

Acoustically-driven fluid interfaces with applications to diagnostic ultrasound bioeffects

by

Brandon Patterson

Dissertation
submitted in partial fulfillment
of the requirements for the degree of
Doctor of Philosophy
Mechanical Engineering
University of Michigan
2017

Doctoral Committee:

Assistant Professor Eric Johnsen, Chair
Professor David R. Dowling
Professor William Schultz
Professor Douglas L. Miller
Professor J. Brian Fowlkes

**Place
Holder**

© Brandon Patterson 2017

All Rights Reserved

TABLE OF CONTENTS

Acknowledgments	i
List of Figures	v
List of Tables	vii
List of Programs	viii
List of Appendices	ix
List of Acronyms and Abbreviations	x
Abstract	xi
Chapter	
I Ultrasound bioeffects	2
1 Introduction	3
1.1 A physical description of sound	3
1.2 Ultrasound in medicine and biological effects	5
1.3 Tissue as a compressible fluid system	6
1.3.1 Dimensional analysis and assumptions for Contrast Enhanced Ultrasound	7
1.3.2 Dimensional analysis and assumptions for acoustically driven alveolus	10
1.3.3 Limitations	12
1.4 Physical mechanisms of ultrasound bioeffects	12
1.4.1 Cavitation of ultrasound contrast agent microbubbles	13
1.4.2 Ultrasound-induced lung hemorrhage	15
1.4.2.1 Driven fluid-fluid interfaces	16
1.5 Thesis overview	18
2 Theoretical microbubble Dynamics at capillary breaching thresholds	19
2.1 abstract	19
2.2 Background & Introduction	20
2.3 Materials and Methods	23
2.3.1 Experimental Setup	23
2.3.2 Bubble Dynamics Model	24
2.4 Results and Discussion	27
2.4.1 Bubble Response	27
2.4.2 Dependence on the Pulse Amplitude	28
2.4.3 Dependence on the Initial (Equilibrium) Bubble Radius	30
2.4.4 Dependence on the Pulse Frequency	32
2.4.5 Dependence on the Tissue Properties	33

2.5	Conclusions	35
3	Dynamics of acoustically-driven gas-liquid interfaces: vorticity as a proposed physical mechanism for ultrasound-induced lung hemorrhage	37
3.1	Abstract	37
3.2	Introduction	38
3.2.1	A review of previous work on diagnostic ultrasound-induced lung hemorrhage	38
3.2.2	A review of previous work on driven fluid-fluid interfaces	41
3.2.3	Explanation and contributions of the present work	44
3.3	Methods	45
3.3.1	Problem set-up	46
3.3.2	Governing equations	47
3.3.3	Numerical methods	50
3.4	Analysis	50
3.4.1	Order of magnitude analysis of vorticity generation mechanisms	51
3.4.2	Comparison of vorticity generation in air and water	54
3.4.3	Considerations of circulation	56
3.5	Preliminary results and discussion	57
3.5.1	Interface response to the $p_a = 10$ MPa trapezoidal wave	58
3.5.1.1	Qualitative behavior of the interface and vorticity	58
3.5.1.2	Dependence on acoustic wave amplitude	59
3.5.1.3	Circulation and vorticity dynamics	60
3.5.1.4	Dependence on the length of the wave	60
3.5.2	Interface response to Diagnostic Ultrasound (DUS) waves	61
3.5.3	Further discussion of the results	62
3.6	Conclusions	63
3.7	Future Work	65
4	Relevance of the vorticity mechanisms to ultrasound	72
4.1	To Do:	72
4.2	Introduction	72
4.2.1	Problem Statement	72
4.2.2	Background	72
4.2.3	Summary	75
4.3	Methods	75
4.3.1	A model of DUS-alveolus interaction	75
4.3.2	Governing Equations	77
4.3.3	Computational implementation	77
4.3.3.0.1	78
4.3.3.0.2	79
4.4	Results and discussion	79
4.4.0.0.3	synopsis of results	79
4.4.1	Qualitative observations of the interface	79
4.4.1.1	Deformation of the interface	79

4.4.1.1.1	Figure with interface snapshots to qualitatively illustrate deformation of interface	79
4.4.1.2	Ultrasound-induced Vorticity generation	79
4.4.1.2.1	Figure with vorticity snapshots to qualitatively illustrate vorticity	79
4.4.2	Ultrasound induced stress and strain at the interface	79
4.4.2.1	Dependence on pulse amplitude, p_a	79
4.4.2.1.1	Viscous shear stresses	80
4.4.2.1.2	Figure with snapshots of viscous stress field and plot of maximum viscous stress vs t	80
4.4.2.1.3	Figure with interface strain (left y-axis) and corresponding elastic stress (right y-axis) vs time for varying p_a	80
4.4.2.2	Dependence on interface perturbation amplitude, a_0	80
4.4.2.2.1	Viscous shear stresses	81
4.4.2.2.2	Figure with snapshots of viscous stress field for $a_0 = 0.03, 0.1, 0.2, 0.3$ and plot of maximum viscous stress vs t for each case	81
4.4.2.2.3	Figure with interface strain (left y-axis) and corresponding elastic stress (right y-axis) vs time for varying a_0	81
4.5	conclusions	81
5	Conclusions	86
II	Underwater Acoustic Uncertainty	87
6	Past work: Efficient estimation of the probability density function of transmission loss in uncertain ocean environments via area statistics	88
6.1	Abstract	88
6.2	Introduction	89
6.3	Methods	92
6.4	Results and comparisons	97
6.5	Conclusions	99
Appendices		101

LIST OF FIGURES

1.1 A schematic illustration of ultrasound induced cavitation and potential bioeffects damage mechanisms (from top to bottom): a). Bubble expansion beyond the radius of a surrounding blood vessel. b.) A cavitation jet away from the wall of a surrounding blood vessel or tissue surface causes the surface to invaginate. c.) A cavitation jet of high speed liquid strikes a vessel or tissue wall. d.) A shock wave created by the bubble collapse encounters nearby tissue.	14
1.2 A schematic of baroclinic torque	17
1.3 A schematic view of the Richtmyer-Meshkov Instability (RMI) instability for a heavy-light interface	18
2.1 Experimental and numerical (filtered) pressure waveforms for the 7.5 MHz pulse at the threshold (Peak negative pressure: 6.0 MPa, 543 ns duration, $MI_{eq} = PRPA/f^{1/2} = 2.2$). Solid: experimental; dashed: numerical.	24
2.2 History of the bubble radius (top) and input-pressure waveform (bottom) for an essentially linear case (frequency: 1.5 MHz; peak negative pressure: 0.35 MPa). No bioeffects are observed here. $R_0 = 1 \mu\text{m}$; solid: $G = 5 \text{ kPa}$; dashed: $G = 100 \text{ kPa}$; dotted: $G = 1 \text{ MPa}$	28
2.3 History of the bubble radius (top) and input-pressure waveform (bottom) for a moderately nonlinear case (frequency: 3.5 MHz; peak negative pressure: 2.4 MPa). Bioeffects are observed here. $R_0 = 1 \mu\text{m}$; solid: $G = 5 \text{ kPa}$; dashed: $G = 100 \text{ kPa}$; dotted: $G = 1 \text{ MPa}$	28
2.4 History of the bubble radius (top) and input-pressure waveform (bottom) for a highly nonlinear case (frequency: 7.5 MHz; peak negative pressure: 6.0 MPa). Bioeffects are observed here. $R_0 = 1 \mu\text{m}$; solid: $G = 5 \text{ kPa}$; dashed: $G = 100 \text{ kPa}$; dotted: $G = 1 \text{ MPa}$	29
2.5 Dependence of the dimensionless maximum bubble radius on the peak negative pressure for $G = 100 \text{ kPa}$. Empty symbols: no bioeffects; filled symbols: bioeffects. Pentagrams: $0.1 \mu\text{m}$; circles: $0.5 \mu\text{m}$; squares: $1 \mu\text{m}$; diamonds: $2 \mu\text{m}$; frequency: 1.5 - 7.5 MHz.	30
2.6 Dependence of the bubble dynamics on the gas contents ($G = 100 \text{ kPa}$). (a) History of the bubble radius for PFP (solid) and air (dashed). $R_0 = 1 \mu\text{m}$; frequency: 3.5 MHz; peak negative pressure: 3.3 MPa. (b) Maximum temperature for PFP (circles) and air (squares). $R_0 = 0.1 - 2 \mu\text{m}$; frequency: 1.5 - 7.5 MHz.	31

2.7	Dependence of the dimensionless maximum bubble radius on the initial bubble size for the amplitude at which bioeffects are first observed, at a given frequency, for $G = 100 \text{ kPa}$. Empty symbols: water; filled symbols: tissue. Circles: 1.50 MHz; squares: 2.25 MHz; diamonds: 3.50 MHz; pentagrams: 5.00 MHz; hexagrams: 7.50 MHz.	32
2.8	Dependence of the bubble dynamics on the frequency for $G = 100 \text{ kPa}$. $R_0 = 0.1 - 2 \mu\text{m}$; empty circles: no bioeffects; squares: bioeffects. (a) Dimensionless maximum bubble radius. (b) Dimensional maximum bubble radius.	33
2.9	Dependence of the maximum bubble radius on frequency and elasticity	34
3.1	A schematic of baroclinic torque	42
3.2	A schematic view of the RMI instability for a heavy-light interface	43
3.3	A schematic view of lung DUS and the model problem	45
3.4	Trapezoidal and DUS pulse waves	47
3.5	The evolution of the acoustically perturbed interface and vorticity field	68
3.6	The interface amplitude and circulation histories for the 10 MPa trapezoidal wave	69
3.7	The interface and circulation dependence on wave amplitude at early time	69
3.8	The interface and circulation dependence on wave amplitude at long time	70
3.9	The individual contributions to circulation generation by physical mechanism	70
3.10	The interface and circulation dependence on wave duration	71
3.11	The interface amplitude and circulation histories for the DUS pulse	71
4.1	(a) and (b) illustrate the physical and model problems we aim to solve.	78
4.2	(??) shows snapshots of the interface at FILL IN $t = 0, \dots$. The interface continues to deform long after the passage of the wave.	80
4.3	Vorticity field at $t = (?)$	81
4.4	(a) and (b) show the shear stress field at $t = (?)$ and the maximum shear stress value within the field as a function of time.	82
4.5	Interface strain and elastic stress field as a function of time	83
4.6	(a) and (b) show the shear stress field at $t = (?)$ and the maximum shear stress value within the field as a function of time.	84
4.7	Interface strain and elastic stress field as a function of time	85
A.1	Center-line pressure at $t=25$. At maximum, 0.1% of the wave is reflected back into the domain.	108
A.2	For cells with non-negligible vorticity, a scatter plot of the mean vorticity in each cell is plotted as a function of volume fraction water (Left).	114

LIST OF TABLES

2.1	Base physical parameters representative of soft tissue used in the present study.	25
3.1	Dimensional properties of air and water used in simulations.	49
3.2	Dimensionless properties of air and water used in simulations.	50

LIST OF PROGRAMS

LIST OF APPENDICES

LIST OF ABBREVIATIONS & ACRONYMS

BAB Blood-air Barrier

CEUS Contrast-Enhanced Ultrasound

DG Discontinuous Galerkin

DUS Diagnostic Ultrasound

HIFU High-Intensity Focused Ultrasound

IC Inertial Cavitation

LH Lung hemorrhage

MI Mechanical Index

PD Pulse Duration

PDF Probability Distribution Function

PRF Pulse Repetition Frequency

PRPA Peak Rarefaction Pressure Amplitude

RMI Richtmyer-Meshkov Instability

STEM Science, Technology, Engineering, and Math

TL Transmission Loss

US Ultrasound

ABSTRACT

Acoustically-driven fluid interfaces with applications to diagnostic ultrasound bioeffects

by

Brandon Patterson

Chair: Eric Johnsen

Numerical simulations are highly useful for approaching a wide range of problems within the field of acoustics. From submarine and whale sounds propagating across vast oceans to ultrasound striking microscopic bubbles in the blood stream behind layers of optically opaque tissue, there are a variety of contemporary acoustic problems with challenges that make them incredibly difficult or infeasible to investigate experimentally. Furthermore, many systems of acoustic interest such as the ocean and human body are immensely complex, rapidly changing, and poorly understood such that at any given time our best knowledge of the system is still fraught with uncertainty. Computation is used to overcome the difficulties of experimentation, explore a range of possibilities in uncertain systems, and to obtain detailed information about physical quantities that are not readily measurable. In this work, we present advancements in two very different areas of acoustics, made possible through the use of computation.

In this work, we investigate two problems related to biological effects of medical Ultrasound (US). The use of US for diagnostic and therapeutic purposes has grown very quickly over the last few decades, as technological advancements have allowed us to use

US for everything from drug delivery and destruction of unwanted tissue to imaging of the internals of the human body. However, certain US procedures have been shown to cause unwanted biological effects that are still poorly understood because they occur on such small length and time scales that they cannot be directly observed as they occur in the body. We develop numerical models to investigate experimentally observed hemorrhage associated with Contrast-Enhanced Ultrasound (CEUS) and Diagnostic Ultrasound (DUS) of the lung. In doing so, we compare calculated cavitation bubble dynamics pertinent to CEUS to previously obtained experimental results to show that accepted thresholds for Inertial Cavitation (IC) are unlikely to be useful for predicting CEUS bio-effects. For the case of DUS of the lung, we propose a new physical damage mechanism based on ultrasonically-induced baroclinic torque at tissue air interfaces within the lungs. We perform analysis and simulations to demonstrate that, given certain simplifying assumptions, predictable deformation of the interface occurs via the proposed mechanism. We conclude that it is a feasible injury mechanism, which will be investigated in detail over the remainder of this thesis.

FINISH ME

Foreword

This dissertation will present work using computation to make advancements in two separate and distinct areas of acoustics: ultrasound bioeffects modeling and acoustic transmission loss uncertainty quantification in uncertain ocean environment. Hence this document is split into two parts along these lines. A summary of relevant background information, work performed, and conclusions in each area will be presented separately.

Part I

Ultrasound bioeffects

CHAPTER 1

Introduction

The purpose of this introduction is to set the stage for the rest of this dissertation and research presented herein and to establish the merit and relevance of the present work. The problems approached here apply to a variety of active areas of study and modern applications within the fields of acoustics and fluids. In the next section, we discuss the application area that is the primary focus and motivation of this work, Diagnostic Ultrasound (DUS) and related biological effects. Accordingly, we describe the driving physical mechanisms of interest to these problems, cavitation and baroclinic vorticity generated by the at accelerated fluid-fluid interfaces. The framework from which we approach these problems, modeling tissue as a compressible fluid system is then discussed. Finally, an overview of the goals and contributions of this thesis are presented.

1.1 A physical description of sound

Sounds are molecular-scale vibrations traveling through a medium. Atoms and molecules perturbed or displaced collide with neighboring atoms and molecules, which collide with their neighbors and so on. In this way, mechanical energy propagates as a wave, away from the initial perturbation location, through any gas, liquid, or solid medium. This is the basic mechanism by which sound moves through all matter whether it be the tissues in human body, the water in the oceans, or the plasma in the stars. Through years of study and experimentation, man has gained a deep understanding for the physical behavior of sound and has learned to harness it as a tool, leading to high-impact advancements throughout Science, Technology, Engineering, and Math (STEM) in

areas ranging from climate change to structural health monitoring and diagnostic and therapeutic medicine. While much of our basic understanding of sound has come from the theoretical study of sound propagating through a constant, infinite, homogeneous medium, there is no such medium in reality, and many of the most interesting physical questions and real world applications of sound are concerned with the scenarios in which sound acts to physically alter the medium through which it is traveling.

The focus of this part of thesis is on problems in which sound travels between multiple media in such a way that the media themselves are physically changed or affected. Typically, when sound traveling in one medium encounters another medium, a portion of the acoustic energy is transmitted through the interface, while the remainder is reflected and scattered back into medium from which the sound originated. In most cases, this results in little change in the media themselves, however, in some instances, acoustic energy can be converted into other forms of energy such kinetic or thermal, resulting in bulk motion or heating of the media respectively. An example of this is a bubble within water or tissue driven by an acoustic wave. As a result of rising and falling acoustic pressure the bubble may oscillate or collapse, changing the temperature or pressure within the bubble and driving the motion of the surrounding medium. Another example is the dissipation of acoustic energy as heat through viscous mechanisms, resulting in a temperature rise in a viscous medium with an acoustic field. The resulting thermal or physical stresses associated with the heating or movement of the media may result in a physical change (eg., phase change) or chemical change (eg., denaturation of proteins in tissue). The ability of acoustic waves to physically alter a media is of particular interest to the field of medical ultrasound, in which it is relevant to both safety concerns in the context of diagnostic sonography and engineering concerns in the context of therapeutic Ultrasound (US).

1.2 Ultrasound in medicine and biological effects

The use of ultrasound in medicine dates back to the 1940s, when Austrian neurologist Dr. Karl Theodore Dussik attempted to use transmission ultrasound to outline the ventricles of the brain (Dussik, 1942; Singh & Goyal, 2007). Since then the abilities and use of US have expanded greatly and the technology has proven to be a powerful tool for noninvasive therapies and safe, real-time diagnostic imaging and its use has become ubiquitous throughout modern medicine.

For context, I will explain the basic physical processes that occur during US procedures. In practice, high-frequency, typically MHz range, acoustic waves and pulses are created at the surface of the body using a piezoelectric US transducer. These vibrations, or acoustic waves, propagate via an impedance matching, acoustic coupling medium from the transducer into the tissue. Once in the tissue, a portion sound scatters at material interfaces within the body, where acoustic impedance changes, or more simply, some of the sound echoes whenever it moves from one tissue to another, or encounters a cavity in the body. This scattering of sound is the basic physical principle that makes the use of ultrasound for diagnostic imaging possible. In DUS, scattered echoes are picked up by a receiver, recorded, and processed. The strength and timing of these echoes are used to generate a real-time image of the scattering surface. This passage of acoustic waves through tissue does not typically directly alter or affect the tissues structures or processes and the use of ultrasound for imaging is typically considered safe and noninvasive. Despite this, this process is not entirely passive. When energy from ultrasound is converted to kinetic or thermal energy, within tissue, it can physically alter or damage that tissue through a variety of mechanisms. These effects to the body are referred to as US bioeffects. In therapeutic applications, US is used to intentionally cause desirable bioeffects that are beneficial to the patient. In the case of diagnostic ultrasound, bioeffects are generally undesirable side effects that are avoided if possible. Ultrasound bioeffects have motivated extensive research for use in the development of effective guidelines and regulations for the development and use of safe US technologies and procedures.

A large portion of past research into ultrasound bioeffects has focused on determining what

types of US bioeffects exist, under what circumstances do they occur. This work has shown that bioeffects may take on a variety of different forms, commonly hemorrhage or cell death. In gaseous tissues such the lung and intestines, ultrasonically induced hemorrhage has been observed. LEHMANN & HERRICK (1953) and Miller & Thomas (1994) observed abdominal peritoneal hemorrhage as a result of unfocused ultrasound in mice. And Child *et al.* (1990) found hemorrhage in mouse lungs after the animal was exposed to lithotripter pulses. Numerous other studies have been performed on the topic of US-induced lung hemorrhage and a much deeper review can be found in chapters 3 and 4. Pulsed ultrasound of the heart has been shown to be capable of inducing cardiac contractions in frogs and mice (Dalecki *et al.*, 1993; MacRobbie *et al.*, 1997). Cell death has been observed in liver, kidney, and heart as a result of Contrast-Enhanced Ultrasound (CEUS), which uses injections of contrast microbubbles as additional scattering surfaces Skyba *et al.* (1998); Miller *et al.* (2008a). In this thesis I will use computational models to investigate bioeffects resulting from CEUS and DUS-induced lung hemorrhage.

1.3 Tissue as a compressible fluid system

To investigate CEUS and DUS-induced lung hemorrhage, throughout this dissertation I will be modeling the relevant physical problems of ultrasound in human tissue as compressible, multiphase fluid systems. In this section I will attempt justify this general approach and explain some of the applicable assumptions and implications.

The underlying governing equations upon which each of our models are based are the general conservation equations for mass, momentum, and energy for a fluid,

$$\frac{\partial \rho}{\partial t} + \nabla \cdot (\rho \mathbf{u}) = 0, \quad (1.1a)$$

$$\rho \frac{D \mathbf{u}}{Dt} = \nabla \cdot \boldsymbol{\tau} + \mathbf{g}, \quad (1.1b)$$

$$\frac{\partial E}{\partial t} + \nabla \cdot (E \mathbf{u}) = \rho (\mathbf{g} \cdot \mathbf{u}) + \nabla \cdot (\boldsymbol{\tau} \mathbf{u}) + \nabla \cdot \mathbf{q}, \quad (1.1c)$$

where ρ is density, \mathbf{u} is the flow velocity vector, t is time, $\boldsymbol{\tau}$ is the stress tensor, which is a second order tensor. \mathbf{g} is the body force vector, $E = \rho (e + \frac{1}{2} [\mathbf{u} \cdot \mathbf{u}])$ is the total energy defined as the sum of the kinetic energy per unit mass $\frac{1}{2} (\mathbf{u} \cdot \mathbf{u})$ and the internal energy per unit mass e , and lastly \mathbf{q} is the heat flux vector. To model ultrasound-tissue interactions, the general conservation equations (1.1) are simplified and manipulated based on the physics appropriate to the specific problem at hand. The closure of these equations is also treated differently depending on the particular problem and model. Details on the appropriate equations of state used to relate pressure and energy, constitutive equations used to relate stress and strain, and boundary conditions are described in greater detail in sections 2.3.2 and 3.3.2.

To consider what physical effects are at play during diagnostic ultrasound, both contrast-enhanced and of the lung, I consider the basic physical scenario of each of these problems. That is an acoustic wave travels through a multiphase medium consisting of soft tissue and gas. Soft tissues are viscoelastic materials, i.e., they exhibiting solid and fluid like behaviors, i.e, viscous and elastic effects may be simultaneously at play. These tissues include blood as well as lung, liver, and kidney tissue, which are relevant to the motivations of this thesis. The multiphase component of these problems suggests that gas-liquid/gas-viscoelastic interface phenomena such as surface tension may also be of some relevance. As fluid motion is expected, inertial effects will likely be of importance. Additionally, as ultrasonic heating is a known source of biological effects, I consider this possibility as well. And for completeness, since the vast majority of ultrasound procedures do not occur on the International Space Station, I consider the effects of gravity too. In the following two sessions, I introduce dimensional analysis to assess the relative importance of each of these physical phenomena for the problems we approach in this part of the thesis.

1.3.1 Dimensional analysis and assumptions for Contrast Enhanced Ultrasound

CEUS-related bioeffects are generally attributed to a process called Inertial Cavitation (IC) in which a bubble or void within a fluid collapses rapidly. This can result in high temperatures,

pressures, stresses, strains, and strain rates within the surrounding fluid. More details about this process and its relationship to US bioeffects will be provided in Section 1.4.1. In this work, I consider the problem of a single US pulse impinging upon a contrast agent microbubble, initially at rest within a viscoelastic soft tissue. For the sake of justification I consider a typical case here. In Chapter 2 a more in-depth analysis, specific to the work presented, is performed. Consider an ultrasound pulses of clinically relevant frequency $f = 3$ MHz and Peak Rarefaction Pressure Amplitude (PRPA)= $p_a = 1$ MPa. The soft tissue is treated as a Voigt type viscoelastic material as in (Yang & Church, 2005) and has a nominal density of $\rho = 1000$ kg/m³, an elastic modulus ranging from $G = 10$ kPa to 1 MPa, and a viscosity of $\mu = 0.015$ Pa s. Surface tension will be based on water such that $S = 0.056$ N/m. Consider a characteristic velocity of $u = \sqrt{p_a/\rho} = 31.6$ m/s. Note that the physical properties of soft tissue vary widely and are poorly characterized, particularly at the strain rates associated with cavitation. As a characteristic length scale, I use a typical bubble size such that equilibrium radius is $R_0 = 1\mu\text{m}$.

Based on this setup I perform dimensional analysis to assess the relative importance of each of the potentially relevant physical mechanisms to the problem of acoustically-driven cavitation in soft tissue:

Viscosity: To access the relevance of viscosity I consider a Reynolds Number, which is defined as $Re = \rho u R_0 / \mu = 2.1$ and is a measure ratio of inertial to viscous forces in a flow. A Reynolds number of order unity, suggests that viscous effects are non-negligible relative to inertia and cannot be neglected.

Heat transfer and thermal effects: In consideration of the role of heat transfer, I calculate a characteristic time scale for heat transfer $t_{thermal} = R_0^2 / \alpha$, where α is the thermal diffusivity, which is $\alpha = 0.143 \times 10^{-6}$ m²/s in water such that $t_{thermal} = 7\mu\text{s}$. This is compared to the approximate timescale for a spherical vapor bubble to collapse to its minimum radius, neglecting surface tension, which is approximately $t_{collapse} = 0.915 \sqrt{\rho R_0^2 / p_a} = 29$ ns (Brennen, 2003). Note that the

form of the equation presented here is for the case where the vapor pressure in the bubble p_v is much smaller than the driving pressure p_a , which is true for ultrasonically driven cavitation. Here, $t_{collapse} \ll t_{thermal}$, suggesting that minimal heat transfer will occur during the collapse. This is perhaps unsurprising, as heat transfer is generally regarded as a much slower process than IC. In any case, heat transfer into and out of the bubble will be neglected in relevant analysis.

Surface Tension: The Weber number is defined as $We = \rho u^2 R_0 / S = 17.9$ and represents the ratio of surface tension to inertial forces in the flow. The calculated We suggests that surface tension at the bubble wall is not negligibly small when the bubble is at its equilibrium radius. Additionally, I note that the effects of surface tension may have an even greater effect during collapse when the bubble radius may decrease by an order of magnitude or more. Hence surface tension cannot be neglected.

Elasticity: The Cauchy number is defined as $Ca = \rho u^2 / G = 1 - 100$. Based on this the effects of elasticity are not expected to be particularly important to the bubble dynamics for the tissues of kPa order elasticity, though this is expected to change for stiffer tissues. Accordingly, elasticity will be included in the cavitation bubble model.

Gravity: The Froude number is defined as $Fr = u / \sqrt{gR_0} = 10^4$ and is a measure of the ratio of inertial to gravitational forces, or more generally, any applicable body forces. The calculated Froude number suggests that gravitational and buoyancy effects are minimal relative to inertia and will be neglected for the sake of this analysis. This is of particular importance because it allows us to consider the case of a radially symmetric collapse, which greatly simplifies the problem.

In summary, based on the dimensional analysis performed, I will consider axially symmetric bubble dynamics in a Voigt-Viscoelastic medium with surface tension. The effects of gravity and heat transfer will be neglected.

1.3.2 Dimensional analysis and assumptions for acoustically driven alveolus

The work presented here is specifically interested in the problem of an ultrasound pulse impinging upon an alveolus within an adult human lung. To access the relevant physical mechanisms here in order to layout the logic for my assumptions and approach, I present a general case relevant to the motivating problem of lung ultrasound. A more comprehensive justification and analysis, specific to the work presented can be found in chapters 3 and 4. Consider an ultrasound pulse with central frequency $f = 3\text{MHz}$, and amplitude $p_a = 1 \text{ MPa}$, which is in the expected range based on past research (Miller *et al.*, 2015). I will use the mean diameter of a typical adult human alveolus as a characteristic length scale length scale $\ell_A = 200\mu\text{m}$ (Ochs *et al.*, 2004). The alveolus is treated as being filled with air such that the sound speed is $c_A = 343 \text{ m/s}$, the density is $\rho_A = 1.2 \text{ kg/m}^3$, the kinematic viscosity is $\nu_A = 16.6\mu \text{ m}^2/\text{s}$, and no elasticity is present in the alveolar interior. The surrounding soft-tissue is treated as water-like, but with elasticity such that the sound speed is $c_T = 1500 \text{ m/s}$, the density is $\rho_T = 1.2$, the viscosity is $\nu_T = 0.7\mu\text{m}^2/\text{s}$ and the elastic modulus is $G = 5 \text{ kPa}$ (Cavalcante, 2005). I use a characteristic velocity $u_a = \sqrt{p_a\rho}$. Based on the physical problem described here I use dimensional analysis to access the relative importance of potentially relevant physical mechanisms:

Viscosity: In consideration of effects of viscosity of the dynamics of the system during the ultrasonic interface, I calculate a viscous length scale on either side of the interface such that $\sigma_{vA} = \sqrt{\nu_A/2\pi f} = 0.94\mu\text{m}$ and $\sigma_{vT} = \sqrt{\nu_T/2\pi f} = 0.19\mu\text{m}$. On either side of the interface $\sigma_v \ll \ell$ such that the viscous layer is small compared to the flow geometry during the ultrasonic interactions. In recognition that the viscous layer may grow in time, after the passage of the acoustic wave, according to $\sigma_v(t) \sim \sqrt{\nu t}$ we calculate that for a 1 kHz Pulse Repetition Frequency (PRF), the viscous layer may grow to $\mathcal{O}(\ell)$ in the alveolar airspace and $\mathcal{O}(0.1\ell)$ in the surrounding tissue. Hence viscosity can be neglected for sufficiently early times, and I will do so in the model for simplicity. I will not consider times later than $\approx 300\mu\text{s}$ to maintain reasonable accuracy of

our inviscid assumption. The applicability of assumption in practical lung ultrasound is aided by the fact that even higher frequencies are sometimes used in clinical application Lichtenstein (2009).

Heat transfer and thermal effects; I use similar arguments to those used for viscous effects in consideration of thermal effects. The thermal length scale is defined as $\sigma_\kappa = \sqrt{\kappa/\pi f \rho C_p}$, where the C_p is the specific heat and κ is the thermal conductivity. In air $C_{pA} = 1005 \text{ J/Kg K}$ and $\kappa_A = 0.027 \text{ W/m K}$ and in Water $C_{pT} = 1005 \text{ J/Kg K}$ and $\kappa_T = 0.49 \text{ W/m K}$. Hence $\sigma_{\kappa A} = 0.3\mu\text{m}$ and $\sigma_{\kappa T} = 1.5\mu\text{m}$. On either side of the interface, $\sigma_\kappa \ll \ell$ such that the thermal boundary layer is small relative to the characteristic length of the flow. Hence I will neglect heat transfer in my approach to this problem moving forward.

Surface Tension: The role of surface tension in the alveoli is critical to healthy respiratory function. Alveoli secrete pulmonary surfactant, which lowers the surface tension at the alveolar surface, helping prevent airway collapse and easing the re-inflation of alveoli during breathing. As a result of this surfactant, alveolar surface tension is far below that of water and has been reported as $S_A = 9 \text{ mN/m}$ (Schürch *et al.*, 1976). Hence I define an acoustic Weber number as $We = p_a \ell / S_A = 22222$. This suggests that forces due to surface tension are small relative to the acoustic pressure at the interface. Based on this, I will neglect surface tension in my analysis as well.

Elasticity: To assess the expected impact of elasticity on the system I define an acoustic Cauchy number $Ca = \rho_T u_a^2 / G$ which becomes the ratio of the acoustic pressure to the elasticity $p_a / G = 200$. This suggests that the effects of elastic effects will be dominated by the acoustic pressure during the wave-interface interaction within the tissue. Within the alveolar air space, there is no elasticity and the Cauchy number is infinite. Based on this, I will neglect elasticity in my model.

Gravity: The importance of gravity is assessed based on a Froude number calculation $Fr =$

$u_a/\sqrt{g\ell} = \sqrt{p_a/\rho g\ell} = 714$. This suggests that gravitational forces are small relative to inertia, and will be neglected. Another reasonable justification for neglecting gravity is that the orientation of the model problem in space is arbitrary and as a 2D model I treat the flow as existing in a plane that is orthogonal to gravitational forces and thus not unaffected by gravity.

1.3.3 Limitations

Before proceeding I would like to acknowledge that the simplifications and assumptions made in the previous sections, while justified in the specified regimes, do deviate from the true physical systems. The purpose of these simplifications is to make the relevant problems tractable with the available resources (computational, intellectual, financial, temporal, etc...). There are many limitations to described model systems that result in aspects of the true physics that are not captured. In both CEUS and in ultrasound-alveoli interactions, the presented dimensional analysis is based on tissue properties such as viscosity and elasticity and behavior that are poorly characterized in both nature and quantity. Additionally the analysis performed here is for reference cases within the relevant range, and certain dependencies, such as the frequency dependence of sound speed in bulk lung tissue, are not capture here. Additionally, actual tissues are highly heterogeneous and may be characterized by a wide range of physical length scales. Despite these limitations, the purpose of this work is to gain insight into the approximate physics applicable to these problems, which hopefully this approach achieves.

1.4 Physical mechanisms of ultrasound bioeffects

Depending on the type of physical damage mechanism responsible, these bioeffects are classified into two groups, thermal and non-thermal. The first group, thermal bioeffects are characterized by deposition of acoustic energy into tissue as heat and are often a result of therapeutic, rather than diagnostic, ultrasound. This heating can lead to a variety of deleterious effects including the release of highly reactive free radicals and protein denaturation at the molecular level and protein

denaturation and death at the cellular level, ultimately causing tissue damage or death. As an example, one class of therapeutic US, known as High-Intensity Focused Ultrasound (HIFU) uses strong, concentrated acoustic fields, to intentionally convert acoustic energy to heat through viscous dissipation. This is used to raise the temperature of unwanted tissues such as fat or cancer to destroy it. Little else will be said about thermal bioeffects, as the bioeffects problems of interest to this work fall into the non-thermal category. The bulk of known non-thermal bioeffects are attributed to acoustically-induced cavitation. For certain bioeffects, such as DUS-induced lung hemorrhage, the physical mechanisms is largely unknown.

The bioeffects that are of motivation and interest to this thesis are those that can result from DUS. While the occurrence of ultrasound bioeffects is intentional and desirable in Therapeutic US, this is typically not the case for when US is used for diagnostic imaging. DUS bioeffects tend to be a result of mechanical processes and typically take the form of unintended tissue damage or cell death. In the remainder of this section I will introduce the bioeffects and mechanisms relevant to this thesis.

1.4.1 Cavitation of ultrasound contrast agent microbubbles

Acoustic cavitation is the phenomenon by which gas nano and microbubbles, called cavitation nuclei, are cyclically grown by low pressures within the US field and then collapsed high pressures within the field. When the bubble dynamics during collapse are dominated by the inertia of the surrounding fluid, it is called IC. IC is typically violent and results in the bubble collapsing to a fraction of its original size. There are several possible damage mechanisms associated with IC that may be responsible for observed US bioeffects. Upon collapse, the pressure and temperature within the bubbles spike, often reaching billions of pascals and thousands of Kelvin respectively. Due to the pressure difference between the vapor/gas mixture within the bubble at collapse and the surrounding media, the collapsed bubble can emit a powerful shock wave which can be damaging to the bubbles surroundings. When cavitation is triggered near a rigid surface, the bubble can collapse in a radially asymmetric fashion causing a high speed “re-entrant” jet of liquid to impinge

upon the surface, effectively striking the surface with a liquid hammer. If cavitation occurs at an appropriate distance from a non-rigid surface, such as soft tissue boundaries and blood vessel walls, the jet can impinge away from the surface, potentially invaginating the surface (Brujan, 2011).

While IC does not typically occur during non-contrast DUS, it is of possible concern during CEUS, which uses contrast-agent microbubbles injected into patients bloodstream to act as additional scattering surfaces. This allows for high contrast imaging and can be used to ultrasonically image blood flow, which is useful for diagnosing heart valve problems, liver lesions, and more (Claudon *et al.*, 2013; Rognin *et al.*, 2008). However, the use of contrast agent microbubbles can also have potential deleterious side effects. These microbubbles can act as cavitation nuclei and the resulting cavitation has been associated with a variety of different forms of cellular death and damage.

The precise ultrasonic thresholds for which cavitation and bioeffects occur have not been clearly described. Furthermore, the exact physical mechanisms through which cavitation causes bioeffects are also not clearly understood (Barnett *et al.*, 1994). Figure 1.1 schematically illustrates potential ultrasound-induced cavitation damage mechanisms. This thesis presents past work investigating the relationships between ultrasound and tissue parameters and cavitation bubble dynamics in clinically relevant regimes. In Chapter 2 we simulate ultrasonically induced cavitation of contrast agent microbubbles in soft tissue (Patterson *et al.*, 2012a) (See Chapter 2). I simulate experimentally measured US waves obtained by Miller *et al.* (2008b) perturbing microbubbles in a Voigt viscoelastic soft tissue (Yang & Church, 2005). The calculated cavitation dynamics and theoretical inertial cavitation thresholds (Flynn, 1982; Apfel, 1982) are compared with bioeffects thresholds associated with each US pulse, as defined by the observation of kidney hemorrhage in rats after exposure to CEUS by Miller *et al.* (2008b). While the results were generally dependent on US, gas, and tissue properties, it was found that the inertial cavitation thresholds were lower than observed bioeffects thresholds.

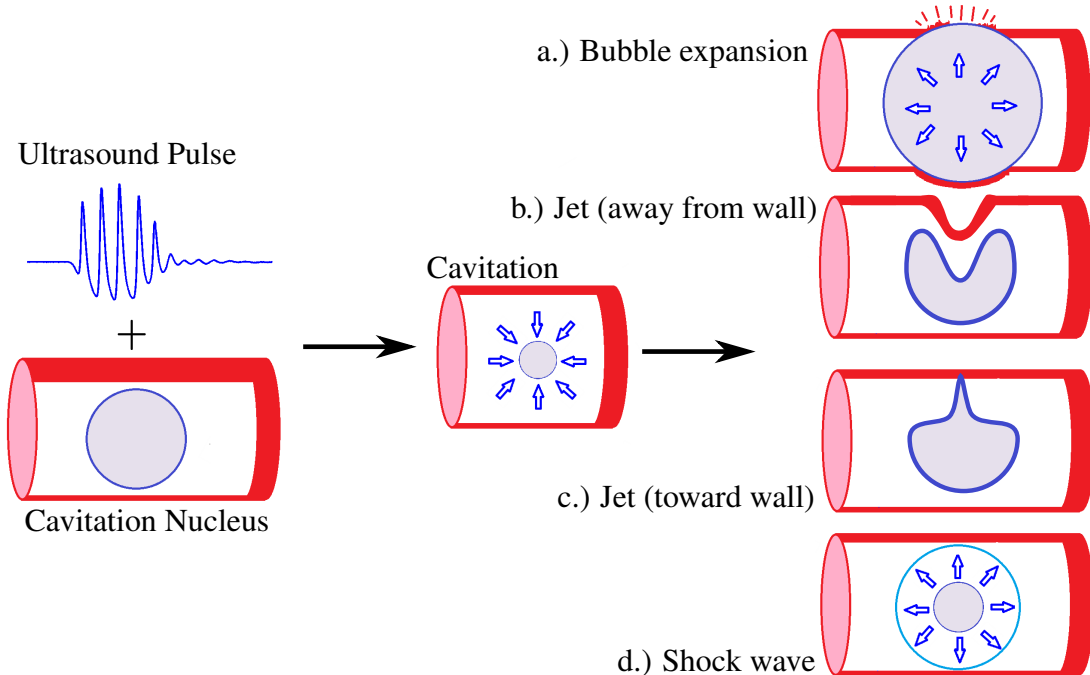


Figure 1.1: A schematic illustration of ultrasound induced cavitation and potential bioeffects damage mechanisms (from top to bottom): a). Bubble expansion beyond the radius of a surrounding blood vessel. b.) A cavitation jet away from the wall of a surrounding blood vessel or tissue surface causes the surface to invaginate. c.) A cavitation jet of high speed liquid strikes a vessel or tissue wall. d.) A shock wave created by the bubble collapse encounters nearby tissue.

1.4.2 Ultrasound-induced lung hemorrhage

The second US bioeffects topic of interest to this thesis is DUS-induced Lung hemorrhage (LH). This phenomenon was first discovered in mice in the over twenty years ago [Child et al. \(1990\)](#) and has since been shown to occur in a variety of other mammals including rats, pigs, rabbits, and monkeys [O'Brien & Zachary \(1997\)](#); [Miller \(2012\)](#); [Tarantal & Canfield \(1994\)](#). Research into this phenomena has been in three main areas: (1) Determining the physical mechanism of the hemorrhage; (2) Understanding how the occurrence and severity of the hemorrhage on the ultrasonic properties (frequency, amplitude, waveform, etc...); and (3) Understanding how the occurrence and severity of the hemorrhage on the characteristics of ultrasound subject (species, age, anesthesia, etc...). The work in this thesis pertains mostly to the first of these three areas.

Despite extensive previous research into DUS-induced LH, the underlying physical mechanisms are still not well understood. Furthermore, past work has shown that common US bioeffects mechanisms do not explain this phenomena. Research has shown that thermal damage mechanisms are unlikely as DUS-induced lung lesions do not appear similar to those induced by heat ([Zachary et al., 2006](#)). Furthermore, cavitation mechanisms do not appear to be responsible, as the severity of DUS-induced LH in mice increased under raised hydrostatic pressure ([O'Brien et al., 2000](#)) and was unaffected by the introduction of US contrast agents into subjects. Both of these results are inconsistent with what is expected of IC-induced bioeffects. More recent work by [Miller \(2016\)](#) investigating Acoustical Radiation Surface Pressure as a potential damage mechanism found that the pressures expected in pulsed ultrasound were likely too low to cause the observed hemorrhage. [Simon et al. \(2012\)](#) Found that atomization and fountaining occurred at tissue-air interfaces subjected to HIFU and suggested that this could potentially happen at diagnostic levels as well. Similarly, works by [Tjan & Phillips \(2007, 2008\)](#) model the evolution of an inviscid, free surface subjected to a Gaussian velocity potential and find that this can lead to the ejection of liquid droplets. They go on to say that DUS of the lung may similarly lead to the ejected of droplets capable of puncturing the air-filled sacs within the lung. The problem of US-lung interaction is the central motivation of

chapters 3 and 4. As such, a far more in-depth literature review will be provided in these chapters

1.4.2.1 Driven fluid-fluid interfaces

The physical problem underlying interactions between ultrasound waves and the various tissue and fluid layers of the body is that of a mechanical wave traveling in one fluid encountering a second fluid of differing physical properties. As was previously explained, this can result in acoustic energy being converted into motion or other effects. In the case of the bubble, the relevant manifestation of this was cavitation. Another manifestation of this is the growth of perturbations at fluid-fluid interfaces as a result of non-uniform velocity gradients that occur at the driven interface. Another way of think of this is in terms of baroclinic vorticity, or localized fluid rotation, generated by the misalignment of interface density gradients and mechanical wave pressure gradients. In this dissertation I will later propose this baroclinic vorticity effect as a potential mechanism for ultrasound induced alveolar hemorrhage. In the remaining portion of section I discuss in greater detail the underlying physics at play here and some of the past work that has been done to understand it.

Previously, there has been extensive research into the fundamental physics describing interactions between mechanical waves, acceleration, and fluid-fluid interfaces. Much of this research is motivated by applications in fusion energy and astrophysics and accordingly has sought to investigate regimes outside of those of acoustic interests. Taylor (1950) predicted that for an interface between two fluids of different density, if the fluid was accelerated normal to the interface in the heavy-to-light direction, perturbations at the interface would grow. That is to say that a “bubble” of light fluid penetrates the heavy fluid, and a “spike” of heavy fluid penetrates the light fluid. This is known as the **RTI!** (**RTI!**). A similar topic of past study is the Richtmyer-Meshkov Instability (RMI), which occurs when a perturbed fluid-fluid interface is instantaneously accelerated by a shock, causing the interface perturbation to grow (Brouillette, 2002; Drake, 2006). This growth is driven by a sheet of baroclinic vorticity deposited along the interface as a result of misalignment between the pressure gradient across the shock and the density gradient across the perturbed interface. This physical mechanism by which these misaligned gradients create a torque on fluid

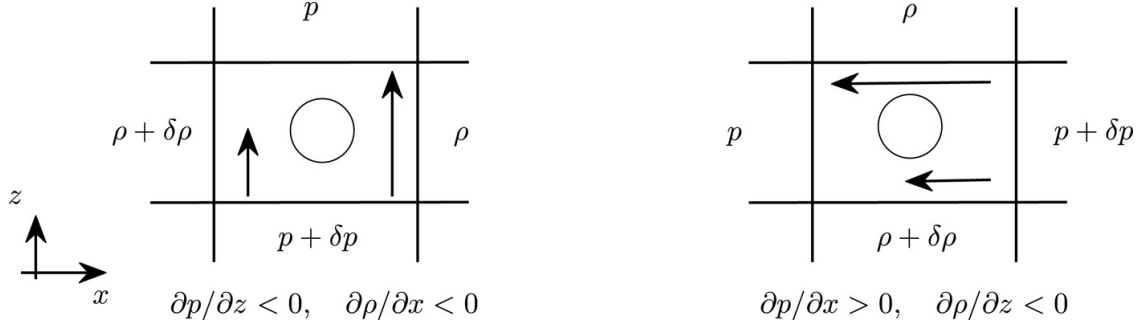


Figure 1.2: From [Heifetz & Mak \(2015\)](#). A hydrostatic force balance upon a particle subject to perpendicular pressure and density gradients illustrates baroclinic torque on a fluid particle.

particles and generate vorticity can be thought of in terms of a hydrostatic balance upon a particle. Pressure gradients result in acceleration of the flow that is inversely proportional to density. When these two gradients are misaligned, the result is a shearing effect on the fluid and vorticity is generated ([Heifetz & Mak, 2015](#)). A graphical explanations of baroclinic vorticity generation is shown in Figure ???. 3.1 from [Heifetz & Mak \(2015\)](#). Analytically, baroclinic vorticity generation can be shown by taking the curl of the conservation of momentum equation for a compressible fluid. It is worth noting that it is a nonlinear effect and cannot be explained by traditional linear acoustics.

The physics of the RMI are fairly well understood. For the classical RMI setup a planar shock impinges normally upon the peaks and troughs of a sinusoidal interface. The interface is accelerated non-uniformly counter-rotating vorticities are generated across the interface. This drives peaks and troughs of the interface to accelerate in the opposite direction. Much like in the case of the **RTI!** instability, this too results in light fluid penetrating the heavy fluid and vice versa. For the case of a wave moving from a light fluid into a heavy one, the peaks and troughs of the interface accelerate away from one another, growing the interface perturbation perturbation. For the case of a wave moving from a heavy fluid to a lighter fluid, the peaks and troughs interface initially accelerate toward one another. They then pass each, inverting the phase of the interface perturbation, and continue moving in opposite directions, growing the perturbation amplitude. This process is illustrated in Figure 3.2, which has been adapted from [Brouillette \(2002\)](#).

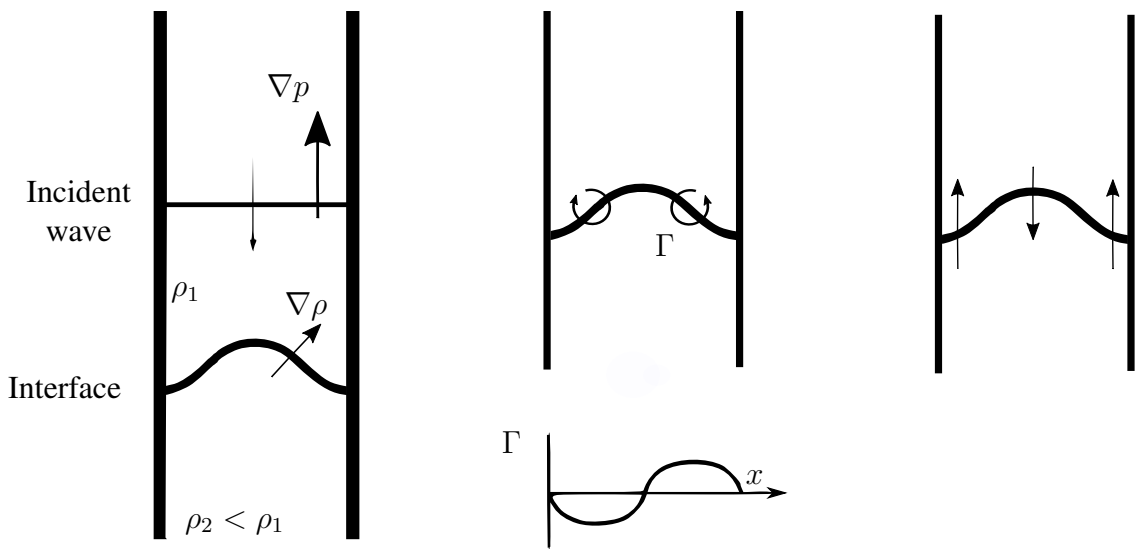


Figure 1.3: Adapted from [Brouillette \(2002\)](#). The RMI for a heavy-light interface is illustrated. The initial condition (left), circulation post wave-interface interaction (center), and perturbation growth (right) are shown.

1.5 Thesis overview

CHAPTER 2

Theoretical microbubble Dynamics at capillary breaching thresholds

In this chapter we present work in which experimentally-measured US pulses are used to simulate US contrast agent microbubble dynamics. The pulses were previously used in experiments to determine capillary breaching thresholds in rat kidneys (Miller *et al.*, 2008b). We compare the calculated bubble dynamics to the experimentally-determined bioeffects thresholds to investigate the use of theoretical IC thresholds as a predictor for bioeffects. This work was published in the Journal of the Acoustical Society of America (Patterson *et al.*, 2012a,b).

2.1 abstract

In order to predict bioeffects in contrast-enhanced diagnostic and therapeutic ultrasound procedures, the dynamics of cavitation microbubbles in viscoelastic media must be determined. For this theoretical study, measured 1.5-7.5 MHz pulse pressure waveforms, which were used in experimental determinations of capillary breaching thresholds for contrast-enhanced diagnostic ultrasound in rat kidney, were used to calculate cavitation nucleated from contrast agent microbubbles. A numerical model for cavitation in tissue was developed based on the Keller-Miksis equation (a compressible extension of the Rayleigh-Plesset equation for spherical bubble dynamics), with a Kelvin-Voigt constitutive relation. From this model, the bubble dynamics corresponding to the experimentally obtained capillary breaching thresholds were determined. Values of the maximum ra-

dius and temperature corresponding to previously determined bioeffect thresholds were computed for a range of ultrasound pulses and bubble sizes for comparison to inertial cavitation threshold criteria. The results were dependent on frequency, the gas contents, and the tissue elastic properties. The bioeffects thresholds were above previously determined inertial cavitation thresholds, even for the tissue models, suggesting the possibility of a more complex dosimetry for capillary injury in tissue.

2.2 Background & Introduction

Cavitation-bubble collapse has been a topic of interest in physical acoustics for nearly a century and has been the object of many experimental and theoretical studies, which have outlined the complexity of the phenomenon (Leighton, 1997). This field made a landmark contribution to non-ionizing radiation biology in medicine in the 1980s when the possibility of inertial cavitation, with potential induction of bioeffects, from diagnostic ultrasound pulses was predicted theoretically (Flynn, 1982; Apfel, 1982). This possibility was included in considerations for the regulation of the ultrasound output of diagnostic machines. Apfel & Holland (1991) performed detailed calculations of the response of different nuclei sizes in the form of free air microbubbles and found that the optimum size decreased with increasing frequency, f . In addition, the rarefactional pressure amplitude threshold, p , for inertial cavitation was determined for the optimum nuclei, using the criterion of a $>5,000$ K gas temperature at collapse. For nuclei in blood, the ratio of $p^{1.67}/f$ was found to have a constant value of 0.13 at the threshold, using units of MPa and MHz. This finding was used to create a Mechanical Index (MI) for regulatory purposes and for display on the screens of diagnostic ultrasound machines. The MI was set equal to the peak rarefactional pressure amplitude (PRPA) adjusted for attenuation, and divided by the square root of frequency. The regulatory guideline limit for diagnostic ultrasound was considered according to the Medical Device Amendment Act of 1976 and the maximum value existing at that time. This guideline limit was eventually set from measurements on a single diagnostic ultrasound probe to be 1.9 (Nyborg,

2001). It is noteworthy that the critical value corresponding to the Apfel & Holland (1991) result would be $p/f^{0.6} = 0.29$, which is much less than the MI limit. This discrepancy does not appear to be of concern for normal diagnostic ultrasound from both experimental (Carstensen *et al.*, 2000) and theoretical (Church, 2002) considerations.

To improve diagnostic information in ultrasound examinations, ultrasound contrast agents (UCAs) were invented. The contrast agents consist of a suspension of stabilized gas-filled microbubbles, which provide strong echoes from blood and improve contrast in sonography (Averkiou *et al.*, 2003; Raisinghani *et al.*, 2004). Soon after contrast-enhanced diagnostic ultrasound was developed, microscale bioeffects were reported (?). The typical bioeffect seen in mesentery, muscle, heart, and kidney was capillary rupture, which appeared to be caused by cavitation nucleation in blood from the circulating contrast microbubbles. Recently, hemorrhage of glomerular capillaries was studied in rat kidney to determine PRPA thresholds and the frequency dependence of the thresholds (Miller *et al.*, 2008b). Presumably, the thresholds correspond to the action of the optimum cavitation nuclei, and this approach therefore provides a means to directly compare cavitation theory with the bioeffects experiments. Over the 1.5-7.5 MHz frequency range tested, the thresholds were proportional to the frequency, such that p/f was approximately constant at 0.49 MPa/MHz for actual diagnostic ultrasound and 0.62 MPa/MHz for diagnostic ultrasound simulated by a laboratory pulsed-ultrasound system. These thresholds fell below the MI=1.9 level, especially for the lower frequencies, but above the inertial cavitation thresholds of Apfel & Holland (1991), and the frequency dependence was different. Evidently, the bioeffects thresholds depend on cavitation dynamics not specifically tied to the inertial cavitation threshold of free air bubbles in blood determined by Apfel & Holland (1991). The fundamental reason for these results remains uncertain, which revives the non-ionizing radiation biology problem of ultrasonic cavitation in medical ultrasound.

The theoretical model of Apfel & Holland (1991) applies to air microbubbles in a Newtonian liquid. However, contrast agents in the blood stream do not necessarily exhibit such properties. It is well-known that human tissue behaves in a viscoelastic fashion (Frizzell, 1976; Madsen *et al.*,

1983). The bubble dynamics greatly depend on not only the viscoelastic properties (Allen & Roy, 2000b; Yang & Church, 2005) for a given model, but also on the type of model (Johnsen & Hua, 2012) and on nonlinearity (Allen & Roy, 2000a). Furthermore, the gas contained in contrast agents is not air; for example, perfluoropropane (PFP, C₃F₈) in Definity (Perflutren Lipid Microsphere, Lantheus Medical Imaging, N Billerica MA), which may affect the collapse temperature. The stabilizing skin or shell may not be an important factor for the capillary rupture bioeffect, because the nucleation process appears to liberate a free gas microbubble. The thresholds for this cavitation bioeffect are above the destabilization threshold of the optimal microbubbles, which therefore may be modeled as free microbubbles (Sboros *et al.*, 2002; Marmottant *et al.*, 2005). Basically, at low PRPAs the stabilization is lost, which releases a free microbubble, thus nucleating cavitation, followed by dissolution at the conclusion of the pulse (Porter *et al.*, 2006). In the case of diagnostic ultrasound, the microbubble is subjected to a series of pulses that start low, build to a peak and finally decline. Thus, when the peak pulse arrives to cause the injury, the microbubbles likely are already destabilized.

The detailed mechanism by which cavitation causes bioeffects is unknown, although several have been proposed, such as shock emission upon collapse, growth beyond a given size, high temperatures generating free radicals, re-entrant jets in non-spherical collapse (Zeqiri, 2003). In order for such phenomena to occur, it is expected that inertial cavitation occurs. From this observation, prior studies have used the threshold for inertial cavitation as a surrogate for bioeffects (Yang & Church, 2005). This inertial cavitation threshold was developed theoretically for bubble dynamics in water (Flynn, 1975). In this work, we show that the bioeffects threshold is different from previously developed inertial cavitation thresholds. The difference between the inertial cavitation threshold calculated for air microbubbles in blood and the capillary rupture thresholds is likely due to an incomplete model. That is, the homogenous model results may correlate better with the bioeffects results if tissue elasticity, gas contents, pulse parameters, and possibly other factors are considered.

In the current work, a different approach combining experiments and numerical modeling to

studying bioeffects is followed. *In vivo* experiments were performed to determine the pulse amplitude and frequency under which bioeffects occur (Miller *et al.*, 2008b). Given these experimental pulses, bubble dynamics are modeled numerically over the entire waveform duration, which is not taken into account by Apfel & Holland (1991), to determine how the bubble response correlates with the observation of bioeffects. A detailed description of the methodology is presented. The experimental setup and numerical model are first discussed in §2.3. The results from the combined experimental and numerical procedure are presented in §2.4. The ability of established inertial cavitation thresholds, and general cavitation parameters, to predict bioeffects is discussed. The article ends with a summary of the results and considerations for future work on this topic.

2.3 Materials and Methods

2.3.1 Experimental Setup

In the previous study of glomerular capillary hemorrhage in rats by Miller *et al.* (2008b), bioeffect thresholds were determined for ultrasound exposure with diagnostic ultrasound machines and with a laboratory system set up to simulate diagnostic scanning. The ultrasonic waveforms (pressure vs. time) used for the driving pressure in this study were based on the laboratory system bioeffect thresholds at 1.50, 2.25, 3.50, 5.00 and 7.50 MHz (with corresponding bioeffects thresholds of 0.98, 1.31, 2.38, 2.82 and 6.00), which allowed more flexibility in producing the desired pulse waveforms than the diagnostic ultrasound machine.

The experiment was designed to simulate worst-case-scenario clinical conditions for CEUS. Anesthetized rats were held in place in a 75 L bath of 37° C degassed water, and exposed to ultrasound while receiving a constant 10 $\mu\text{l}/\text{kg}/\text{min}$ infusion of UCA. The ultrasound probe was placed such that its focal zone was at the cortex of the right kidney. The ultrasound system consisted of a transducer, power amplifier (A-500, Electronic Navigation Industries, Rochester NY), function generator (model 3314A function generator, Hewlett Packard Co., Palo Alto CA). Five damped single element transducers (Panametrics, Olympus NDT Inc. Waltham, MA) with 1.9 cm diam-

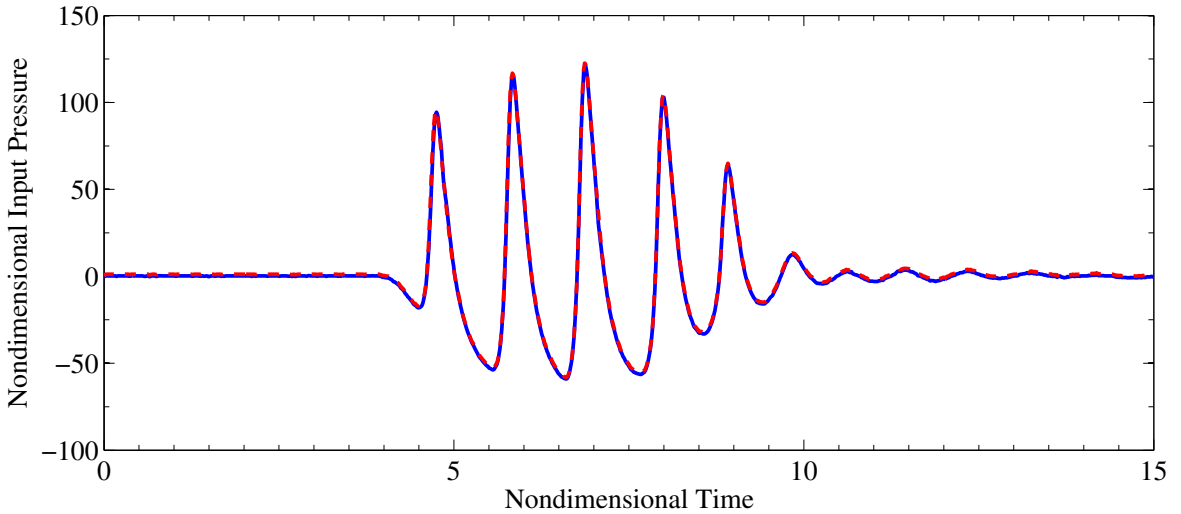


Figure 2.1: Experimental and numerical (filtered) pressure waveforms for the 7.5 MHz pulse at the threshold (Peak negative pressure: 6.0 MPa, 543 ns duration, $MI_{eq}=PRPA/f^{1/2}=2.2$). Solid: experimental; dashed: numerical.

eter and 3.8 cm focus were used at their resonant ultrasonic frequencies in a warmed water tank. The function generator was set using the n -cycle mode with $n = 3$ to produce a simple pulse train with pulse durations and PRPAs the same as used for the *in vivo* exposures. The waveforms were measured with a calibrated PVDF bilaminar film hydrophone with 0.4 mm spot size (model 805, Sonora Medical Systems, Longmont CO) and were adjusted to equal the threshold at each frequency and to several 3 dB increments above and below the threshold. The purpose of the progressive steps was to help identify any specific cavity behavior, which recurred at each frequency as the threshold was crossed. The hydrophone measured the alternating pressure including the PRPA, to which the constant atmospheric pressure must be added to obtain the total pressure. The highest PRPA available for the higher frequencies was limited by the transducers. The experimental waveforms are imported into Matlab, and smoothed using a moving-average low-pass filter. This procedure results in waveforms, such as that shown in Fig. 2.1 for the threshold at 7.5 MHz, in which the high-frequency experimental noise is removed. The smoothed waveforms are then input into the bubble dynamics code as the driving pressure.

Parameter	Dimensional value	Dimensionless number
Viscosity	$\mu = 0.015 \text{ (Pa s)}$	$\mapsto Re = \rho u R_o / \mu = 2/3$
Elasticity	$G = 10^5 \text{ (Pa)}$	$\mapsto Ca = \rho u^2 / G = 1.0$
Surface tension	$S = 0.056 \text{ (N/m)}$	$\mapsto We = \rho u^2 R_o / S = 2$
Sound speed	$c = 1570 \text{ (m/s)}$	$\mapsto C = c/u = 157$

Table 2.1: Base physical parameters representative of soft tissue used in the present study.

2.3.2 Bubble Dynamics Model

The bubble dynamics are modeled under the assumption that a single spherical gas bubble is subjected to a far-field pressure change (ultrasound pulse) in an infinite medium of uniform properties. Given that bioeffects are observed in some of the experiments and that it is likely that inertial cavitation occurs, it is expected that compressibility of the surrounding medium matters. Furthermore, tissue is expected to behave in a viscoelastic fashion. To account for all of these elements, the Keller-Miksis equation (Keller, 1980), a compressible extension of the Rayleigh-Plesset equation, is considered, and the constitutive relation between the stresses and strains follows a Kelvin-Voigt viscoelastic model, as in Yang & Church (2005). Thus the nondimensional equations governing the bubble dynamics are:

$$\left(1 - \frac{\dot{R}}{C}\right) R \ddot{R} + \frac{3}{2} \left(1 - \frac{\dot{R}}{3C}\right) \dot{R}^2 = \left(1 + \frac{\dot{R}}{C}\right) \left[p_B - 1 - p_a - \frac{R}{C} \frac{dp_a}{dt} \right] + \frac{R}{C} \dot{p}_B,$$

where $R(t)$ is the bubble radius, C is the dimensionless sound speed, p_a is the time-varying component of the far-field pressure and the dot represents material (time) derivatives. The bubble pressure p_B is given by

$$p_B = \left(1 + \frac{2}{We}\right) \frac{1}{R^{3\gamma}} - \frac{2}{WeR} + \tau_R, \quad (2.1)$$

where We is the Weber number (dimensionless surface tension), γ is the specific heats ratio for the gas, and τ_R is the shear stress in the rr -direction evaluated at $r = R$.

As in Yang & Church (2005), the Kelvin-Voigt model is used as the constitutive relation be-

tween the stresses and strains:

$$\tau_R = -\frac{4}{3Ca} \left(1 - \frac{1}{R^3} \right) - \frac{4}{Re} \frac{\dot{R}}{R}, \quad (2.2)$$

where Re is the Reynolds number (dimensionless viscosity), and Ca is the Cauchy number (dimensionless elasticity). The dimensionless numbers are defined in Table 2.1. The resulting system of equations is solved for the bubble radius using a fifth-order accurate Cash-Karp Runge-Kutta method with adaptive time-step control. In the problem under consideration, the pressure pulse is smooth and its wavelength is on the order of 1 mm. Since the bubbles are initially in the micron range and do not grow beyond a few initial radii, the present Rayleigh-Plesset-type approach is justified.

The base values for tissue properties, listed in Table 2.1, are taken from the literature (Apfel & Holland, 1991; Yang & Church, 2005). In the present work variables are nondimensionalized using a tissue density of $\rho = 1000 \text{ kg/m}^3$, a characteristic speed given by $u = \sqrt{p_{atm}/\rho}$ where p_{atm} is atmospheric pressure, and a characteristic equilibrium radius of $R_0 = 1 \mu\text{m}$. The resulting time scale is thus close to the Rayleigh collapse time. A range of equilibrium radii within 0.1-2.0 μm , a typical size distribution for UCAs, is considered. Thus, changing the equilibrium radius modifies the nondimensional parameters. The specific heat is taken as $\gamma = 1.13$ for perfluoropropane. Reported values of tissue elasticity fall in the 1-100 kPa range (Arda *et al.*, 2011). However, it is known that the elasticity may increase up to the MPa range at high strains (Krouskop *et al.*, 1998). Here, a nominal elasticity of $G = 100 \text{ kPa}$ is considered as the base case.

Since the thresholds for cavitation bioeffects are above the destabilization threshold, the microbubbles are modeled as free bubbles (Sboros *et al.*, 2002; Marmottant *et al.*, 2005), *i.e.*, UCA stabilizing films and shells are neglected. Additionally, the detailed effect of the physical constraint imposed by blood vessel walls is considered by including it in the bulk elasticity of the tissue. Though non-spherical perturbations may occur due to the local heterogeneity of tissue and thus lead to a significant change in the bubble dynamics, non-spherical collapse is expected to

produce lower temperatures and pressures (Johnsen & Colonius, 2009). In this sense, the spherically symmetric model represents a worst-case scenario useful in determining safe, conservative parameters for CEUS procedures.

2.4 Results and Discussion

2.4.1 Bubble Response

Typical bubble responses are first shown to provide a qualitative understanding of the physics. Figs. 2.2, 2.3 and 2.4 show the history of the dimensionless bubble radius produced by a given pressure waveform for a range of essentially linear to nonlinear cases, and different elasticities (5 kPa, 100 kPa and 1 MPa). In the linear case, the bubble oscillations are in phase with the pressure waveform. Increasing the elasticity leads to larger oscillation amplitudes, though the changes are small. At intermediate frequency and amplitude, the oscillations become larger and more nonlinear for larger elasticities. This observation, although seemingly counterintuitive, is consistent with the results of Johnsen & Hua (2012), who showed analytically that the damping of the oscillations is smaller in this range of elasticities. In the fully nonlinear case (large pulse amplitude and frequency), the oscillation amplitude becomes yet larger, thus yielding a larger maximum radius and very small minimum radius. For all elasticities, the initial behavior is similar up to the second maximum radius. Thereafter, the stiffer case ($G=1$ MPa) departs and collapses violently, while the other cases rebound. The maximum radius is achieved at approximately the same time in all cases, after the peak positive pressure. In all the simulations, the oscillations damp out rapidly after the passage of the pulse.

In the results of the following sections, the maximum dimensionless radius, R_{max} , and dimensional bubble temperature at collapse, T_{max} , obtained using the ideal gas law, are determined by recording their largest value over the simulation. These quantities are compared to the inertial cavitation thresholds used by Apfel & Holland (1991) and Yang & Church (2005): $R_{max} = 2$ and $T_{max} = 5000$ K. The dependence of the bubble dynamics on the pulse amplitude, initial bubble size

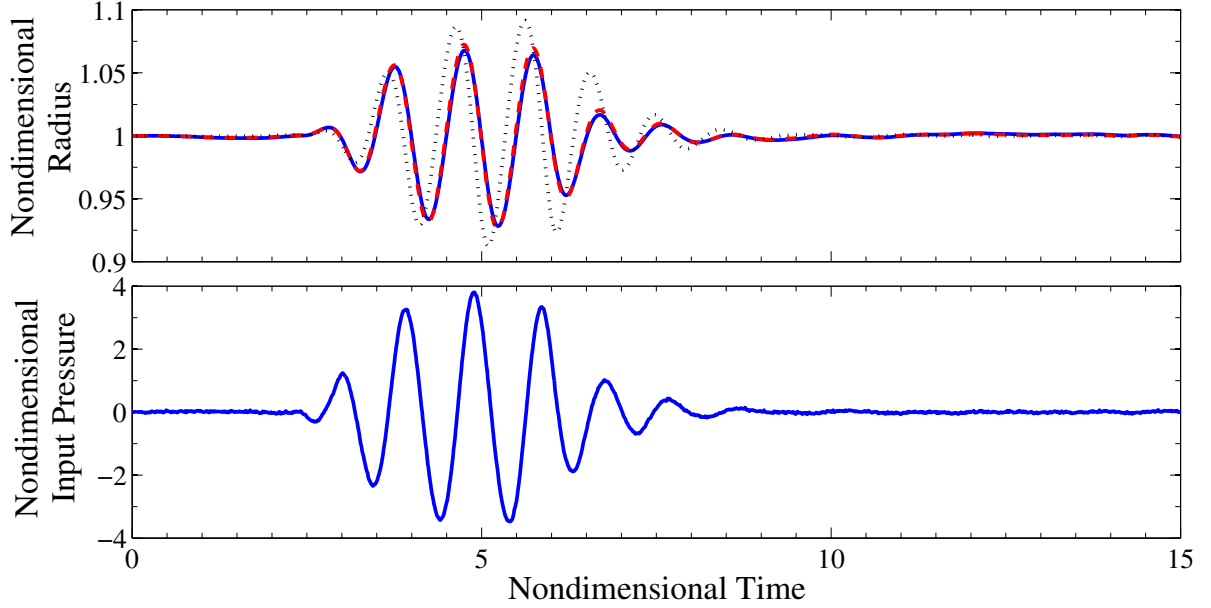


Figure 2.2: History of the bubble radius (top) and input-pressure waveform (bottom) for an essentially linear case (frequency: 1.5 MHz; peak negative pressure: 0.35 MPa). No bioeffects are observed here. $R_0 = 1 \mu\text{m}$; solid: $G = 5 \text{ kPa}$; dashed: $G = 100 \text{ kPa}$; dotted: $G = 1 \text{ MPa}$.

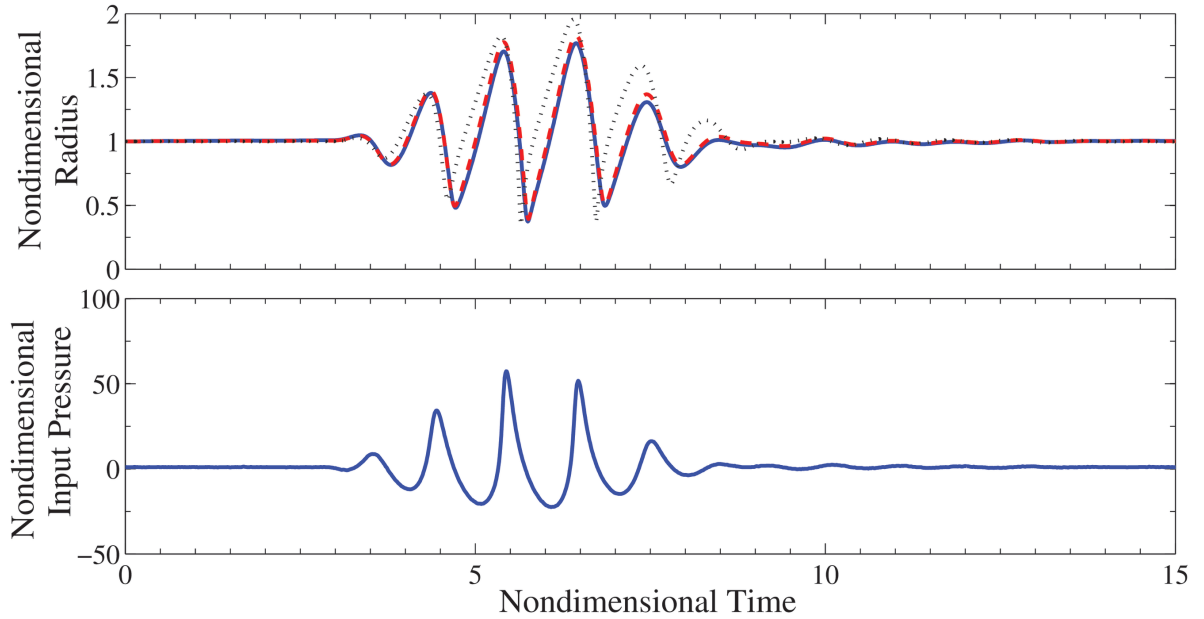


Figure 2.3: History of the bubble radius (top) and input-pressure waveform (bottom) for a moderately nonlinear case (frequency: 3.5 MHz; peak negative pressure: 2.4 MPa). Bioeffects are observed here. $R_0 = 1 \mu\text{m}$; solid: $G = 5 \text{ kPa}$; dashed: $G = 100 \text{ kPa}$; dotted: $G = 1 \text{ MPa}$.

(*i.e.*, UCA size distribution), pulse frequency, and tissue properties are considered individually.

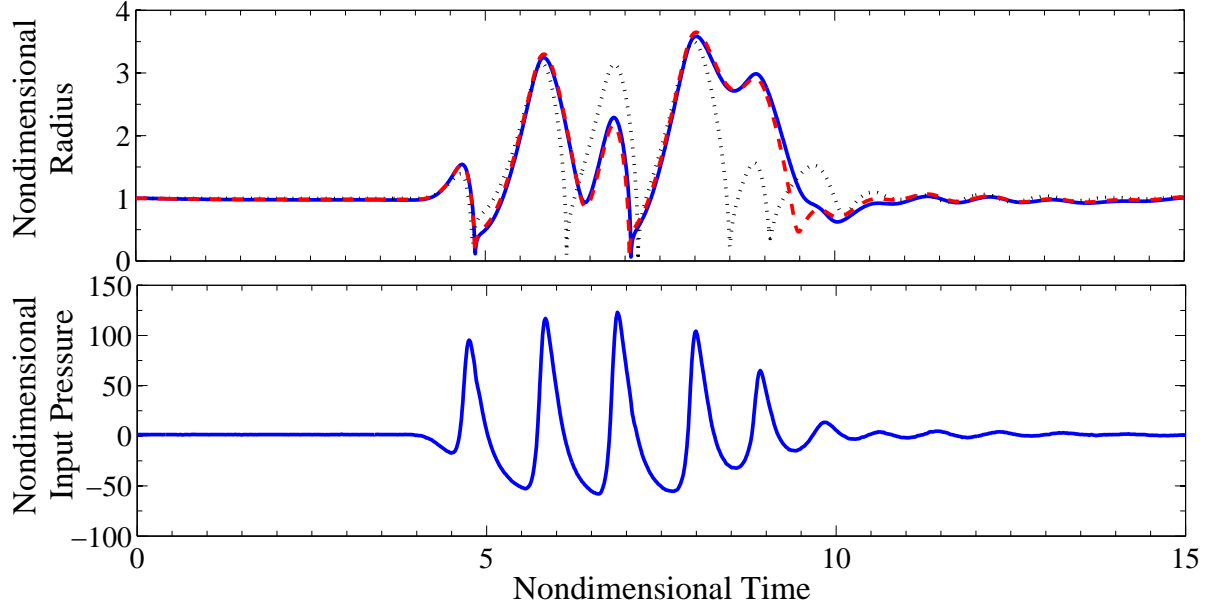


Figure 2.4: History of the bubble radius (top) and input-pressure waveform (bottom) for a highly nonlinear case (frequency: 7.5 MHz; peak negative pressure: 6.0 MPa). Bioeffects are observed here. $R_0 = 1 \mu\text{m}$; solid: $G = 5 \text{ kPa}$; dashed: $G = 100 \text{ kPa}$; dotted: $G = 1 \text{ MPa}$.

2.4.2 Dependence on the Pulse Amplitude

Given the strong dependence of the MI on the rarefactional pressure amplitude, the influence of the pulse amplitude on the bubble dynamics is first evaluated. Fig. 2.5 shows the dimensionless maximum radius as a function of rarefactional pressure amplitude. Initial bubble radii ranging between 0.1–2.0 μm are shown, as well as different frequencies. The open symbols denote cases where bioeffects did not occur, while the filled symbols denote the occurrence of bioeffects.

The results show that the bubble dynamics, through the maximum radius, scale with the pulse amplitude. Although the results do not collapse fully onto a line, a general trend is discernible. At low amplitude, the increase in the maximum radius is approximately linear; beyond some amplitude, the bubble undergoes nonlinear oscillations, thus explaining the different depended and larger spread. These results are consistent with the plots shown in Figs. 2.2-2.4. Over a broad range of amplitudes, the occurrence of bioeffects has little correlation with pulse amplitude alone: at a given amplitude, bioeffects may be observed or not, depending on the bubble size and pulse frequency. Only at very large pressure amplitudes ($\text{PRPA} > 4.20 \text{ MPa}$) are bioeffects systematically observed

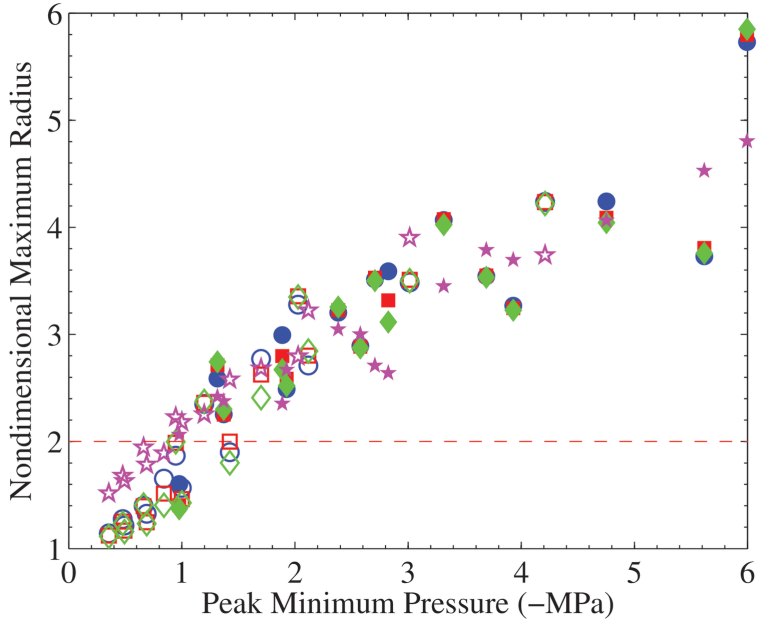


Figure 2.5: Dependence of the dimensionless maximum bubble radius on the peak negative pressure for $G = 100$ kPa. Empty symbols: no bioeffects; filled symbols: bioeffects. Pentagrams: $0.1 \mu\text{m}$; circles: $0.5 \mu\text{m}$; squares: $1 \mu\text{m}$; diamonds: $2 \mu\text{m}$; frequency: $1.5 - 7.5$ MHz.

regardless of the bubble size and pulse frequency. This behavior is not surprising, since at these amplitudes the bubble response is expected to be highly nonlinear. Conversely, at low amplitudes ($\text{PRPA} < 0.97$ MPa), the oscillations are linear and no bioeffects are observed, regardless of bubble size and pulse frequency. In this latter case, most bubbles whose R_{max}/R_o is below two do not exhibit bioeffects; however, this behavior depends on the value of elasticity, as shown in §2.4.5. Although not shown here for conciseness, similar results are obtained for peak positive pressure.

Similarly, the criterion $T_{max} > 5000$ K is not achieved with perfluoropropane. As shown in Fig. 2.6, the observed temperatures for PFP are far below this value, though the results for air approach it. This result is expected since the criterion was determined for air, which has a larger specific heats ratio ($\gamma_{air} = 1.4$) than PFP ($\gamma = 1.13$). The specific heats ratio appears in the internal gas pressure term in Eq. 2.1; its effect on the bubble dynamics is minor if the minimum radius is not very small, as in Fig. 2.6. Still, since the adiabatic relationships for an ideal gas are used, the temperature is significantly affected by the different specific heats ratio. Hence, even though the bubble dynamics are not strongly affected by the specific heats ratio, the maximum temperature is.

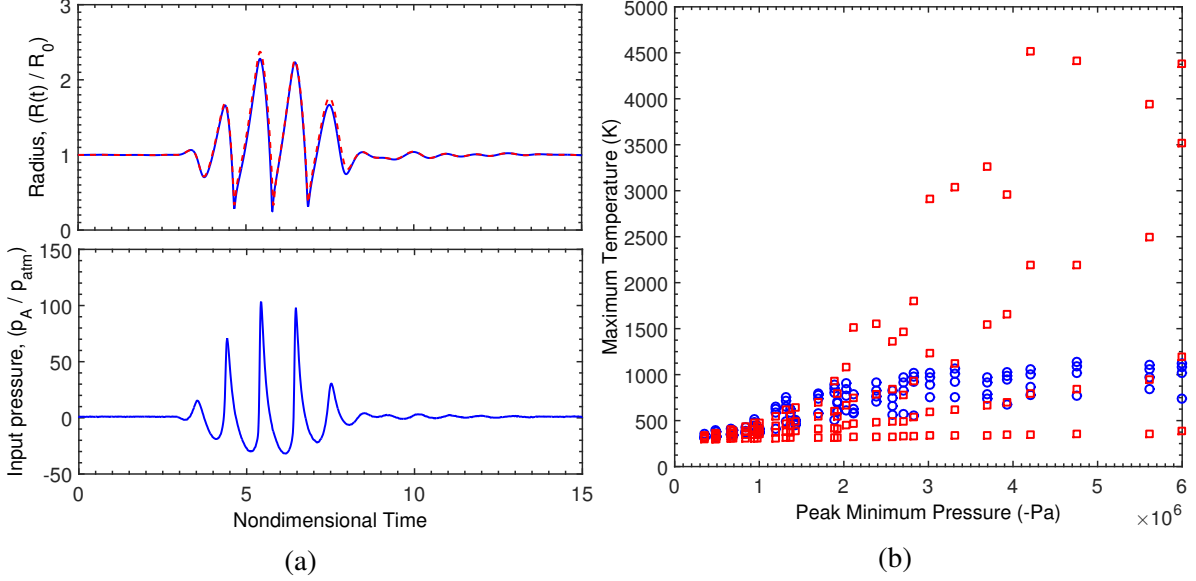


Figure 2.6: Dependence of the bubble dynamics on the gas contents ($G = 100$ kPa). (a) History of the bubble radius for PFP (solid) and air (dashed). $R_0 = 1 \mu\text{m}$; frequency: 3.5 MHz; peak negative pressure: 3.3 MPa. (b) Maximum temperature for PFP (circles) and air (squares). $R_0 = 0.1 - 2 \mu\text{m}$; frequency: 1.5 - 7.5 MHz.

2.4.3 Dependence on the Initial (Equilibrium) Bubble Radius

In the experiment, the size distribution of the UCAs is not known exactly. It is desirable to know whether the observed bioeffects are caused by all bubbles responding to the ultrasound, or whether a specific size is more likely to be responsible at the bioeffects threshold. To answer this question, for each experimental frequency, bubbles of different radii ranging from $0.1 - 2 \mu\text{m}$ are subjected to the pressure waveform corresponding to the bioeffects threshold amplitude. It should be noted that varying the equilibrium radius changes the non-dimensional parameters. Fig. 2.7 shows the maximum dimensionless radius, for both water (zero elasticity) and tissue (finite elasticity, $G = 100$ kPa), for the amplitude at which bioeffects are first observed at a given frequency.

Excluding the smallest size, the bubble response in tissue is monotone and changes little for a given frequency; there is no initial size that consistently leads to a dramatic response. The somewhat erratic behavior of the small bubbles may imply that such sizes are not present in UCA concentrations. On the other hand, the behavior is more irregular for water, particularly at small radii: for a given frequency, there is an optimal size that exhibits the largest response; these variations

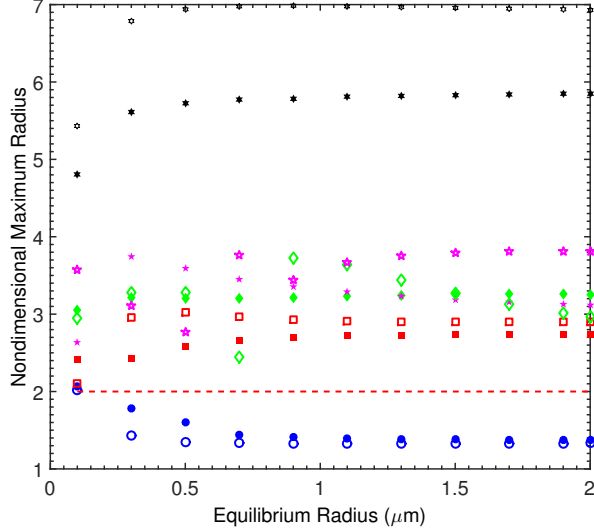


Figure 2.7: Dependence of the dimensionless maximum bubble radius on the initial bubble size for the amplitude at which bioeffects are first observed, at a given frequency, for $G = 100$ kPa. Empty symbols: water; filled symbols: tissue. Circles: 1.50 MHz; squares: 2.25 MHz; diamonds: 3.50 MHz; pentagrams: 5.00 MHz; hexagrams: 7.50 MHz.

are much larger than for tissue.

2.4.4 Dependence on the Pulse Frequency

The dependence of the bubble response on the pulse frequency is considered in this section. Fig. 2.8 shows the maximum dimensionless and dimensional radius for all initial bubble sizes and amplitudes vs. frequency. The square symbols denote cases in which bioeffects were observed in the experiments, while the circular symbols represent no bioeffects. The initial bubble sizes are not discriminated here for simplicity.

With the exception of a few outliers, a clear separation between cases for which bioeffects did and did not occur is observed; in other words, the bioeffects threshold has a strong dependence on the frequency. The trend appears to be approximately linear with frequency. Large growth may be achieved with no evident bioeffects, especially at high frequencies. The quantity R_{max} is a measure of cavitation collapse, since it is related to the available energy of the bubble. Thus, the present results indicate that cavitation collapse is expected to play an important role regarding bioeffects, although the precise mechanism cannot be inferred. Again, the existing criteria for inertial cavita-

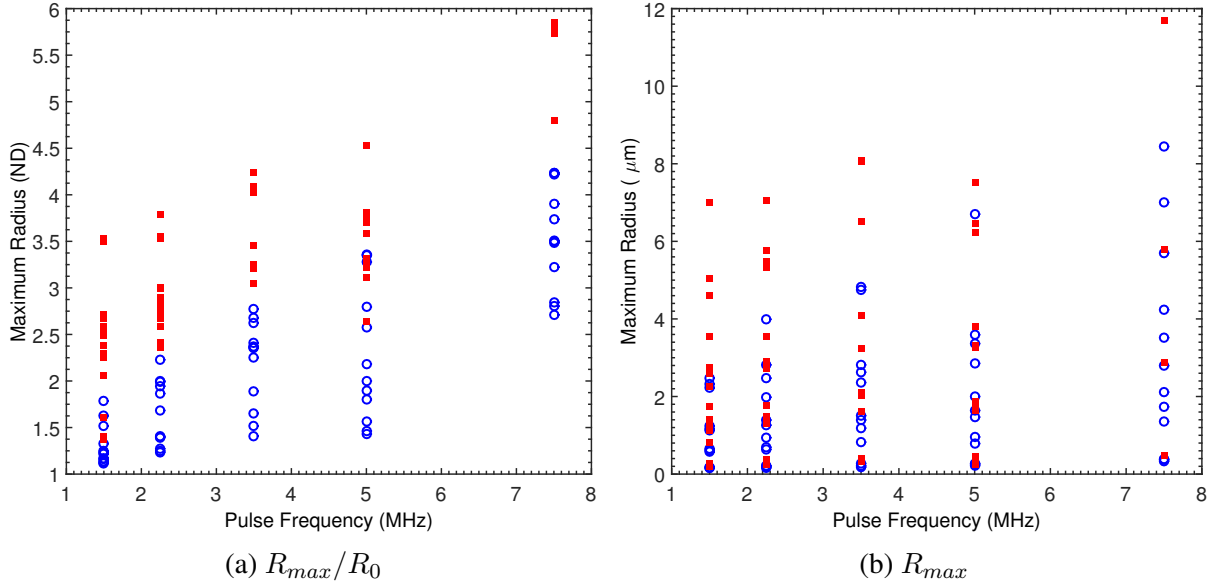


Figure 2.8: Dependence of the bubble dynamics on the frequency for $G = 100$ kPa. $R_0 = 0.1 - 2 \mu\text{m}$; empty circles: no bioeffects; squares: bioeffects. (a) Dimensionless maximum bubble radius. (b) Dimensional maximum bubble radius.

tion thresholds are frequency-independent and do not correlate well with the bioeffects threshold, which clearly shows a strong dependence on frequency.

Another hypothesis is that bubble growth may be responsible for capillary breaching. However, the plot of the dimensional maximum radius vs. frequency does not show systematic bioeffects beyond a certain size, *e.g.*, some capillary diameter. Thus, growth is not the sole mechanism by which bioeffects occur. However, the data remains inconclusive, due to the inability to identify the cases in which cavitation collapse is the dominant effect.

2.4.5 Dependence on the Tissue Properties

As suggested in Figs. 2.2-2.4, the bubble dynamics are sensitive to the tissue properties, specifically the elasticity. However, different types of tissue may have very different properties. Many of the measurements of tissue elasticity are made *in vitro*, and depend strongly on tissue preparation, storage, and degradation as well as method of measurement. Consequently it is possible that these measurements do not accurately represent the current behavior. To explore the effect of the elasticity on the results and the correlation to bioeffects, Fig. 2.9 shows the maximum dimension-

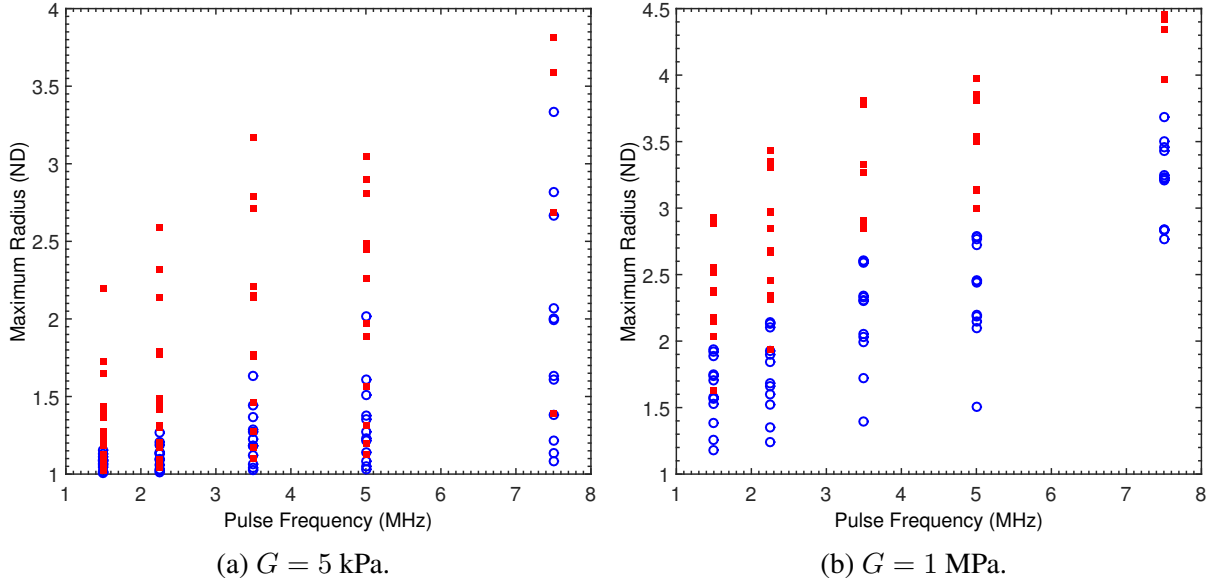


Figure 2.9: Dependence of the dimensionless maximum bubble radius on the frequency. $R_0 = 0.1 - 2 \mu\text{m}$; empty circles: no bioeffects; squares: bioeffects. (a) $G = 5 \text{ kPa}$. (b) $G = 1 \text{ MPa}$.

less radius for all initial bubble sizes and amplitudes vs. frequency for $G = 5$ kPa and $G = 1$ MPa. Although seemingly high, the latter elasticity is chosen to match the work of Yang & Church (2005).

The bubble dynamics and correlation to bioeffects significantly change when reducing the elasticity. For a value of 5 kPa, the discrimination is no longer clear. The bubble dynamics are closer to the behavior in water, such that different sizes may have dramatically different responses to the same waveform, as explained previously. On the other hand, the stiffer medium ($G = 1$ MPa) shows an even sharper demarcation, which again appears to be approximately linear. Given the sensitivity of the results on the elasticity, it is clear that more precise *in vivo* data is required for elasticities of tissues at the relevant strain rates.

Although not shown here, the type of viscoelastic model significantly affects the bubble dynamics (Johnsen & Hua, 2012; Patterson *et al.*, 2012a). For instance, a standard linear solid model, which includes stress relaxation in addition to elasticity, leads to very different maximum radii and oscillation properties (frequency and damping). For large relaxation times, elasticity variations become negligible.

2.5 Conclusions

In the present work, a numerical model is used to investigate experimentally observed bioeffects as a result of contrast-enhanced ultrasound. This work is unique in its combination of experimental results and numerical modeling. For the experimentally generated input pressure waveforms, it is known which of these triggered bioeffects, and from the numerical model we obtained calculated values for the dimensionless maximum radius and dimensional maximum temperature for each of these cases. By comparing the results of this study to previously established inertial cavitation thresholds used by Apfel & Holland (1991) and Yang & Church (2005), $T_{max} = 5000$ K and $R_{max} = 2$, it would appear that the inertial cavitation threshold does not play a role in determining the bioeffects threshold. However, it is unlikely that the inertial cavitation threshold is irrelevant. Instead, it is far more probable that these thresholds are not defined appropriately for cavitation in a viscoelastic medium, such as soft tissue. This work suggests the need for further experimental and numerical studies of cavitation in viscoelastic media.

The present work shows a strong correlation between cavitation dynamics and bioeffects when considering the pulse frequency. From the plot of maximum dimensionless radius vs. frequency, there is a clear separation between when bioeffects do and do not occur, and based on these results it appears that the frequency of the input pressure waveforms is of key importance to the definition of a bioeffect threshold, and likely the inertial cavitation threshold as well.

The present work shows that the elasticity of tissue significantly affects the bubble dynamics. This finding is perhaps not completely unexpected given that bubble dynamics are known to strongly depend on viscoelastic properties and model. The present study shows the need for more accurate measurements of material properties and for determining appropriate constitutive models for soft tissue, particularly at high strain rates. Finally, although the present work suggests that inertial cavitation collapse plays an important role with respect to bioeffects, it does not shed light on the exact mechanism, *e.g.*, shock emission upon collapse, growth beyond a given size, high temperatures generating free radicals, re-entrant jets in non-spherical collapse, etc. In future work we

plan on investigating this injury mechanism by conducting direct simulations of the full equations of motion for bubble dynamics in a viscoelastic medium.

CHAPTER 3

Dynamics of acoustically-driven gas-liquid interfaces: vorticity as a proposed physical mechanism for ultrasound-induced lung hemorrhage

3.1 Abstract

Over the past few decades, Diagnostic Ultrasound (DUS) of the lung has been shown to cause hemorrhage in a variety of mammals, though the underlying damage mechanism is yet to be determined. While there do not appear to be serious health risks associated with this problem under typical clinical conditions, the use of DUS for imaging of the lung is increasing rapidly. It is important we understand this phenomena to ensure that lung DUS remains safe as new procedures and technologies are developed. In this work we investigate the underlying physics associated with acoustic waves and liquid-gas interfaces and propose a previously unconsidered physical damage mechanism for DUS-induced Lung hemorrhage (LH). Specifically we propose that misalignments between ultrasound pressure gradients and tissue-air interface density gradients result in the generation of baroclinic vorticity, which could drive fragile cellular barriers around the alveoli to deform and ultimately hemorrhage. To investigate our hypothesis, we treat the lung as an inviscid, compressible fluid system and develop a simplified, numerical model of the problem to simulate DUS pulse-alveolus interaction. We show that acoustic waves, such as DUS pulses, are capable of generating baroclinic vorticity at sharp liquid-gas interfaces such as those found in the lungs, and that

this drives subsequent deformation of the interface. We perform analysis to describe the vorticity and interface dynamics and propose a scaling law based on dimensional analysis to predict the growth of a purely circulation driven interface. We compare predicted results with numerical experiments to verify that baroclinic vorticity is the mechanism responsible for the deformation.

Finally we suggest future work to be completed for this dissertation in the upcoming year. We plan to increase the relevance of this work to lung Ultrasound (US) by using more realistic geometries and computing theoretical stresses within the lungs. Additionally we will model the circulation and interface deformation associated with simple expansion and compression waves and use these models to design optimal waveforms for minimizing interface growth after the passage of the wave.

3.2 Introduction

3.2.1 A review of previous work on diagnostic ultrasound-induced lung hemorrhage

Diagnostic Ultrasound (DUS) is the safest form of medical imaging available today and has become ubiquitous in clinical practice. Currently, the only known bioeffect of non-contrast DUS known to occur in mammals is Lung hemorrhage (LH). The physical damage mechanisms underlying, DUS-induced LH are presently unknown, though the damage does not appear to be particularly severe, and is not considered a problem of significant clinical concern. However, it is an important problem to understand if we hope to improve lung DUS by expanding the US regimes used in clinical application. In this work, we use numerical experiments to investigate the underlying physics of DUS wave-lung interaction. We model the lung as a compressible multi-fluid system and solve the Euler equations of inviscid fluid motion to study the dynamics of fluid-fluid interfaces exposed to acoustic waves relevant to DUS. We observe that acoustically-generated vorticity at perturbed water-air interfaces drives the interface to deform. We hypothesize that a similar

mechanism may be responsible for deforming and ultimately rupturing the fragile tissue barriers around alveoli, tiny air sacs within the lungs, leading to DUS induced LH.

Ultrasound (US)-induced LH is not a new problem. It was first discovered in mice over 20 years ago (Child *et al.*, 1990). Since then, the use of lung DUS has become increasingly common in certain critical care situations (Lichtenstein, 2009). And there has been much work to better understand the problem of DUS-induced LH. Previous research has primarily aimed at three specific ends: (1) Determining the dependence of damage characteristics and thresholds on the characteristics of the US subject; (2) Determining the dependence of damage characteristics and thresholds on the US properties; and (3) Investigating the physical damage mechanism causing the hemorrhage. Our work aims to contribute to this third area by investigating the fundamental physics underlying the problem.

Work in the first area has considered species, age, physiological development, and pulmonary state of the US subject as possible variables which DUS-induced LH may depend upon. Within mammals, DUS-induced LH has been observed to be largely species indiscriminate and has been found to occur in mice, pigs, rats, rabbits, and monkeys (Baggs *et al.*, 1996; Child *et al.*, 1990; Dalecki *et al.*, 1997; Frizzell *et al.*, 1994, 2003; Harrison *et al.*, 1995; Holland *et al.*, 1996; Kramer *et al.*, 2001; O'Brien & Zachary, 1997; O'Brien *et al.*, 2001a, 2003a, 2005, 2000, 2001c; Penney *et al.*, 1993; Raeman *et al.*, 1993, 1996; Tarantal & Canfield, 1994; Zachary & O'Brien, 1995; Zachary *et al.*, 2001a,b). Dalecki *et al.* (1997) investigated the effect of age on DUS-induced LH in mice by exposing neonatal, juvenile, and adult mice to DUS pulses. The study found that while hemorrhage thresholds were similar in all mice, the degree of hemorrhage was much greater in the adult mice than in the younger subjects. Similarly, O'Brien *et al.* (2003a), studied the age dependence of hemorrhage in pigs, and found that older pigs had a significantly lower hemorrhage thresholds than juvenile and middle-aged pigs. In an unexpected result, the study also found that if one lung was exposed to US and the pig was then rolled over and the second lung exposed, the hemorrhage threshold in the second lung was substantially lower than in the first. In a separate study, O'Brien *et al.* (2002) subjected rats with variable degrees of lung inflation to DUS in order

to study the role of the impedance boundary condition at the lungs pleural surface on LH. It was found that rats with deflated lungs, that had less impedance mismatch with their surroundings, were more easily damaged than inflated lungs. While no direct experimentation has been performed on humans, for obvious ethical reasons, *Meltzer et al.* (1998) found that transesophageal echocardiography with similar US parameters to those causing lung hemorrhage did not lead to visible hemorrhage on the surface of the lung. While DUS-induced LH has not been shown to occur in humans, it has been demonstrated in a wide variety of mammals of varying age and size. The work presented here is not specific to any particular species or subject, but aims to consider the more general physical problem at hand.

The second area of research, investigating the dependence of lung hemorrhage on US properties, has seen the largest amount of work and is important for designing US in a way that is capable of high quality diagnostic imaging while minimizing any unwanted bioeffects. Research in this area has looked at the dependence of hemorrhage on US waveform and dosimetric properties. *Zachary & O'Brien* (1995) used continuous-wave and pulsed-wave US in mice, rabbits, and pigs, and found that while the continuous- and pulsed-wave-induced lesions appear macroscopically similar, they differ microscopically. Hemorrhage induced by continuous wave US consisted primarily of plasma and contained some cells, whereas pulsed-wave induced hemorrhage was composed largely of cells and contained little plasma. *Raeman et al.* (1996) subjected mice to pulsed US with varying exposure time and concluded that while threshold amplitudes appeared insensitive to exposure time, suprathreshold damage increased with increasing exposure. *O'Brien et al.* (2001b) investigated the effects of US beamwidth and found that as beamwidth increased so did the incidence, surface area, and volume of hemorrhage. It was noted that lung hemorrhage is perhaps the only known beamwidth-dependent mechanical bioeffect of US. *O'Brien et al.* (2003b) found evidence that increasing US pulse duration increases the likelihood of lung hemorrhage in rats. In this effort we consider the dependence of the alveolar wall dynamics on acoustic properties relevant to US, including acoustic wave amplitude, duration, and pressure gradient, which we relate back to US more closely in our discussion of our results (See Section 3.5.3).

While work in the third area of research, studying the cause of DUS-induced LH, has not yet led to a conclusive determination of the specific physical damage mechanisms, the most common ultrasound bioeffects mechanisms have been shown to be unlikely causes of the damage. [Zachary et al.](#) (2006) found that DUS-induced lung lesions do not appear similar to those induced by heat, and hence concluded that thermal damage mechanisms are unlikely. [O'Brien et al.](#) (2000) observed that the severity of DUS-induced LH in mice increased under raised hydrostatic pressure. And [Raeman et al.](#) (1996) notes that hemorrhage is unaffected by the introduction of US contrast agents into subjects. Both of these findings suggest that Inertial Cavitation (IC) is not a likely cause of DUS-induced LH. However, [Holland et al.](#) (1996) reports detecting cavitation during DUS-lung interaction in rats. [Tjan & Phillips](#) (2007, 2008) model DUS of the lung as an inviscid, free surface subjected to a Gaussian velocity potential and perform simulations to find that this setup can lead to the ejection of liquid droplets. They go on to say that DUS of the lung may similarly lead to ejected droplets capable of puncturing the air-filled sacs within the lung. Despite these efforts, the precise damage mechanism underlying DUS-induced LH is still unknown. In this work we propose a previously unconsidered mechanical damage mechanism and perform simulations to investigate its feasibility.

3.2.2 A review of previous work on driven fluid-fluid interfaces

Within the fluids community, there has been extensive research into the fundamental physics describing interactions between mechanical waves and fluid interfaces. Much of this research is motivated by applications in fusion energy and astrophysics and accordingly has investigated the Richtmyer-Meshkov Instability (RMI), in which a perturbed fluid-fluid interface is accelerated by a shock, causing the interface perturbation to grow ([Brouillette, 2002](#); [Drake, 2006](#)). The growth is driven by a sheet of baroclinic vorticity deposited along the interface as a result of misalignment between the pressure gradient across the shock and the density gradient across the perturbed interface. This physical mechanism by which these misaligned gradients create a torque on fluid particles and generate vorticity can be thought of in terms of a hydrostatic balance upon a particle.

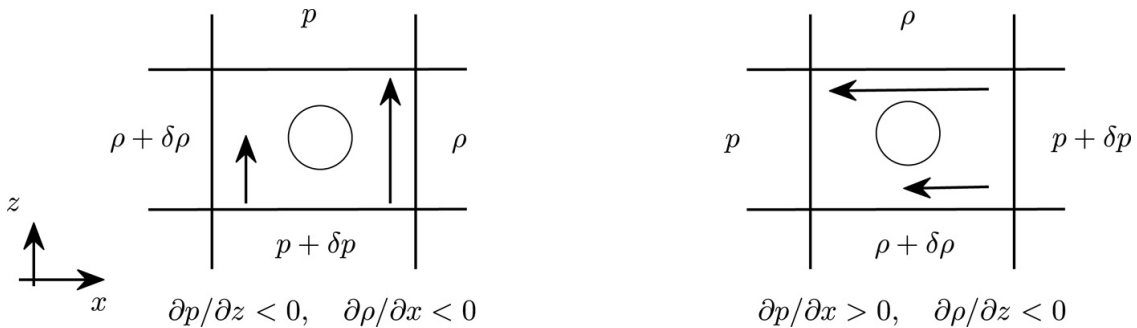


Figure 3.1: From [Heifetz & Mak \(2015\)](#). A hydrostatic force balance upon a particle subject to perpendicular pressure and density gradients illustrates baroclinic torque on a fluid particle.

Pressure gradients result in acceleration of the flow. This acceleration is inversely proportional to density, resulting in shear and vorticity [Heifetz & Mak \(2015\)](#). This is illustrated in Figure 3.1. The existence of baroclinic vorticity can be shown by taking the curl of the conservation of momentum equation for a compressible fluid, however we note that it is a nonlinear effect cannot be explained by traditional linear acoustics. 3.1 from [Heifetz & Mak \(2015\)](#).

For the classical RMI setup, a planar shock impinges normally upon the peaks and troughs of a sinusoidal interface. As the degree of misalignment varies along the interface, the interface is accelerated non-uniformly. The direction of the vorticity changes where the slope of the interface changes. This counter rotation on either side of interface peaks and troughs entrains nearby fluid causing interface peaks to accelerate in one direction and troughs to accelerate in the opposite direction. This results in a “bubble” of light fluid penetrating the heavy fluid, and a “spike” of heavy fluid penetrating the light fluid. How exactly this occurs varies slightly depending on the relative densities of the two fluids. For the case of a wave moving from a light fluid into a heavy one, the peaks and troughs of the interface are initially accelerated to move away from one another, and the interface perturbation amplitude undergoes growth exclusively. For the case of a wave moving from a heavy fluid to a lighter fluid, the peaks and troughs of the interface are accelerated such that they initially move closer to one another decreasing the perturbation amplitude. They then pass one another, inverting the phase of the interface perturbation, and then continue moving in opposite directions, growing the perturbation amplitude. This process is illustrated in Figure 3.2, which has been adapted from [Brouillette \(2002\)](#).

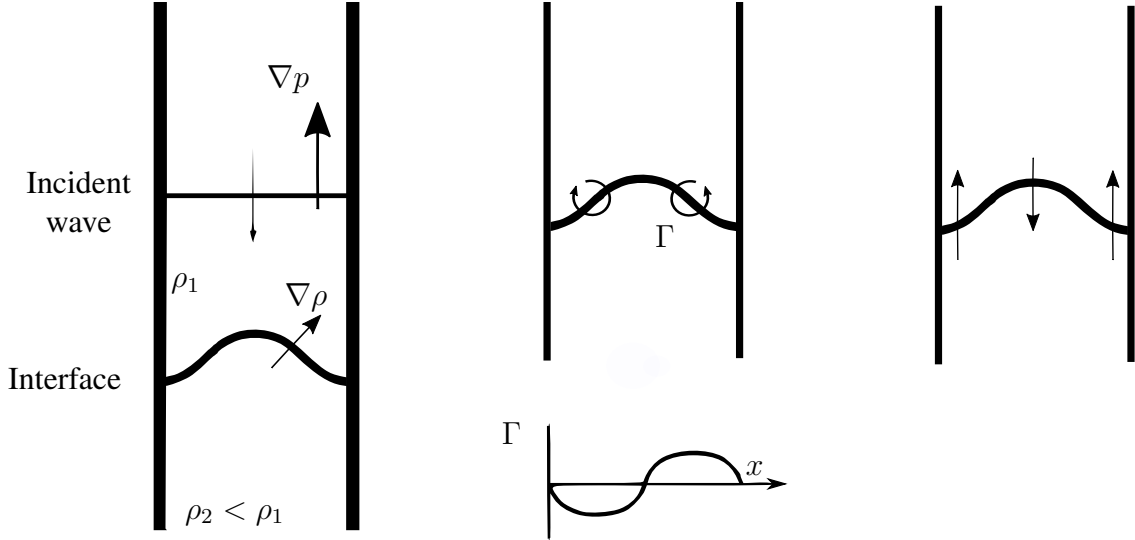


Figure 3.2: Adapted from [Brouillette \(2002\)](#). The RMI for a heavy-light interface is illustrated. The initial condition (left), circulation post wave-interface interaction (center), and perturbation growth (right) are shown.

Previous studies of the RMI has utilized theory, computation, and experiments to describe the behavior of the interface after the wave has passed. [Richtmyer \(1960\)](#) performed the linear stability perturbation analysis developed by [Taylor \(1950\)](#) for the case of an impulsive acceleration to create a model for the initial growth of the interface perturbation. [Meshkov \(1972\)](#) experimentally confirmed Richtmyer's qualitative predictions, hence the name of the instability. [Meyer \(1972\)](#) performed numerical simulations of the RMI and found good agreement with Richtmyer for the case of a shock impinging upon a light-heavy interface. [Fraley \(1986\)](#) used Laplace transforms in order to find the first analytical solution for the asymptotic growth rate for a shocked interface between perfect gases. To describe the late time, nonlinear growth of the perturbation, [Zhang & Sohn \(1997\)](#) used single mode perturbation, keeping many high order terms, to describe the velocity of the bubble and spike regions of the fluid. [Sadot *et al.* \(1998\)](#) combined the linear, impulsive solution with potential flow models of the asymptotic behavior of the bubble and spike to develop a model for the perturbation growth that is in good agreement with shock tube experiments for shocks with Mach numbers $\text{Ma}=1.3, 3.5$. Vortex theory has also been used to describe the behavior of the interface. [Jacobs & Sheeley \(1996\)](#) horizontally oscillated a container with two vertically stratified liquids to obtain standing waves and then bounced the container off of a coil

spring to study the incompressible RMI. The late time evolution of the interface is modeled using a row of line vortices to obtain qualitatively similar results to those experimentally observed, however the late-time growth rate is underestimated. [Samtaney & Zabusky \(1994\)](#) used shock polar analysis to find the circulation deposited by a shock on planar and non-planar interfaces. Their results are validated using an Euler code and found to be within 10% of the computed value for $1.0 < \text{Ma} \leq 1.32$ for all $\rho_2/\rho_1 > 1$, and $5.8 \leq \rho_2/\rho_1 \leq 32.6$ for all Ma. This work aims to add to the current body of work on this topic by investigating interfaces accelerated by pressure waves within the acoustic regime.

3.2.3 Explanation and contributions of the present work

We argue that the basic problem setup of the RMI, a mechanical wave impinging upon a material interface, is similar to DUS of the lungs. Accordingly we propose another possible damage mechanism of DUS-induced LH. We hypothesize that misalignment between the pressure gradients in the DUS pulses and the sharp density gradients across the tissue-air interfaces of the lungs creates a torque around the alveoli, which deforms and ultimately hemorrhages the alveolar walls.

The detailed nonlinear interactions between acoustic waves and perturbed fluid-fluid interfaces does not appear to have been previously studied in this manner or context. This work is separate from previous research into the RMI as a result of the acoustic waves being studied. Unlike shock waves, which occur over a few molecular mean free paths and interact nearly instantaneously, acoustic waves have a finite spacial wavelength and can occupy a much larger portion of space. Consequently, their interaction with interfaces occurs over a longer period of time, the duration of which depends on a variety of factors including shape and amplitude of the waveform, the speed of sound in the media, the relative orientation of the traveling wave and the interface (e.g., the shape of the interface). This duration can also be thought of in terms of the relative sizes of the physical features of the interface and the wavelengths of each feature of the acoustic wave of interest. Simple RMI analysis assumes an impulsive acceleration, and does not apply to this work because the interface has time to deform throughout its interaction with the wave. In this work

we demonstrate that the finite duration of the wave-interface interaction can effect the qualitative behavior of the on interface dynamics because of the interface deformation that occurs during this period. We will specifically attempt to address the following questions:

1. Are acoustic waves capable of generating sufficient baroclinic vorticity at perturbed fluid-fluid interfaces for substantial deformations?
2. what is the impact of the acoustic wave properties, such as amplitude and wave duration, on the vorticity and interface dynamics?

In the remainder of this work, we will first present a simplified model problem and a set of numerical experiments designed to investigate the fundamental physics underlying interactions between acoustic waves and perturbed interfaces between fluids. The simulation results and related analysis will be presented and discussed first in the context of the fluid dynamics. We will then draw from these results to further elaborate on the significance of these results as they regard to the motivating problem of DUS-induced lung hemorrhage. We will finally end by summarizing the main conclusions drawn from this work and suggest the next steps to be taken.

3.3 Methods

In this section, we describe the set of numerical experiments performed to investigate the fundamental fluid dynamics associated with acoustically-accelerated, perturbed liquid-gas interfaces and US-induced LH.

3.3.1 Problem set-up

The experiments are designed to model the physics associated with a DUS pulse propagating from soft lung tissue (modeled as water) onto a pulmonary alveolus (modeled as air). Accordingly, we consider a 2D, compressible inviscid fluid system in the xy -plane with an acoustic wave impinging from water (top) downward toward air (bottom). The water-air interface is initially located near

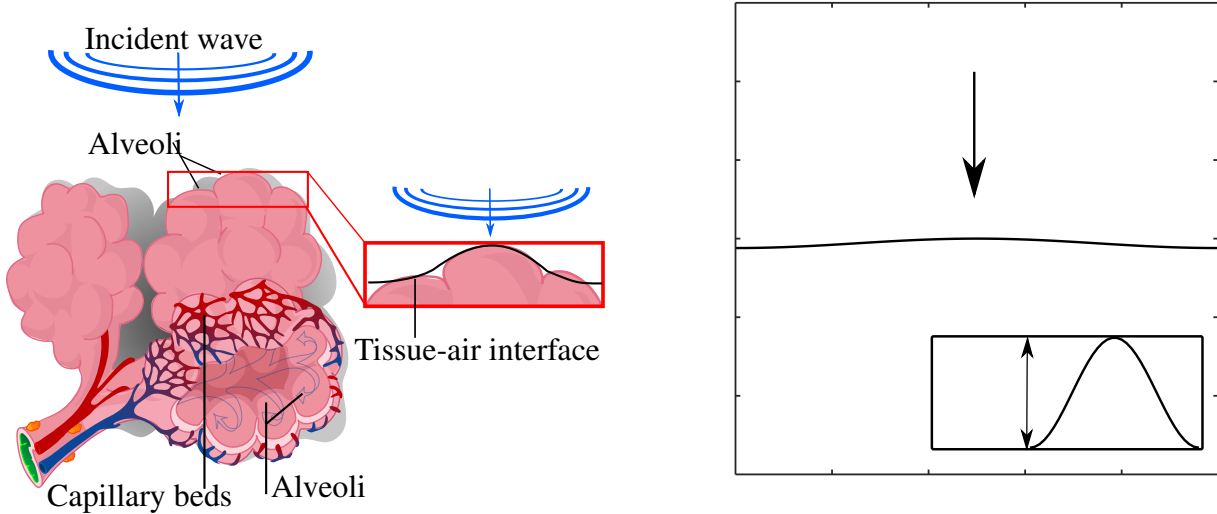


Figure 3.3: A schematic view of the physical problem (left) is shown next to a schematic view of initial setup and boundary conditions of the numerical experiments performed (right). A DUS pulse impinging from tissue onto a pulmonary alveolus is modeled as an acoustic wave impinging from water onto a sinusoidally perturbed water-air interface.

$y = 0$ and has a sinusoidal shape with wavelength λ and amplitude 0.03λ as seen in Figure 3.3. The width of the rectangular computational domain is 1λ such that it is traversed by a single period of the interface. This interface geometry is consistent previous studies of the RMI ([Brouillette, 2002](#)).

To model the DUS pulse we consider two different waveforms with different purposes. We design the first waveform to closely resemble a typical DUS pulse, in order to simulate the appropriate dynamics. The waveform shape is composed of a sinusoidal pressure modulated by a Gaussian envelope as seen in Figure 3.4),

$$p(t) = p_a \sin(2\pi f [(t - t_0)^2]) \exp\left(-\frac{t - t_0}{FWHM / (2\sqrt{2 \ln(2)})}\right). \quad (3.1)$$

Here $p(t)$ is the pulse pressure as a function of time, p_a is the maximum acoustic pressure, f is the frequency in Hz, t is time, t_0 is a time offset, and $FWHM$ is the full width at half maximum amplitude for the Gaussian envelope. The presented DUS- pulse waveform is given as a function of time, as is typical of US. The speed of sound in water is used to convert this to a spatial waveform for the initial condition.

Because A typical DUS pulse is mathematically complicated and not ideal for analysis we also use a trapezoidal waveform, which is sufficiently simple such that the relevant vorticity and interface dynamics can be studied analytically. To design this wave, we think of the ultrasound pulse as a sum of sin waves, each of which is composed of half-sinusoids, which can be approximated as trapezoidal waves. This thought process is illustrated in figure 3.4 (Left). Hence we use an initially symmetric trapezoidal waves.

Each wave is prescribed as an initial condition in the flow and is composed of three stages, described here in the order that they encounter the interface. First, compression occurs. Pressure increases linearly from atmospheric to a maximum of $p_a = 1, 5, \text{ or } 10 \text{ MPa}$ gauge pressure. Second, the elevated pressure p_a remains constant over a fixed distance (or time). Third, expansion occurs and pressure decreases linearly back to atmospheric pressure. The pressure rise and fall occur over equal distances 5λ , such that they have constant, equal slopes $\pm p_a/5\lambda$. Note that this neglects wave distortion due to acoustically induced changes in sound speed, which we assume to be small for our purposes. Unless otherwise stated, the period of constant pressure has length 35λ . Hence the total length L of the incoming trapezoidal wave is 45λ . We assume a typical alveolar length scale $\lambda = 100 \mu\text{m}$. For the wave initially in water, ($c=1500 \text{ m/s}$), we find an equivalent acoustic pulse duration of our waveform is $3 \mu\text{s}$. This is within the range of typical US pulse durations in clinical imaging ([Edelman, 2005](#)) and relevant research ([O'Brien, William D. et al., 2006](#)).

3.3.2 Governing equations

The governing equations describing the dynamics US lung interaction are conservation of mass, momentum, and energy for a compressible, viscoelastic material. In the present work we neglect elastic and viscous effects to arrive at the Euler equations of fluid motion, which we nondimensionalize by the density ρ and speed of sound c of air. For our setup we model the tissue as water and alveolus as air and the DUS pulse as a trapezoidal pressure waveform. Hence we solve the Euler equations to simulate simplified trapezoidal acoustic waves propagating from water towards

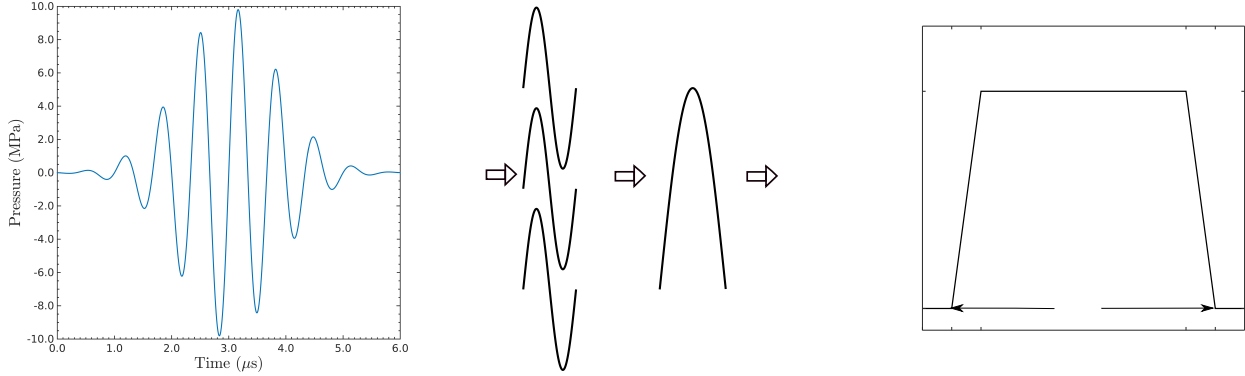


Figure 3.4: The initial pressure waveforms in the domain. A DUS pulse used as an initial condition (Left) is thought of as a sum of (half) sinusoids (Center), which can each be approximated as a trapezoidal waves (Right). The trapezoidal wave initial condition, shown as a function of vertical distance from the interface, is used for the bulk of this study.

a sinusoidally perturbed water-air interface. The interface and vorticity dynamics are studied.

It is worth noting that the Euler equations are length scale invariant, and thus no inherent physical length scale exists in the equations that we solve. Hence all length scales hereafter will be considered relative to an interface perturbation wavelength λ . Within the context of the DUS, λ can be thought of as a typical length scale of an alveolus.

We solve the dimensionless Euler equations of compressible, inviscid fluid motion in two dimensions (x, y) ,

$$\frac{\partial \rho}{\partial t} + \frac{\partial (\rho u)}{\partial x} + \frac{\partial (\rho v)}{\partial y} = 0, \quad (3.2a)$$

$$\frac{\partial \rho u}{\partial t} + \frac{\partial}{\partial x} (\rho u^2 + p) + \frac{\partial}{\partial y} (\rho u v) = 0, \quad (3.2b)$$

$$\frac{\partial \rho v}{\partial t} + \frac{\partial}{\partial x} (\rho u v) + \frac{\partial}{\partial y} (\rho v^2 + p) = 0, \quad (3.2c)$$

$$\frac{\partial E}{\partial t} + \frac{\partial}{\partial x} [u(E + p)] + \frac{\partial}{\partial y} [v(E + p)] = 0, \quad (3.2d)$$

where t is time, ρ is density, p is the pressure, u and v are the velocity components in the x and y directions respectively, and E is the total energy. We use the density and sound speed of air at 300 K to nondimensionalize the system. It is worth noting that the Euler equations are length scale invariant, and thus no inherent physical length scale exists in the equations that we solve. Hence

all length scales hereafter will be considered relative to an interface perturbation wavelength λ .

To close the system, we solve a stiffened equation of state which relate the total energy to the pressure and velocity in the flow, such that,

$$E = \frac{\rho(u^2 + v^2)}{2} + \frac{p + \gamma B}{\gamma - 1}. \quad (3.3)$$

Here B is a measure of liquid stiffness. For perfect gases, such as is our treatment of air, γ is the specific heats ratio and $B = 0$. The sound speed in our simulations is calculated based on the following relationship, derived from the stiffened equation of state.

$$c = \sqrt{\frac{\gamma(p + B)}{\rho}}. \quad (3.4)$$

While physical diffusion is not considered in this setup, numerical diffusion does occur at the water-air interface, creating a mixed region between the two fluids. The numerical treatment of the diffusion layer at the interface for the initial condition is such that the density has an exponential profile ([Latini et al., 2007](#)), which is used to get the mass fraction and molecular weight fields in the mixed region. Which then used to determine the other material parameters in the mixed region in a thermodynamically consistent fashion.

To solve for the material parameters in the mixed region and prevent spurious pressure oscillations at the interface, two additional advection equations are solved for γ and B .

$$\frac{\partial}{\partial t} \left(\frac{\gamma B}{\gamma - 1} \right) + \vec{u} \frac{\partial}{\partial x} \left(\frac{\gamma B}{\gamma - 1} \right) = 0, \quad (3.5a)$$

$$\frac{\partial}{\partial t} \left(\frac{1}{\gamma - 1} \right) + \vec{u} \frac{\partial}{\partial x} \left(\frac{1}{\gamma - 1} \right) = 0. \quad (3.5b)$$

This implementation is consistent with the works of [Abgrall \(1996\)](#); [Shyue \(2001\)](#); [Alahyari Beig & Johnsen \(2015\)](#). Details of this implementation are explained by [Henry de Frahan et al. \(2015b\)](#). The dimensional and dimensionless values of each fluid property can be found in tables 3.1 and 3.2 respectively.

3.3.3 Numerical methods

To solve the governing equations, we implement a third-order accurate Discontinuous Galerkin (DG) scheme in space and a fourth-order accurate, adaptive Runge-Kutta method to march forward in time (Henry de Frahan *et al.*, 2015b). Roe solver is used to calculate flux in and out of each cell in a way that handles discontinuities and keeps the interface sharp. As previously stated, the computational domain width (x -direction) is λ . The domain length (y -direction) is 80λ . The grid resolution is 100 points per λ unless otherwise stated. To minimize artificial reflections, we use inflow and outflow boundary conditions at the top and bottom of the domain, and implement geometric grid stretching in the vertical direction for the top and bottom-most 10λ segments of the grid. Periodic boundary conditions are used at the left and right edges of the domain.

3.4 Analysis

We perform analysis to make quantifiable predictions about the vorticity and interface dynamics. The results of these analyses are compared with the results of our numerical experiments in section 3.5.

To better understand the source of circulation within our problem we look to the vorticity generation equation for a 2D, inviscid fluid system,

$$\frac{\partial \vec{\omega}}{\partial t} + (\vec{u} \cdot \nabla) \vec{\omega} = -\vec{\omega} (\nabla \cdot \vec{u}) + \frac{\nabla \rho \times \nabla p}{\rho^2}. \quad (3.6)$$

Table 3.1: Dimensional properties of air and water used in simulations.

	Density, ρ^* (kg/m ³)	γ	B^* (Pa)	c^* (m/s) ($p=1$ atm)
Air	1.18	1.4	0	347.2
Water	996	5.5	492115000	1648.7

* indicates dimensional parameter

Each term in equation (3.6) represents a different physical mechanism by which the vorticity $\vec{\omega}$ is changing. The terms on the left-hand side of the equation represent changes in the existing vorticity field and the terms on the right represent vorticity sources and sinks. The first term on the left represents the total change of vorticity at a location in the flow field with respect to time. The second term on the left represents the advection of vorticity within the field. The first term on the right describes changes in vorticity due to compressibility. The last term on the right is the baroclinic term which represents vorticity generated by the misalignment of the pressure and density gradients in the flow. We seek to understand the relative importance of these mechanisms on the dynamics of the acoustically driven interface.

3.4.1 Order of magnitude analysis of vorticity generation mechanisms

To quantifiably compare the various mechanisms by which vorticity changes within the flow, we recognize that any vorticity generated must be a result of acoustic energy being converted to kinetic energy. As the only mechanism for this to occur in an inviscid fluid without pre-existing vorticity is baroclinic, we require misaligned density and pressure gradients. Hence we choose to perform our analysis at the water-air interface during the period in which the interface is interacting with the incoming wave. For simplicity, we narrow this down to only consider the period in which the incoming compressive portion of the wave encounters the interface. As this interaction occurs quickly, over an approximate time span $\Delta t_a \approx 5\lambda/c_w$, we assume that the interface is static and remains undeformed from its initial state during this interaction. We will show in section 3.5 that this assumption is reasonable for the cases considered. Having now established the point at which the analysis is to be performed we evaluate the order of magnitude of the compressible, advective,

Table 3.2: Dimensionless properties of air and water used in simulations.

	Density, ρ	γ	B	c
Air	1	1.4	0	1
Water	846.6	5.5	3469.1	4.75

Parameters are nondimensionalized by the density and sound speed of air.

and baroclinic terms of the vorticity generation equation (3.6). We note that the advective term is not a true source of vorticity, but is useful in understanding the change of vorticity at a given time and location within the flow.

In our evaluation of the order of magnitude of the individual terms of the vorticity generation equation (3.6), we treat gradient, curl, and divergence terms of any arbitrary quantity f such that $\nabla f = \mathcal{O}(|\Delta f|/\Delta L)$, $\nabla \cdot f = \mathcal{O}(|\Delta f|/\Delta L)$, and $\nabla \times f = \mathcal{O}(|\Delta f|/\Delta L)$. Here Δf is a change in f over a characteristic length scale ΔL . Because the only motion in the flow is generated by the acoustic wave. Accordingly, we consider acoustic pressure, velocity, and density perturbations such that $\Delta p = \Delta p_a$, $\Delta \vec{u} = \Delta \vec{u}_a$, and $\Delta \rho = \Delta \rho_a$, and use acoustic relations to relate these quantities (Anderson, 1990),

$$\Delta p_a = \pm \Delta u_a \rho c = c^2 \Delta \rho_a. \quad (3.7)$$

Additionally, to evaluate the expressions in this section we use the values in tables 3.1 and 3.2 consider our base trapezoidal wave case where $p_a = \Delta p_a = 10$ MPa. The length scale associated with the acoustic wave is the initial length of the pressure rise $\Delta L_a = 5\lambda$. The initial interface length scale ΔL_I , defined as the thickness of the mixed gas-liquid region of the interface from volume fraction of water $y_0 = 0.05$ to 0.95 volume fraction is estimated as $\Delta L_I \approx 0.05\lambda$. We approximate the order of theta based on its average value along a half-wavelength of the interface for our initial condition $a_0 = 0.03\lambda$ such that $\overline{|\theta|} \approx 0.12$.

To assess the baroclinic contribution to vorticity, we write the cross product of the density and pressure gradients as $|\nabla \rho| |\nabla p| \sin(\theta)$. Here θ is the angle between the acoustic pressure gradient, treated as constantly in the $+y$ -direction, and the direction of the density gradient which we treat as the outward normal direction to the interface. For $a_0/\lambda \ll 1$, we can approximate $\sin(\theta) \approx \theta$ at the interface. The density gradient due to the water-air interface is far greater than that due to the acoustic wave. As such we use the change in density across the interface $\Delta \rho_I$ and associated length scale ΔL_I to write the density gradient. The pressure change is a result of the acoustic wave, and

as such we use the acoustic pressure change Δp_a and associated length scale ΔL_a to express the pressure gradient. And thus we write the order of magnitude of the baroclinic vorticity generation term at the interface,

$$\left\| \frac{\nabla \rho \times \nabla p}{\rho^2} \right\| = \mathcal{O} \left(\frac{|\Delta \rho_I|}{|\Delta L_I|} \frac{|\Delta p_a|}{|\Delta L_a|} \frac{1}{|\rho|^2} |\theta| \right). \quad (3.8)$$

In the evaluation of the compressible and advective terms we consider two possible cases for the evaluation of the vorticity, based on whether the dominant vorticity arises from the acoustic flow-field or is baroclinically generated. Thus we will ultimately treat $\vec{\omega}$ as either the curl of the acoustic velocity field $\vec{\omega} = \nabla \times \vec{u}$ or the integral of the baroclinic vorticity generation term (3.8), treated as constant, over the characteristic time of the pressure rise $\Delta t_a \approx \Delta L_a / c_w$.

We first consider the case in which vorticity is predominately a product of the acoustic velocity field such that the approximate order of magnitude of the compressible contribution to vorticity generation is expressed as

$$\| -\vec{\omega} (\nabla \cdot \vec{u}) \| = \mathcal{O} \left(\left[\frac{|\Delta u_a|}{|\Delta L_a|} \right]^2 \right), \quad (3.9)$$

and for the advective contribution we find

$$\| (\vec{u} \cdot \nabla) \vec{\omega} \| = \mathcal{O} \left(\left[\frac{|\Delta u_a|}{|\Delta L_a|} \right]^2 \right). \quad (3.10)$$

We note that from this analysis, we expect the advective and compressible vorticity effects to be of the same order during considered period and will treat them as such for the remaining analysis.

Now, to compare the relative importance of the baroclinic and compressible (or advective) contributions to vorticity for this case we will look at the ratio of the two vorticity generation approximations. We divide equation (3.8) by equation (3.9) use (3.7) to express acoustic quantities in terms of the density perturbation $\Delta \rho_a$ and simplify,

$$\begin{aligned}
\frac{\left\| \frac{\nabla \rho \times \nabla p}{\rho^2} \right\|}{\| -\vec{\omega} (\nabla \cdot \vec{u}) \|} &= \mathcal{O} \left(\left(\frac{|\Delta \rho_I|}{|\Delta L_I|} \frac{|\Delta p_a|}{|\Delta L_a|} \frac{1}{|\rho|^2} |\theta| \right) / \left(\left[\frac{|\Delta u_a|}{|\Delta L_a|} \right]^2 \right) \right) \\
&= \mathcal{O} \left(\left[\frac{|\Delta \rho_I|}{|\Delta L_I|} \frac{|\Delta \rho_a|}{|\Delta L_a|} \frac{|c|^2}{|\rho|^2} |\theta| \right] / \left[\frac{|c|}{|\rho|} \frac{|\Delta \rho_a|}{|\Delta L_a|} \right]^2 \right) \\
&= \mathcal{O} \left(\frac{|\Delta \rho_I| / |\Delta L_I|}{|\Delta \rho_a| / |\Delta L_a|} |\theta| \right). \tag{3.11}
\end{aligned}$$

Evaluating the right-hand side of (3.11) using the previously described approximations and values we find that the ratio of baroclinic vorticity and compressible contributions to vorticity to be of order $\mathcal{O}(10^3)$.

As the previous result would suggest that baroclinic vorticity generation is strongly dominant, we must check the result by again evaluating the compressible and advective contributions to vorticity generation, using an expression for vorticity based on the time integration of (3.8),

$$\| -\vec{\omega} (\nabla \cdot \vec{u}) \| \sim \| (\vec{u} \cdot \nabla) \vec{\omega} \| = \mathcal{O} \left(\frac{|\Delta u_a|}{|\Delta L_a|} \frac{|\Delta \rho_I|}{|\Delta L_I|} \frac{|\Delta p_a|}{|\Delta L_a|} \frac{1}{|\rho|^2} |\theta| \frac{|c|}{|\Delta L_a|} \right). \tag{3.12}$$

Again, comparing the relative importance of the baroclinic and compressible (or advective) contributions to vorticity as we did before,

$$\frac{\left\| \frac{\nabla \rho \times \nabla p}{\rho^2} \right\|}{\| -\vec{\omega} (\nabla \cdot \vec{u}) \|} = \frac{c}{|\Delta u_a|} = \frac{\rho}{|\Delta \rho_a|} \tag{3.13}$$

Now evaluating this expression we expect that the relative contribution of baroclinic to compressible/advective vorticity generation is approximately of order $\mathcal{O}(10^2)$ at the end of the compression-interface interaction.

Comparing the evaluations of expressions (3.11) and (3.13) we expect two things. First, that baroclinicity will be the dominant physical mechanism by which circulation is generated. Hence, we expect that (3.11) is likely to overestimate the dominance of baroclinic vorticity after a small amount of baroclinic vorticity has been generated. Second, we expect the ratio of the baroclinic to

compressible contributions to vorticity generation will range from $\mathcal{O}(10^3)$ to $\mathcal{O}(10^2)$ during the compression-interface interaction.

3.4.2 Comparison of vorticity generation in air and water

Having established that the dominant source of vorticity is baroclinicity we now aim to determine where this vorticity will be generated within the mixed gas-liquid interface region. Specifically, we aim to compare the order of baroclinic vorticity generation from equation (3.8) in pure water and air. As this can already be evaluated in water from what we have provided up to this point, we will focus on evaluation of the order of baroclinic vorticity generation in air, from equation (3.8). Throughout the analysis we will denote the properties of the incoming wave and water with a subscript $-$, and the transmitted wave and air with a subscript $+$. For water, we will use the values for $\Delta\rho_I$, ΔL_I , $\Delta\rho_a$, ΔL_a and θ defined in the previous section based on our initial condition. Our treatment of the density gradient at the interface will remain unchanged for evaluation in air such that $\Delta\rho_I^- = \Delta\rho_I^+$ and $\Delta L_I^- = \Delta L_I^+$.

As a portion of the acoustic wave is transmitted into air, it undergoes several physical changes relative to the incident wave. To describe the properties of the transmitted wave in air we will borrow techniques from linear acoustics. To find the pressure change in the transmitted compression wave Δp_a^+ , we recognize that $a_0/\lambda \ll 1$ and treat the incoming wave as a plane wave impinging normally on a flat material interface such that $\Delta p_a^+ = \mathbf{T}\Delta p_a^-$, where \mathbf{T} is the acoustic transmission coefficient, $\mathbf{T} = 2\rho^+c^+ / (\rho^+c^+ + \rho^-c^-)$ (Kinsler *et al.*, 1982). For our water-air interface $\mathbf{T} \approx 4.97 \times 10^{-4}$. Because of the strong impedance mismatch between fluids, the acoustic wave is almost entirely reflected, decreasing the pressure gradient of the transmitted wave relative to the incident wave. Because of the drop in sound speed across the interface, the transmitted wave is compressed into a smaller physical area (i.e., the wavelength decreases) relative to the incoming wave, such that $\Delta L_a^+ = \Delta L_a^-(c^+/c^-)$. This effect increases the pressure gradient in the transmitted wave. To evaluate θ^+ , we utilize Snell's law which states that $c^- \sin(\theta^-) = c^+ \sin(\theta^+)$. Tedious, but simple geometric arguments can be used to show that because $a_0/\lambda \ll 1$ it is also

true that $\theta^- \ll 1$. Thus we use the small angle approximation of sin to find that $\theta^+ \approx \theta^- (c^+ / c^-)$. We note that this decreases the misalignment between the pressure and density gradients in air, and quantitatively approximately cancels the increase in pressure gradient due to the decrease in wavelength of the transmitted wave.

To determine where the vorticity will be generated at the interface, we consider equation (3.8) in air and water and write the ratio to find

$$\begin{aligned} \frac{\left\| \frac{\nabla \rho \times \nabla p}{\rho^2} \right\|_{air}}{\left\| \frac{\nabla \rho \times \nabla p}{\rho^2} \right\|_{water}} &= \mathcal{O} \left(\frac{\left[\frac{|\Delta \rho_I^+|}{|\Delta L_I^+|} \frac{|\Delta p_a^+|}{|\Delta L_a^+|} \frac{1}{|\rho^+|^2} |\theta^+| \right]}{\left[\frac{|\Delta \rho_I^+|}{|\Delta L_I^+|} \frac{(|\Delta p_a^+| / |\mathbf{T}|)}{|\Delta L_a^+| (|c^+| / |c^-|)} \frac{1}{|\rho^-|^2} (|c^+| / |c^-|) |\theta^+| \right]} \right), \\ &= \mathcal{O} \left(|\mathbf{T}| \left(\frac{|\rho^-|}{|\rho^+|} \right)^2 \right). \end{aligned} \quad (3.14)$$

For our water-air interface, we evaluate equation (A.1) to find that the ratio of baroclinic vorticity generation in air to that in water would be of order $\mathcal{O}(10^2)$. While this result considers vorticity generation in pure air and water, as opposed to the mixed fluid region relevant to this work, it provides a useful upper bound on the change we expect in the vorticity across the interface. Additionally, this result suggests that for the mixed water-air region, where the strongest density gradient exists, vorticity generation is likely to occur in areas with a lower volume fraction of water (i.e., gas-dominated fluid).

3.4.3 Considerations of circulation

In order to verify our analyses numerically we will consider not the vorticity generation, but rather the circulation and circulation generation as functions of time. As circulation is a global quantity of vorticity integrated over a region, it is more practical to compare to our numerical experiments. The expressions previously obtained for estimates of vorticity generation can be integrated in space to obtain integral expressions for circulation generation. As the expressions derived were approximate and spatially independent, we expect that the approximate vorticity relationships found in this section can be extended to considerations of the circulation. For instance, based on the results

of equation (3.13) we expect the baroclinic circulation generation in the left or right half-domain to be $\mathcal{O}(10^2)$ larger than the compressible and advective terms toward the end of interaction between the interface and the acoustic compression.

To access this, we integrate equation (3.6) over the half-domain, A_R , to get

$$\left(\frac{\partial \Gamma}{\partial t} \right)_{total} = \left(\frac{\partial \Gamma}{\partial t} \right)_{compressible} + \left(\frac{\partial \Gamma}{\partial t} \right)_{baroclinic} - \left(\frac{\partial \Gamma}{\partial t} \right)_{advective}, \quad (3.15)$$

Each term will be analyzed separately to determine the individual physical contributions to circulation. Here

$$\left(\frac{\partial \Gamma}{\partial t} \right)_{compressible} = - \int_{A_R} \vec{\omega} (\nabla \cdot \vec{u}) dA_R, \quad (3.15a)$$

$$\left(\frac{\partial \Gamma}{\partial t} \right)_{baroclinic} = + \int_{A_R} \frac{\nabla \rho \times \nabla p}{\rho^2} dA_R, \quad (3.15b)$$

$$\left(\frac{\partial \Gamma}{\partial t} \right)_{advective} = + \int_{A_R} (\vec{u} \cdot \nabla) \vec{\omega} dA_R. \quad (3.15c)$$

Finally, as we expect the interface growth to be purely circulation driven long after all waves have left the domain, we perform dimensional analysis to find a scaling law for the corresponding interface perturbation amplitude $a(t)$ as a function of circulation and time,

$$a(t) \sim \sqrt{\Gamma t}. \quad (3.16)$$

This proposed scaling law will be compared to the late time dynamics of the interface, after the acoustic wave has left the domain in Section 3.5.1.2.

3.5 Preliminary results and discussion

In this section we present the results of the numerical experiments and compare them to our analysis. We focus specifically on the vorticity/circulation and interface dynamics. We first investigate the response of the trapezoidal wave case in detail and then qualitatively compare this to results

for the US pulse case.

3.5.1 Interface response to the $p_a = 10$ MPa trapezoidal wave

3.5.1.1 Qualitative behavior of the interface and vorticity

To provide a qualitative understanding of the underlying physics, we consider our reference case in which a $p_a = 10$ MPa trapezoidal wave (See Figure 3.4) impinges on the water-air interface. Nearly all of the acoustic energy is reflected back into the water as a tension wave due lower acoustic impedance of the second fluid. The transmitted compression wave is weakly focused due to the sound speed mismatch across the curved interface perturbation. These reflected and transmitted waves dissipate at the inflow and outflow boundaries.

To illustrate the evolution of the interface and vorticity fields, Figure ?? contains color plots of the density (Top) and vorticity (Bottom) fields at different instances in the flow's evolution. Areas of high density (i.e., water) are dark blue and areas of low density (i.e., air) are light-blue. On the vorticity contours, counterclockwise (positive) vorticity is red, and clockwise (negative) vorticity is blue. The purpose of the vorticity plots is only to show the location and direction of vorticity at each time. For sake of visualization, the range of the vorticity color scale changes at each time slice because the vorticity spreads over time. Hence the vorticity magnitudes are not shown here. Contours of $y_0 = 0.5$ volume fraction are indicated in black on both plots.

The initially smooth interface perturbation grows from a smooth sinusoid to a sharp spike at late time. At $t = 1$, the compression-interface interaction has nearly completed and the vorticity is heavily concentrated in the air such that 97% of the total circulation in the left or right half domain exists in fluid with volume fraction of water $y_0 < 0.5$. This is qualitatively consistent with our analysis . As time progresses, it can be seen that the vorticity disperses throughout the domain, but remains concentrated around the interface and the vertical center of the domain.

To more closely exam the interface and circulation dynamics associated with the compression wave-interface interaction, Figure 3.6 shows the early-time histories of the interface amplitude

$a(t)$ and half-domain circulation Γ . t_{1-4} are the times at which the interface first encounters each features of the incoming wave: 1-pressure rise, 2-static elevated pressure, 3-pressure fall, and 4-return to ambient pressure. These points are denoted with black \times s along the curves in these figures and those hereafter. From $t_1 = 0^+$ to t_2 the compression wave encounters the interface. During this interaction the perturbation amplitude decreases, and the right half-domain circulation Γ rises sharply. At $t_2 \approx 1.1$, the pressure reaches its maximum amplitude, $p_a = 10$ MPa, and remains constant until t_3 . We note that at $\overline{a(t_{1-2})}/a_0 \approx 0.96$, suggesting that the static interface assumption made in our vorticity generation order of magnitude analysis was reasonable. The interface amplitude continues to decrease and the half-domain circulation Γ stops its rapid growth and changes little during this static elevated pressure period, until the expansion wave hits at t_3 . At $t \approx 5.0$, the perturbation undergoes a phase inversion and begins to grow, as is observed for the heavy-light interface Richtmyer-Meshkov problem. At $t_3 \approx 8.5$ the expansion wave first hits the interface. The perturbation amplitude continues to grow, and Γ increases sharply again. At $t_4 \approx 9.7$ the acoustic wave has finished traversing the interface, and atmospheric pressure is resumed. The perturbation amplitude a_0 continues to grow long after the wave-interface interaction has finished.

3.5.1.2 Dependence on acoustic wave amplitude

To investigate the dependence of the dynamics on the trapezoidal wave amplitude, we compare results for $p_a = 1, 5$, and 10 MPa while keeping the initial lengths of the wave L and the rise and fall ΔL_a constant such that p_a scales linearly with the acoustic pressure gradient. Figure 3.7, illustrates the interface amplitude and p_a -normalized circulation histories for $t \leq 25$, during and shortly after the wave-interface interaction. Black \times s along the curves indicate t_{1-4} , described previously in Subsection . During the interaction between the interface and the compression wave, the rate at which the perturbation amplitude decreases is greater for higher amplitude waves. The circulation deposited during this period scales linearly with p_a as is consistent with baroclinically-generated circulation based on our analysis. For the 10 MPa wave, the phase of the interface inverts

at, before the expansion hits, causing circulation deposited by the expansion to have the same sign as that deposited by the compression. For the 1 and 5 MPa waves interface phase inversion occurs after the expansion and consequently deposits circulation opposite that of the compression wave.

Figure 3.8 shows the interface amplitude and circulation histories for 5 and 10 MPa trapezoidal wave cases for $0 \leq t \leq 1000$. The perturbation amplitude history is plotted on logarithmically-scaled axes. For both waves, the slope of the perturbation amplitude is approximately 0.60 long after the waves have left the interface. This is slightly higher than the 0.5 slope predicted by scaling law (3.16). The results for the 1 MPa trapezoidal wave were not included because interface evolved too slowly to obtain useful data given the computational resources available.

3.5.1.3 Circulation and vorticity dynamics

We observe that the wave deposits a sheet of vorticity along the interface that moves with the interface in time. Figure ?? shows a surface plot of vorticity in the region of the domain around the interface for the 10 MPa trapezoidal wave case, at $t = 1.0$, during the middle of the interface-compression wave interaction (Left). Not shown is the rest of the domain, where vorticity was relatively insignificant. The vorticity is antisymmetric across the $x = 0.5$ center line. To analyze the physical mechanisms generating the vorticity, we plot each term of the circulation generation equation (3.15) during the period around the compression wave-interface interaction. Near the end of the interaction at $t = 1.0$, $(\partial\Gamma/\partial t)_{advection} = -5.3 \text{ e-}5$; $(\partial\Gamma/\partial t)_{compressible} = 2.7 \text{ e-}5$; $(\partial\Gamma/\partial t)_{baroclinic} = 7.7 \text{ e-}3$; $(\partial\Gamma/\partial t)_{total} = 7.7 \text{ e-}3$. This result is quantitatively consistent with expected vorticity generation based on our analysis (3.13). Furthermore, it supports our hypothesis that vorticity is primarily baroclinically generated.

3.5.1.4 Dependence on the length of the wave

To investigate the dependence of the dynamics on the length of the trapezoidal wave L , and comparably the wave-interface interaction time, we compare results for $p_a = 10$ MPa waves of constant rise and fall length ΔL_a . This effectively changes the time the interface has to evolve while experi-

encing the constant elevated pressure portion of the wave between the compression and expansion. Figure 3.10 shows the interface amplitude and circulation histories corresponding to waves with $L = 45\lambda, 35\lambda, 30\lambda, 25\lambda, 15\lambda, 10\lambda$ for $0 \leq t \leq 25$. For the three longest waves, $L \geq 30\lambda$, the expansion encounters the interface after the perturbation reverses phase. In these cases, the expansion deposits additional positive circulation along the right half of the interface. For the shorter waves, $L \leq 25\lambda$, the expansion encounters the interface before the perturbation reverses phase and the net half-domain circulation is decreased. Comparing cases in which the interface inverts phase before the expansion occurs the larger $a(t)$ is at the time, the more circulation is generated. The same is true when comparing cases in which the phase inversion occurs after the interface inverts phase.

3.5.2 Interface response to Diagnostic Ultrasound (DUS) waves

To evaluate the relevance of our trapezoidal wave experiments we simulate a $p_a = 1, 5$ and 10 MPa DUS pulse waves (See Figure 3.4) impinging onto the water air interface. In figure 3.11 we illustrate the circulation and interface amplitude histories for the $p_a = 10$ MPa DUS like-pulse case. The post-wave interface dynamics are similar to those observed for trapezoidal wave cases. During the wave-interface interaction, the interface amplitude is compressed overall, but oscillations are observed in correspondence with the acoustic pulse oscillations. After the wave has left the interface, the perturbation amplitude continues to decrease until the interface undergoes a phase inversion, after which the perturbation amplitude grows for the remainder of the simulation. half-domain circulation oscillates during wave-interface interaction before settling to a nearly constant non-zero value after the wave has passed. We note that the total circulation deposited is of the same order of magnitude as that generated by the trapezoidal wave of the same amplitude and duration. Qualitatively similar results were observed for the 5 MPa case. For the one 1 MPa case, the evolution of the system was slow such that running the simulation long enough to obtain useful results was computationally prohibitive.

3.5.3 Further discussion of the results

For both the trapezoidal and DUS pulse acoustic waves, the pressure, velocity, and density return to initial, ambient conditions after the passing of the wave. As these waveforms are continuous, this implies that the integral of the pressure gradient ∇p at each point along the interface, over all time must be zero. Hence we surmise that if the interface remains unchanged during the interaction with the wave, as it would for a wave moving with infinite velocity, $\nabla \rho$ remains constant and the net baroclinic circulation deposited must be zero. Thus for any finite duration acoustic wave such as ours to deposit net baroclinic circulation upon an interface, the interface itself must deform during interaction with the wave. This deformation alters the misalignment of the pressure and density gradients at the interface causing positive and negative circulation deposited to not cancel out entirely. Note that this is unique to waves that begin and end at the same pressure. This is not the case for the traditional RMI problem, for which conditions do not return to their original state after the passage of the shock.

For the cases varying the length of the static elevated pressure in the trapezoidal wave we previously noted that whether the expansion increased or decreased the total half-domain circulation depended on whether it encountered the interface before or after the phase change. If indeed circulation is driving the deformation of the interface, then changes in the waveform that appear to have little effect on the interface dynamics during the wave-interface interaction period, may have far more significant impacts on the long term dynamics of the interface. To put this in the context of DUS, which uses repeated pulses, if ultrasonically-deposited circulation is causing deformation within the lungs, longer Pulse Durations (PDs) may allow for greater deformation and increased circulation deposition as a result of any individual pulse. If the system acts as we have modeled it, the Pulse Repetition Frequency (PRF) would determine the degree of interface deformation experienced by pulses subsequent to the first and may influence deformation and hemorrhage. Finally, in recognition of the limitations of this study, we note that the true physical nature of lung tissue is viscoelastic (Bayliss & Robertson, 1939), and neither viscosity nor elasticity is included in our

model problems. While preliminary results with a Navier-Stokes code showed similar early time results, we expect that viscosity would dissipate circulation over a long enough period of time. Furthermore, elasticity may provide a mechanism by which the alveolar walls could resist deformation or retard to their original shape between pressure perturbations.

In the context of DUS, which uses repeated pulses, if ultrasonically-deposited circulation is causing deformation within the lungs, longer PDs may allow for greater deformation and increased circulation deposition as a result of any individual pulse. If the system acts as we have modeled it, the PRF would determine the degree of interface deformation experienced by pulses subsequent to the first and may influence deformation and hemorrhage. Finally, in recognition of the limitations of this study, we note that the true physical nature of lung tissue is viscoelastic (Bayliss & Robertson, 1939), and neither viscosity nor elasticity is included in our model problems. While preliminary results with a Navier-Stokes code showed similar early time results, we expect that viscosity would dissipate circulation over a long enough period of time. Furthermore, elasticity may provide a mechanism by which the alveolar walls could resist deformation or retard to their original shape between pressure perturbations.

3.6 Conclusions

This work is unique in that it demonstrates that acoustic waves may trigger significant deformation of perturbed liquid-gas interfaces over long periods of time. The driving mechanism behind this deformation is baroclinic vorticity, which occurs as a result of misalignment between the pressure gradient of the acoustic wave and density gradient of the perturbed interface. This mechanism arises as a result of nonlinear, compressible fluid mechanics, and cannot be predicted through traditional linear acoustics. We suggest that nonlinear effects such as baroclinic vorticity are important at liquid-gas interfaces, such as those in the lungs, because of the sharp density discontinuities between air and tissue within the lungs. To demonstrate this we simulate acoustic waves with properties relevant to DUS impinging from water into air.

The work presented here supports the following three conclusions:(1) Baroclinic vorticity generated by acoustic waves within the DUS regime is capable of significantly deforming perturbed liquid-gas interfaces. We observed that much of the vorticity generated by the acoustic wave at the interface remains with the interface as it evolves and deforms even long after the passage of all acoustic waves. Part of this is attributed to a lack of physical mechanism for dissipating vorticity in the inviscid case considered. From dimensional analysis we find scaling law (3.16), suggesting that the interface perturbation amplitude will grow as $t^{0.5}$ for purely circulation driven growth. In our computed results we find the actual perturbation amplitude grows as $t^{0.6}$. This discrepancy does not appear to change between $t = 500$ and 1000 and may be a result of the inability of a global quantity Γ to completely describe $a(t)$ which is governed by local fluid mechanics. (2) During interactions between acoustic waves and perturbed liquid-gas interfaces, baroclinic vorticity is predominantly deposited in the gas-dominated fluid. We perform analysis to predict that on either side of an infinitely sharp water-air interface, the vorticity generation rate would be approximately two orders of magnitude greater on the air side of the interface than in the water. This is qualitatively supported by our computational results which find that near the end of the initial compression wave-interface interaction nearly all of the circulation exists in fluid dominated by air. For the 10 MPa wave, for instance, 97% of the circulation is found in fluid with volume fraction of water $\alpha < 0.5$ at $t = 1$, after 91% of the compression has passed. (3) Changes in the acoustic waveform that have little effect on the interface dynamics during their interaction can substantially effect the interface over longer periods of time, via vorticity. By comparing the effects of 10 MPa trapezoidal waves with varying static pressure durations between compression and expansion, we observe that the evolution of the interface between these two wave components drastically effects the ultimate growth rate of the interface. The phase and amplitude of the interface perturbation at the time it encounters the expansion wave determine the direction and magnitude respectively of the vorticity deposited. Consequently, the amount of vorticity remaining at the interface and in the surrounding fluid after the passage of the wave changes greatly based on the time-dependent features of the wave.

This work is a step toward understanding the effects of acoustically generated vorticity on gas-liquid interfaces, however we acknowledge that there are many questions left to be answered. However, we consider our findings in the context of DUS-induced LH and propose a previously unconsidered potential damage mechanism. We hypothesize that baroclinic torque occurs at fragile air-tissue interfaces of the lung due to misalignment between the US pressure gradient and material interface density gradient, causing stress, deformation, and ultimately rupture at the interface. We note that evaluation of the hypothesized damage mechanism will require considerable further work including experiments, and numerical simulations that incorporate realistic viscosity, elasticity, attenuation, and realistic waveforms and lung geometries. This validation is beyond the scope of the proposed dissertation.

3.7 Future Work

Finally, we address some of the limitations of this study and propose future work to address some of these issues. To further evaluate the relevance of the proposed damage mechanisms and presented results to DUS-induced lung hemorrhage, viscous and elastic effects should be considered, as both of these have the potential to reduce observed deformation, and mitigate hemorrhage. Additionally, geometries that more accurately represent physical networks of alveoli within the lungs will be useful to understand the propagation of ultrasound waves and hemorrhage deeper into the lungs, beyond the first tissue-air interface. To do this accurately, it may be necessary to include a model for interface rupture. Many of these future tasks will require not only numerical efforts, but also experimental studies to appropriately characterize the lung tissue and validate the suggested models. Additionally, to increase our understanding of the relevant fluid dynamics, it would be useful to be able predict the circulation and interface dynamics based on the wave properties and initial conditions.

To address some of these issues and complete the proposed dissertation research we plan to perform several tasks:

- To further the relevance of this research to the problem of DUS of the lung we will:
 1. Calculate stresses and strains at the interface and compare to previously measured failure thresholds of the lungs. A passive viscous stress tensor will be computed from the velocity field and volume fraction fields, assuming constant viscosity for pure water and air. Either Volume fraction fields or Lagrange particles will be used to calculate the pathlength of the interface as a function of time $S_{Intf}(t)$ and engineering strain of the interface, ε_{Intf} , as though the interface were a solid sheet of tissue where, $\varepsilon_{Intf} = [S_{Intf}(t = 0) - S_{Intf}(t)]/S_{Intf}(t = 0)$.
 2. Investigate the effects of alveolar side wall structures. To model this, a thin layer of tissue (modeled as water) will be placed at the edges of the alveolus (modeled as air) and periodic boundary conditions will be used.
 3. Investigate the propagation of ultrasound waves and hemorrhage into the lungs. To model this we will modify the current geometry to such that a thin sinusoidal strip of water, parallel to the initial interface, will be placed every λ deep into the alveoli. This will be used with the alveolar walls described above to simulate a diagnostic ultrasound pulse propagating into a uniformly distributed alveolar network.
- To further our understanding of fluid mechanics associated with acoustically perturbed fluid interfaces we will:
 1. Seek to understand discrepancies between the $a(t) \sim \sqrt{\Gamma t}$ scaling obtained and the numerical results. This may require longer simulations to reach the final growth rate of the interface, or re-assessment of the logic behind using a global metric to describe a locally-dependent flow feature.
 2. Develop a model to predict the circulation deposited on a slightly perturbed interface by a simple compression or expansion wave. To do this, we will assume the interface is static during the interaction with the wave. Then, estimate the baroclinic term of the

vorticity equation based on known interface and wave properties and linear acoustic relationships between state variables.

3. Develop a model to predict the interface phase-reversal time for a simple compression wave. This model will be based on the expected compression of the interface due to the rising pressure during the interaction with the wave, and the subsequent circulation driven deformation described by scaling law (3.16).
4. Design acoustic waveforms that utilize time dependent features and interface deformation to generate minimal circulation and interface growth. To do this, we will aim to create waves that deposit vorticity of opposite sign and approximately equal magnitude before and after the interface phase change. One example of a wave that will be considered is a single period sinusoidal pressure wave that changes from the compression to expansion as the phase of the interface inverts.
5. Investigate the cause of late time circulation growth observed in some simulations. As can be seen from the circulation history for the 10 MPa trapezoidal wave in Figure 3.8, circulation continues to grow after all waves have left the domain. We plan to first determine if this effect is physical or numerical. If this effect is physical, we aim to determine the mechanism.

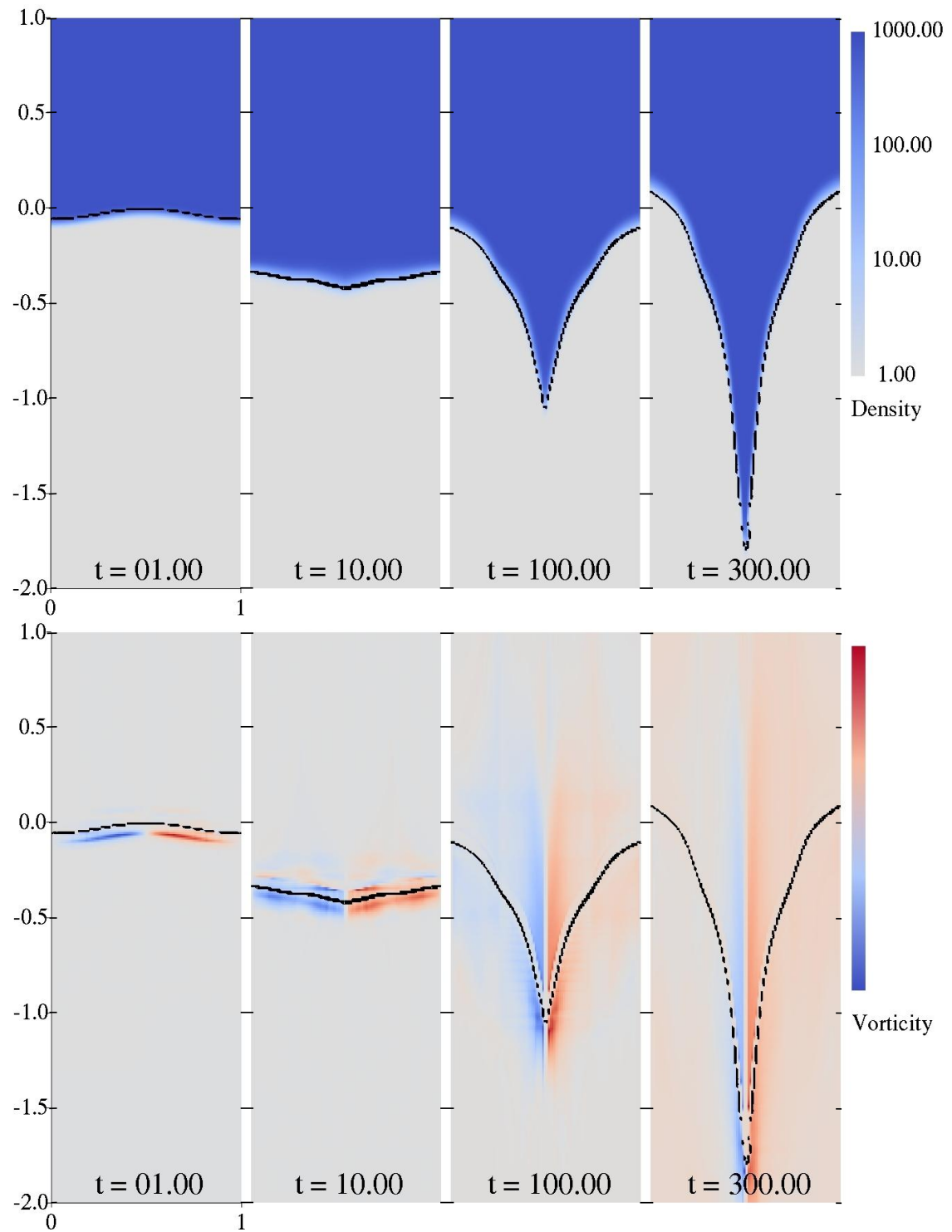


Figure 3.5: Surface plots of density (Top) and vorticity (Bottom) throughout the evolution of the interface for the 10 MPa trapezoidal wave case. Areas of high density (i.e., water) are indicated in dark blue. Areas of low density (i.e., air) are indicated in white. Positive (counterclockwise) vorticity is indicated in red, and negative (clockwise) vorticity can be seen in blue.

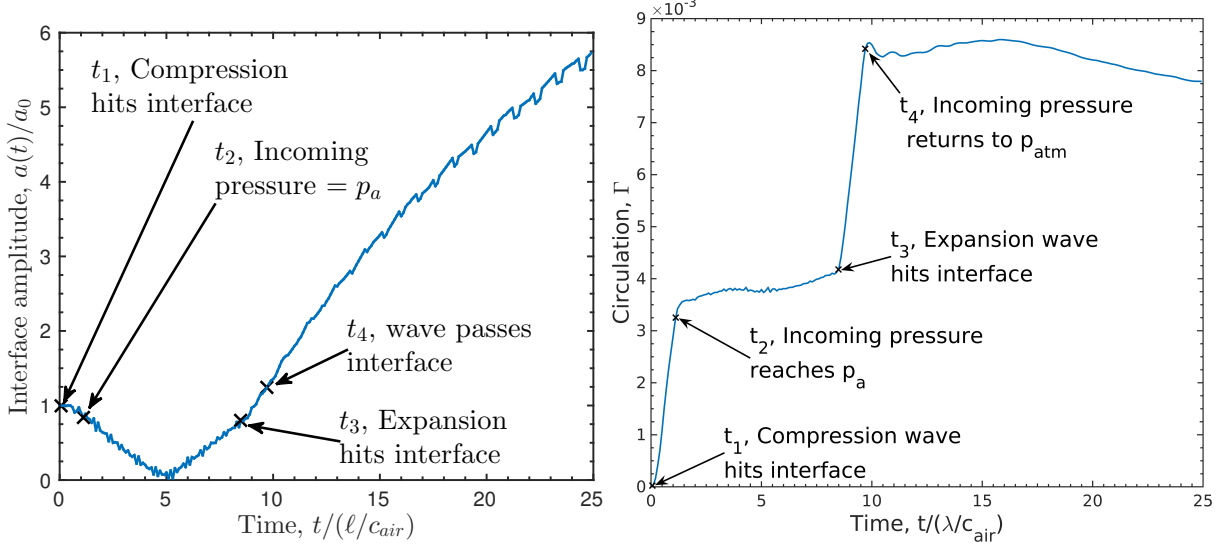


Figure 3.6: The interface amplitude (left) and circulation (right) histories corresponding to the 10 MPa trapezoidal waves are shown for $t \leq 25$. Indicated times, t_{1-4} , are the times at which different stages of the incoming trapezoidal pressure wave shown in Figure 3.4 first encounter the interface.

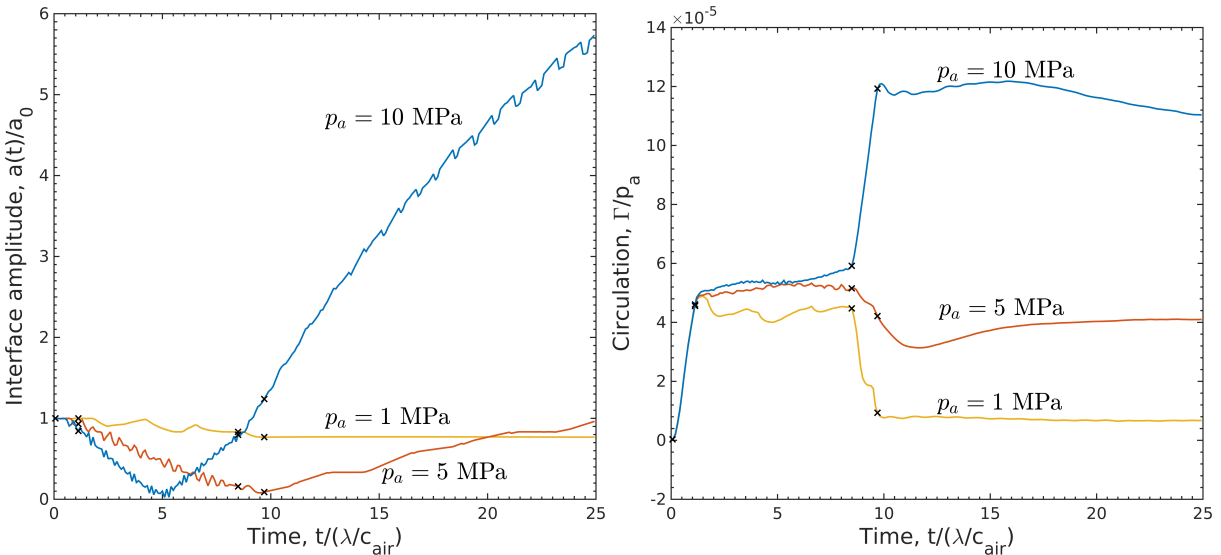


Figure 3.7: The interface amplitude (left) and circulation (right) histories corresponding to the 1(yellow), 5(orange), and 10(blue) MPa trapezoidal waves are shown for $t \leq 25$. The circulation history is normalized by the acoustic amplitude of the incoming wave to illustrate that circulation deposition by the compression wave scales linearly with p_a .

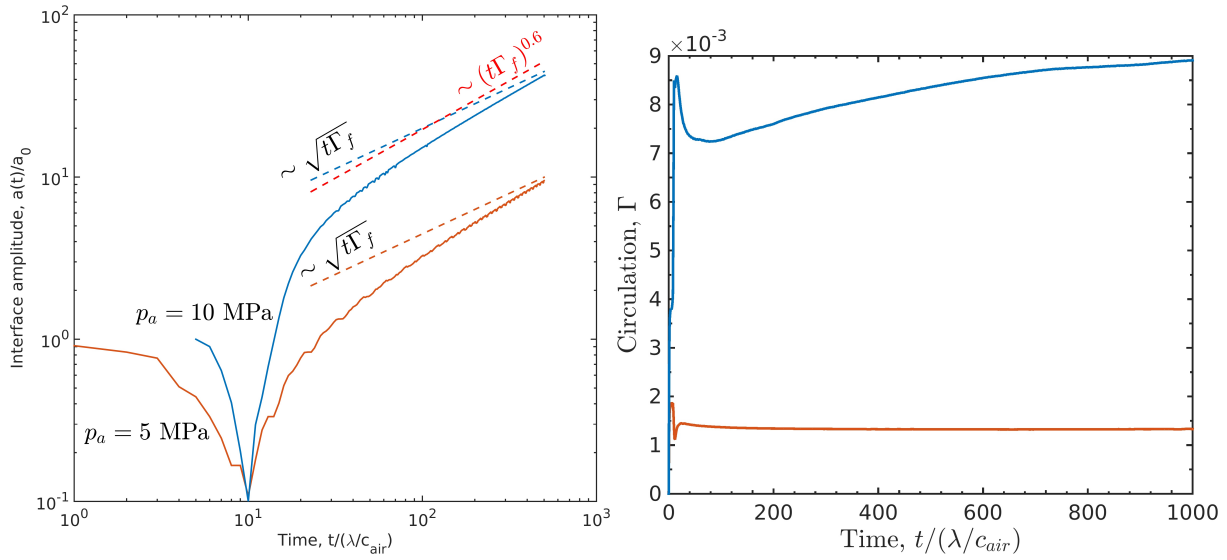


Figure 3.8: The interface amplitude (left) and circulation (right) histories corresponding to the 5(orange) and 10(blue) MPa trapezoidal waves are shown for $t \leq 500$. To appropriately compare late time dynamics, time has been offset in the interface amplitude history such that the phase reversal appears to occur simultaneously in both simulations. Dashed lines of the same color are used to demonstrate the expected slope of pure circulation driven interface growth, based on Equation (3.16). The red dashed line shows the slope we appear to be approaching for the 10 MPa wave case for the end time.

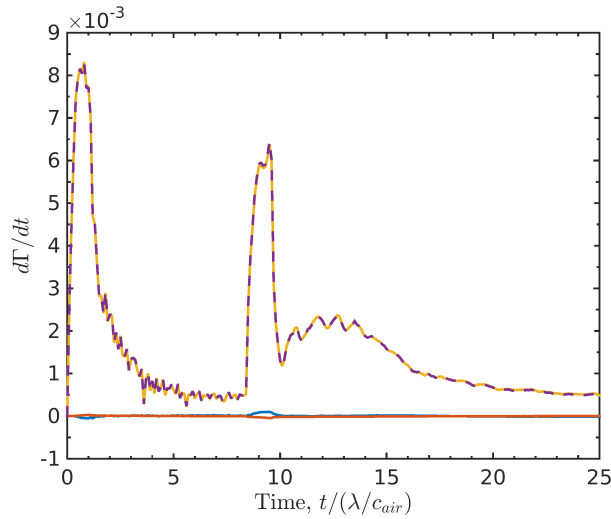


Figure 3.9: Each term of the circulation generation equation (3.15) is plotted as a function of time: $(d\Gamma/dt)_{advective}$ (blue), $(d\Gamma/dt)_{compressible}$ (orange), $(d\Gamma/dt)_{baroclinic}$ (yellow), $(d\Gamma/dt)_{total}$ (purple, dashed).

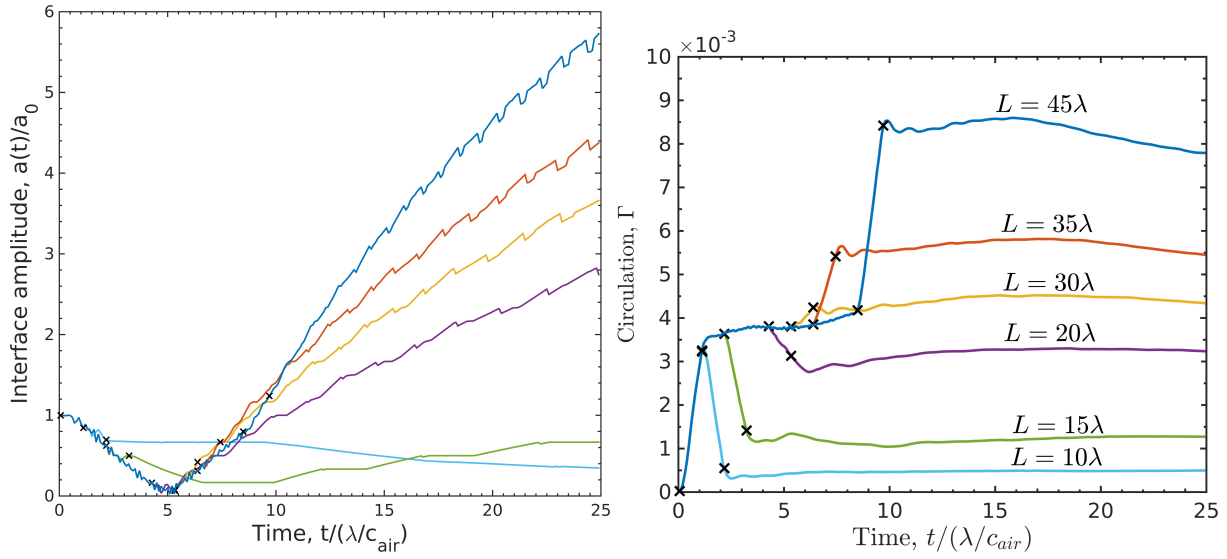


Figure 3.10: The interface amplitude (left) and circulation (right) histories for waves of varying total length L and elevated static pressure duration between the expansion and compression . Here we show results for $L = 45\lambda$ (blue), $L = 35\lambda$ (orange), $L = 30\lambda$ (yellow), $L = 20\lambda$ (purple), $L = 15\lambda$ (green), $L = 10\lambda$ (light blue)

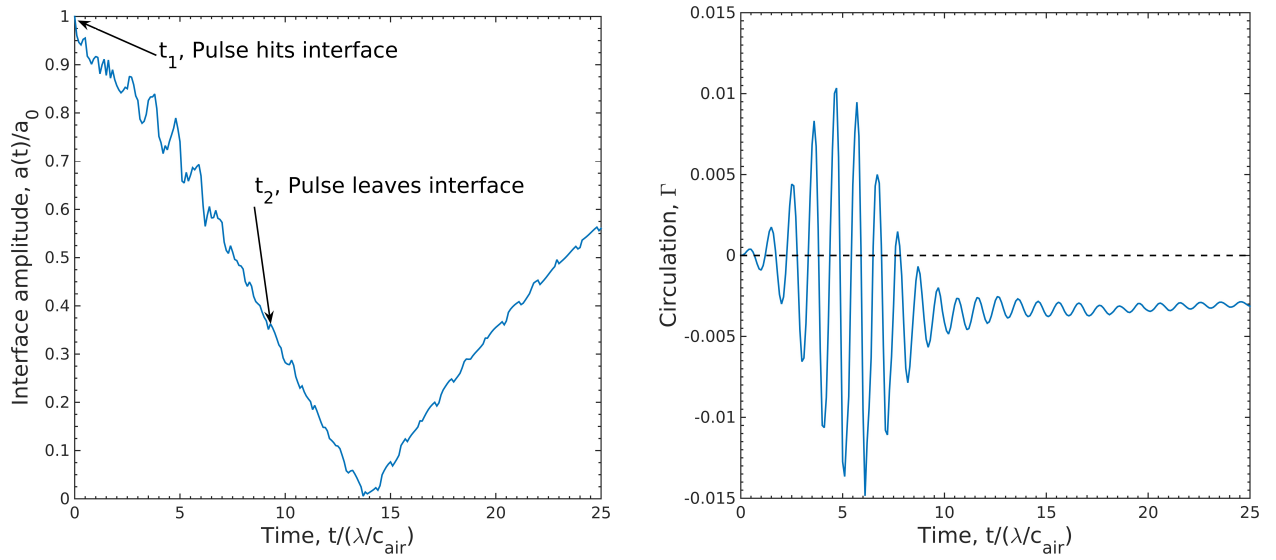


Figure 3.11: The interface amplitude (left) and circulation (right) histories corresponding to the a water-air interface disturbed by the US-like pulse shown in Figure 3.4.

CHAPTER 4

Relevance of the vorticity mechanisms to ultrasound

4.1 To Do:

- Save explanation of vorticity-driven interfaces / RM for results and discussion
- Add vorticity contours
- Add circulation plots
- Add summary of acoustic vorticity paper to intro (1 short summary paragraph)

4.2 Introduction

4.2.1 Problem Statement

This work aims to use computational modeling to investigate the cause of Diagnostic Ultrasound (DUS)-induced **PH!** (**PH!**).

4.2.2 Background

Ultrasound (US) is a powerful tool for medical diagnostics, and is one of the safest forms of medical imaging used today. Currently, **PH!** is the only biological effect known to occur as a result of non-contrast diagnostic ultrasound under clinically acceptable parameters Mechanical

Index (MI) \leq 1.9 (FDA, 1997). The physical mechanism underlying this damage is still not well understood. And, while DUS-induced PH! has not previously been observed in humans CITE, the use of DUS for lung imaging is growing rapidly for critical care situations (Lichtenstein, 2009). To guide the future of safe US practices, it is important that we understand the cause of DUS-induced PH!.

This work aims to use numerical simulations to investigate the dynamics associated with the interaction between a DUS pulse and an aleolar air-tissue interface. We hypothesize that acoustically generated baroclinic vorticity within the lungs is capable of driving deformation of alveolar air-tissue interfaces to the point of hemorrhage. We model the problem as a sinusoidally perturbed air-water interface driven by a single acoustic pulse and study the subsequent dynamics. Calculated stresses and strains are compared to previously measured failure criteria from the literature.

There has been a significant amount of previous research that is relevant to the problem of interest. This work arises from three different areas: Identifying the underlying mechanisms of DUS-induced lung hemorrhage; Determining the dependencies of DUS-induced lung hemorrhage on the properties of the ultrasound and subject (or the physical structure and mechanical properties of pulmonary tissue) and interactions between mechanical waves and interfaces between fluids.

The physical mechanisms underlying DUS-induced PH! are not well understood and traditionally expected US bioeffects mechanisms do not appear to be the primary cause of damage. US bioeffects mechanisms are typically classified as thermal or non-thermal with the bulk of non-thermal bioeffects being a result of acoustic Inertial Cavitation (IC). Zachary *et al.* (2006) finds that DUS-induced lung lesions do not appear similar to those induced by heat and concludes that thermal mechanisms are not likely to be the cause. O'Brien *et al.* (2000) observes that the severity of DUS-induced Lung hemorrhage (LH) in mice increases under raised hydrostatic pressure, and Raeman *et al.* (1996) finds that the LH is unaffected by the introduction of US contrast agents. Both of these findings are inconsistent with what would be expected of IC-induced hemorrhage. One study reports detecting cavitation during DUS-lung interaction in rats Holland *et al.* (1996). Tjan & Phillips (2007) considers another potential damage mechanism, that focused US may lead to the

ejection of droplets capable of puncturing the air-filled sacs within the lung. To investigate this, they perform numerical simulations of an inviscid, free surface subjected to a Gaussian velocity potential and show that the proposed droplet ejection may occur under certain circumstances. Similarly, Simon *et al.* (2012) observed High-Intensity Focused Ultrasound (HIFU) induced atomization of tissue at air interfaces. Despite these efforts, the precise damage mechanism underlying DUS-induced LH is still unknown.

The anatomical structure of the lungs is well documented, and the alveolar anatomy is of particular interest to the present work. The alveoli can be thought of as a network of openly connected, air-filled saccules with distinctly irregular surfaces. And while alveoli are irregularly shaped and do not have a true diameter, past research suggests that their size appears to be species dependent Faffe *et al.* (2002) and reported mean alveolar diameters range from tens to hundreds of microns with $45\text{ }\mu\text{m}$ in mice Knust *et al.* (2008) and $200\text{ }\mu\text{m}$ in adult humans Ochs *et al.* (2004). The alveoli are surrounded by a sheet-like web of blood-filled capillaries. Separating the blood from the air is a multi-layer wall of tissues, $0.2\text{-}0.3\mu\text{m}$ thick, referred to as the Blood-air Barrier (BAB) West (2000).

Normal tidal breathing can produce linear distension strains of 0-5%, with likely strains of 15-40% at total lung capacity (Roan & Waters, 2011).

Young's moduli of alveolar tissue depend on transpulmonary pressure, P_{tp} . Values range from $1.2 \times 10^4\text{ Pa}$ at low transpulmonary pressure (4cmH₂O) to 1.4×10^5 at high transpulmonary pressure (20cmH₂O) (Perlman & Wu, 2014).

Mechanical failure of the alveolar membrane leads to alveolar edema or frank hemorrhage West *et al.* (1991).

Pulmonary capillaries are almost completely unsupported by surrounding tissue West *et al.* (1991).

In addition to alveolar structure, the mechanical properties and failure behavior of pulmonary tissue are of broad, and have been studied extensively. West *et al.* (1991) Raised the pulmonary capillary pressure of anesthetized rabbits and found some disruption of capillary endothelium and

alveolar epithelium occurred for transmural pressures as low as 3.2 kPa and consistent disruption occurred for pressures \geq 5.3 kPa.

The morphology of DUS-induced lung hemorrhage is characterized by ...! (-induced lung hemorrhage is c

Within the context of DUS of the lung, hemorrhage has been observed for Peak Rarefaction Pressure Amplitude (PRPA) as low as 1 MPa CITE.

4.2.3 Summary

As DUS of the lung has been shown to trigger same-day, acute alveolar hemorrhage Zachary *et al.* (2001a), it is specifically interactions between the an aveolus and a single DUS pulse that we consider in this work. To investigate the mechanism underlying this hemorrhage, we develop a numerical model of this problem to compute the expected dynamics of the alveolar air-tissue interface for varying acoustic amplitudes an alveolar geometries. To relate the computed dynamics to lung hemorrhage, we approximate the relevant stresses and strains and compare these results to existing values of the material properties alveolar tissue to assess possible causes of hemorrhage.

4.3 Methods

In this section we develop a model of DUS-alveolus interaction as a compressible fluid system. We then describe in detail the setup of the numerical experiments performed and calculations performed to investigate the problem.

4.3.1 A model of DUS-alveolus interaction

COPIED THIS PARAGRAPH TO OTHER PAPER. Consider a DUS pulse as it travels into the lungs. After passing through layers of soft tissue and fluid, the wave encounters a network of openly connected, air-filled saccules with distinctly irregular surfaces. These are the alveoli. It is the interaction between an incident US pulse and the first alveolar tissue-air interface it encounters that we treat here, as shown in figure 4.1a.

To model the problem, we consider a rectangular domain with a 2D (x, y) cross section containing soft tissue (modeled as water) sitting atop a single alveolus (modeled as air) as illustrated in figure 4.1b. An acoustic pulse is prescribed within the water, above the interface, and allowed to propagate downward ($-y$ -direction) toward the air. The alveolus spans the width of the domain, ℓ . A typical mean aveolar diameters in an adult human is $200\mu\text{m}$ (Ochs *et al.*, 2004).

To capture the irregular shape of the alveolus, the water-air interface contains a single mode sinusoidal perturbation of amplitude a_0 such that the vertical center of the interface is described by,

$$Y(x, t = 0)_{interface} = a_0 \sin \left(\frac{2\pi x}{\ell} - \frac{\pi}{2} \right). \quad (4.1)$$

An interface thickness $\delta = 0.08$ is chosen such that at $t = 0$, the fluid in the domain above $y \geq Y_{interface} + \delta/2$ is pure water, and below $y \leq Y_{interface} - \delta/2$ is pure air, which a water-air mixture filling the region around the interface. A more detailed treatment of the interface can be found in referred to (Patterson and Johnsen, 2016). To investigate the dependence of the dynamics on the alveolar geometry we will consider multiple interface perturbation amplitudes: $a_0 = 0.03\ell, 0.1\ell, 0.2\ell$, and 0.3ℓ .

The diagnostic ultrasound pulse is modeled as a sinusoidal carrier wave of amplitude p_a and frequency f modulated by a Gaussian Envelope such that,

$$p(x, t_0) = p_a \sin \left(2\pi f \frac{[y - (Y_{wave} + L_{wave})]}{c} \right) \exp \left(-\frac{([y - (Y_{wave} + L_{wave}/2)] c)^2}{FWHM / (2\sqrt{2 \ln(2)})} \right). \quad (4.2)$$

The carrier wavelength $\lambda = c_{water}/f$ and the full width of the Gaussian envelope at half of the maximum amplitude $FWHM$ are designed to scale appropriately with respect to ℓ . Here, $f \approx 1.25c_{water}/2\pi\ell$ and $FWHM = 15\ell$. For an alveolar length scale of $\ell = 200\mu\text{m}$, this corresponds to $f = 1.65$ MHz and $FWHM = 3$ mm. $L_{wave} = 45\ell$ is the length of the computational domain, over which the wave is defined to exist and Y_{wave} is y -location of the bottom of the wave at $t = 0$,

which is set to $10a_0$ above the peak of the interface. To consider the dependence of the interface dynamics on pulse amplitude we vary $p_a = 1, 5, 10$, and 15 MPa .

4.3.2 Governing Equations

To simulate the model problem described above we solve equations for conservation of mass, momentum, energy. While it has been long since recognized that tissue exhibits viscoelastic behavior (Bayliss & Robertson, 1939). To simplify things we consider the expected length scale over which viscosity will influence the dynamics, $l_{viscous}$. From dimensional analysis, this scales as $l_{viscous} \sim \sqrt{\nu/(\ell/c)}$. In air at 300 K , $l_{viscous} \sim \mathcal{O}(1\mu\text{m})$ and in water $l_{viscous} \sim \mathcal{O}(0.1\mu\text{m})$. In either case we consider that $l_{viscous} \ll \ell$. Furthermore, we consider the relative importance of elasticity and surface tension

$$\frac{\partial \rho}{\partial t} + \frac{\partial (\rho u)}{\partial x} + \frac{\partial (\rho v)}{\partial y} = 0, \quad (4.3a)$$

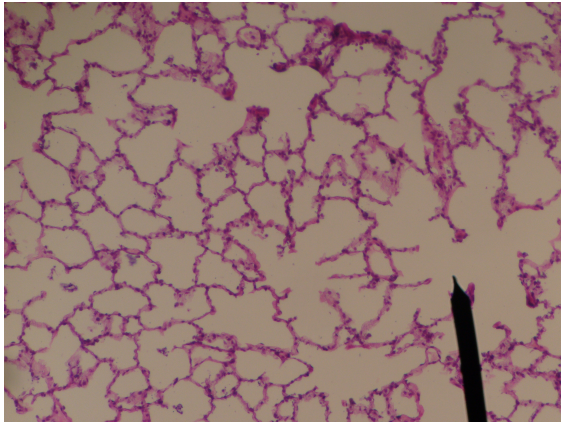
$$\frac{\partial \rho u}{\partial t} + \frac{\partial}{\partial x} (\rho u^2 + p) + \frac{\partial}{\partial y} (\rho u v) = 0, \quad (4.3b)$$

$$\frac{\partial \rho v}{\partial t} + \frac{\partial}{\partial x} (\rho u v) + \frac{\partial}{\partial y} (\rho v^2 + p) = 0, \quad (4.3c)$$

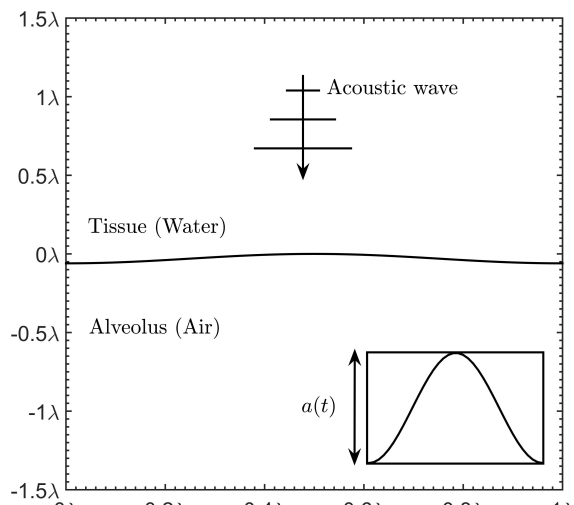
$$\frac{\partial E}{\partial t} + \frac{\partial}{\partial x} [u(E + p)] + \frac{\partial}{\partial y} [v(E + p)] = 0, \quad (4.3d)$$

4.3.3 Computational implementation

The Euler equations (4.3) are solved on a rectangular computational grid using Discontinuous Galerkin Methods in space and a fourth order Runge-Kutta time marching scheme as described in (Patterson and Johnsen, 2016 [submitted]). As previously mentioned the width of the computational domain is 1 mean alveolar diameter, ℓ . The length of the domain is chosen based on two criteria: one - the domain must fully capture the initial acoustic wave and the moving interface throughout the simulation, and two - the domain must be long enough to sufficiently largely eliminate artificial reflections from the boundaries. Thus the computational domain considered for this



(a) (STILL TO BE MODIFIED) A schematic view of an ultrasound wave impinging onto an alveolus. [By Jpogi (Own work) [CC BY-SA 4.0 (<http://creativecommons.org/licenses/by-sa/4.0>)], via Wikimedia Commons]



(b) (STILL TO BE MODIFIED) A schematic view of the model problem.

Figure 4.1: (a) and (b) illustrate the physical and model problems we aim to solve.

problem is described by $0 \leq x \leq 1\ell$ and $-20\ell \leq y \leq 60\ell$. To further help eliminate reflections, grid stretching is implemented at the top and bottom 10ℓ .

- Wave

- ultrasound is focused to a zone that is at least of order λ , and $\lambda \gg \ell$.
- $k_{y-acoustic}/1.25$

-length scales

4.3.3.0.1

To approximately calculate the viscous shear stresses we use the calculated velocity fields.

As the described experiments are in two dimensions, x, y , so the relevant viscous stress tensor can be written as

$$\tau_{ij} = \mu \begin{bmatrix} 0 & \frac{du}{dy} + \frac{dv}{dx} \\ \frac{dv}{dx} + \frac{du}{dy} & 0 \end{bmatrix} \quad (4.4)$$

4.3.3.0.2

4.4 Results and discussion

4.4.0.0.3 synopsis of results

Simulations of interactions between sinusoidal water-air interfaces and diagnostic ultrasound pulses were performed. Approximate viscous and elastic stresses were calculated during the wave-interface interaction and in the time thereafter when the interface continued to evolve. These values were compared to failure stress values from the literature. The dependence on the ultrasound pulse amplitude and alveolar geometry were considered by varying p_a and a_0 respectively.

4.4.1 Qualitative observations of the interface

4.4.1.1 Deformation of the interface

4.4.1.1.1 Figure with interface snapshots to qualitatively illustrate deformation of interface

4.4.1.2 Ultrasound-induced Vorticity generation

4.4.1.2.1 Figure with vorticity snapshots to qualitatively illustrate vorticity

4.4.2 Ultrasound induced stress and strain at the interface

4.4.2.1 Dependence on pulse amplitude, p_a

$p_a = 1, 5, 10,$ and 15 amplitude waves were propagated at interfaces with initial amplitudes of $a_0 = 0.03\ell$ to consider the effect of variable pulse strengths. The Approximate shear stress fields and interface strains with corresponding elastic stresses were calculated for each simulation.



Place
Holder

Figure 4.2: (??) shows snapshots of the interface at **FILL IN** $t = 0, \dots$. The interface continues to deform long after the passage of the wave.

4.4.2.1.1 Viscous shear stresses

4.4.2.1.2 Figure with snapshots of viscous stress field and plot of maximum viscous stress vs t

4.4.2.1.3 Figure with interface strain (left y-axis) and corresponding elastic stress (right y-axis) vs time for varying p_a



Figure 4.3: Vorticity field at $t = (?)$

4.4.2.2.1 Viscous shear stresses

4.4.2.2.2 Figure with snapshots of viscous stress field for $a_0 = 0.03, 0.1, 0.2, 0.3$ and plot of maximum viscous stress vs t for each case

4.4.2.2.3 Figure with interface strain (left y-axis) and corresponding elastic stress (right y-axis) vs time for varying a_0



(a) Viscous stress field at $t = (?)$



(b) Maximum viscous shear stress in the field at
 $t = (?)$

Figure 4.4: (a) and (b) show the shear stress field at $t = (?)$ and the maximum shear stress value within the field as a function of time.



Place
Holder

Figure 4.5: Interface strain and elastic stress field as a function of time



(a) Viscous stress field at $t = (?)$



(b) Maximum viscous shear stress in the field at
 $t = (?)$

Figure 4.6: (a) and (b) show the shear stress field at $t = (?)$ and the maximum shear stress value within the field as a function of time.



Place
Holder

Figure 4.7: Interface strain and elastic stress field as a function of time

CHAPTER 5

Conclusions

Part II

Underwater Acoustic Uncertainty

CHAPTER 6

Past work: Efficient estimation of the probability density function of transmission loss in uncertain ocean environments via area statistics

6.1 Abstract

Calculations of acoustic Transmission Loss (TL) in the ocean are useful in naval and ocean monitoring applications. These TL calculations are often uncertain because they are based on uncertain environmental parameters, but standard methods for determining TL uncertainty are computationally expensive. This paper describes how TL statistics in a range-depth area surrounding the point of interest within a single TL-field calculation can be efficiently used to estimate the Probability Distribution Function (PDF) of TL that results from ocean environment uncertainty. Such area-statistics estimated PDFs of TL are compared to PDFs of TL obtained from 1000-sample Monte-Carlo calculations at source frequencies of 100, 200 and 300 Hz and source depths of 91, 137, and 183 m in four different uncertain ocean environments at test location depths from 20 m to 5 km and source-receiver ranges from a few km to more than 60 km. These comparisons show that the estimated PDFs of TL are engineering-level accurate in 93% of tests in ocean environments with consistent bottom reflection, and can be produced with $O(10^{-6})$ the computational effort required for the Monte-Carlo calculations. In deep refracting environments, area statistics was engineering-level in 78% of test cases after algorithm adjustments.

6.2 Introduction

Remote sensing in the ocean is primarily managed through the broadcast and/or reception of acoustic waves. Computational acoustic field models are commonly used to assess the extent of radiated sound fields, and to extract information from recorded signals via signal processing routines. Unfortunately, the ocean environment parameters necessary for fully exploiting the capabilities of modern acoustic field models are seldom (if ever) known with sufficient precision to prevent uncertainty in ocean parameters from influencing the predicted acoustic fields. Yet, understanding and quantifying the uncertainty associated with a given field calculation is important for determining its utility.

In underwater acoustics, the uncertainty in acoustic field predictions arises from limited knowledge of the physical and geometric properties of the ocean environment of interest. Consequently, acoustic field predictions are typically made using imperfect estimates of environmental parameters, and, as a result, the predicted fields themselves are also uncertain. For a harmonic acoustic field produced by a point source, the most fundamental attribute is the field's amplitude, and it is commonly reported as transmission loss (TL), a field quantity that has been part of sonar engineering for many decades (Urick, 1962). Uncertainty in TL predictions has received increased attention in recent years due to its utility in practical naval applications (Abbot & Dyer, 2002; Pace & Jensen, 2002) and ocean measurement system design (Munk, 1994). Unfortunately, there is no known general relationship between environmental uncertainty and TL field uncertainty, and the most common techniques for calculating TL uncertainty, Monte Carlo and direct sampling methods, are too computationally expensive to be practical for real time applications. The purpose of this paper is to introduce and describe an approximation technique, area statistics, as a computationally efficient alternative to Monte Carlo and direct sampling methods, or other means for producing the probability density function of TL at a point of interest within an uncertain ocean environment.

The topic of acoustic uncertainty in ocean environments has seen considerable interest in the

last decade or so (Livingston *et al.*, 2006). The physical uncertainty of an ocean environment has been shown to have considerable impact on naval applications ranging from sonar performance prediction to tactical decision aids and threat assessment. Accordingly, there has been much work within the field of underwater acoustics toward two goals: (1) understanding and quantifying environmental and acoustic field uncertainties, and (2) determining how these uncertainties affect relevant applications (Abbot & Dyer, 2002; Emerson *et al.*, 2014; Sha & Nolte, 2005; Stone & Osborn, 2004). The technique described here primarily addresses the first goal through computationally efficient predictions of TL field uncertainty based on typical ocean environment uncertainties.

There have been multiple studies aimed at accurately describing environmental uncertainties. This is a challenging task given the complexity and variability of the ocean water column and seabed properties, especially in shallow waters (Livingston *et al.*, 2006). Uncertainties associated with archived bathymetry data sets obtained without the use of modern multi-beam technology have been reported (Calder, 2006), and historical data have been used to describe seasonal sound-speed uncertainties on the continental shelf and slope in the Middle Atlantic Bight (Linder *et al.*, 2006).

The task of predicting acoustic TL field uncertainties that arise as a result of the uncertain environment is the focus of this paper. The starting point is a single baseline TL-field calculation that provides TL as function of range and depth within the ocean along a chosen azimuthal direction. For this baseline calculation, all uncertain environmental parameters are set to their most probable values. The Probability Density Function (PDF) of TL is used here to quantify the uncertainty of baseline TL values since it contains all the relevant TL statistics for ocean applications (Gerstoft *et al.*, 2006). The mean and standard deviation of TL, which may be reflective of the macro- and micro-states of the ocean, respectively (Abbot *et al.*, 2006), are readily calculated from the PDF of TL. The techniques currently available for predicting the PDF of TL require differing levels of computational effort. These are described in the following paragraphs from highest to lowest computational cost, as assessed by the number of additional TL field calculations beyond the baseline calculation necessary to implement the technique.

Monte Carlo and direct sampling methods are well-accepted techniques for obtaining PDFs of TL, but their computational effort increases exponentially as the number (N) of uncertain environmental parameters increases. For both techniques, a potentially large set of TL calculations is undertaken that sample the N -dimensional space of uncertain environmental parameters in a random (Monte Carlo) or structured (direct sampling) manner. The PDF of TL at any location in physical space is then constructed from the computed TL values found at that location in each of the many field TL calculations. Monte Carlo calculations have been used to obtain the probability distribution of TL subject to geoacoustic inversion uncertainty (Gerstoft *et al.*, 2006), and to explore acoustic sensitivity to environmental parameters and assess the utility of a stochastic description of environmental variables (Heaney & Cox, 2006). More recently, Monte Carlo and direct sampling calculations have been used to generate reference PDFs of acoustic field amplitude to assess the accuracy of approximate PDF construction techniques (James & Dowling, 2008, 2011). Monte Carlo calculations based on 1000 TL field calculations are used for this purpose in the work reported here.

The mathematically rich technique of polynomial chaos expansions (PCE) has also been used to assess acoustic uncertainty (Finette, 2005, 2006, 2009). Here the uncertain acoustic field is represented as a series of Q basis functions with each function having its own range-, depth-, and frequency-dependent coefficient. The coefficients are determined from the solution of a set of Q coupled partial differential equations. The technique produces converged uncertainty assessments as Q increases, with Q being a proxy for the number field calculations when there is a single uncertain environmental parameter ($N = 1$). However, when there are more uncertain parameters ($N \geq 2$), a different PCE solution technique is needed and the approximate correspondence between Q and the number of field calculations is lost. For comparison, the area statistics technique described herein is simpler to implement than PCE and it does not require the solution of any additional partial differential equations beyond the baseline TL field calculation.

There are also approximate methods for predicting acoustic uncertainty that do not involve the computational expense of Monte Carlo simulation or mathematical complexity of PCE. A tech-

nique for estimating TL confidence bounds for environments in which acoustic propagation can be described by a sum of propagating modes has been previously described (Zingarelli, 2008). The technique can be applied when there are multiple uncertain parameters and it is computationally efficient, as it only requires the baseline field calculation. However, it inherently relies on range, depth, or frequency averaging, and does not provide the full PDF of TL. Another approximate method for predicting the PDF of acoustic field amplitude for multiple uncertain environmental parameters is based on determining spatial shifts between acoustic field calculations completed with a difference in one uncertain parameter (James & Dowling, 2008). However, this field-shifting technique requires one additional field calculation for each uncertain parameter.

The area statistics technique described here provides estimates of the PDF of TL, and only requires the baseline TL field calculation. It is simple and fast enough for implementation in real-time sonar applications, and can be used in any environment for which TL field calculations can be completed. As implemented here, it incorporates $N = 5$ uncertain parameters, but the number and selection of these can be altered. When compared to Monte Carlo results based on 1000 TL field calculations, it reaches engineering level accuracy in 93% of test cases in downward-refracting acoustic environments that support consistent bottom reflection. The remainder of this paper is divided into three sections. The next section describes the four uncertain ocean environments used in this study, the area statistics technique, and the procedures followed for generating the Monte Carlo results. The third section presents quantitative comparisons between area statistics and Monte Carlo results in the four ocean environments at depths from 20 m to 5 km, and ranges from a few km to more than 60 km. The final section summarizes this effort and states the conclusions drawn from it.

6.3 Methods

This section describes the main components of this investigation: the uncertain ocean environments and their characterization, the algorithm steps followed for the area statistics technique, the

implementation details for the Monte Carlo calculations, and the quantitative means for assessing the accuracy of the PDFs of TL produced from area statistics. Sample results are provided to illustrate each component.

Four ocean environments with uncertain bathymetry, sound speed profile (SSP), and seabed properties were considered in this study. The environments, labeled 1 through 4 and ordered according to their maximum depth from shallowest to deepest, are shown in cross section in Figure 1. For environments 1 and 3, bathymetric data were obtained from National Oceanographic and Atmospheric Administrations multibeam bathymetric survey database (Multibeam collections for KM0504, EW9509), and are taken from the challenger plateau west of New Zealand, in the South China Sea, and off the coast of Taiwan. For environments 2 and 4, bathymetric data were obtained from the US Office of Naval Researchs (Vuln-TDA-STTR_10-25-14_samples), and are taken from the North Pacific, near the Hawaiian Islands.

Five uncertain parameters were considered within each environment: bathymetry offset , sound speed increment multiplier , seabed density , seabed sound speed , and seabed attenuation . These are labeled and depicted in Figure 2. Detailed specifications of these were needed to complete the Monte Carlo calculations described below. The bathymetry offset represented ocean depth uncertainty and was a random range-independent distance that was added uniformly to the range-dependent bathymetric survey depth of the environment. The seabed was treated as a single layer with random range independent properties (ρ_b , c_b , and α_b).

The sound speed increment multiplier γ requires a little more description. For the environments where range- and depth-dependent SSP information was provided (2 and 4), the range-averaged, but still depth-dependent, mean $\langle c(z) \rangle$ and standard deviation $\langle \sigma_c(z) \rangle$ of the sound speed were calculated. This range-averaged mean SSP $\langle c(z) \rangle$ was then used as the baseline SSP for TL calculations in each sample environment. Uncertainty in the SSP was introduced by adding $\gamma \langle \sigma_c(z) \rangle$ to $\langle c(z) \rangle$ for each individual Monte Carlo calculation, with γ varying randomly between calculations. Because only $\langle c(z) \rangle$ was known for environments 1 and 3, $\langle \sigma_c(z) \rangle$ calculated for environment 2 was used to incorporate SSP uncertainty in these environments.

All 5 uncertain parameters were assumed to have Gaussian-like distributions, however the extremes of the distributions were truncated as described below and the distribution values were then renormalized. The most-probable value and Gaussian standard deviation of each uncertain parameter is provided in Table 1. Samples were drawn randomly from these distributions for the Monte Carlo calculations. The most-probable values, standard deviations, and parametric ranges in Table 1 were intended to mimic the actual uncertainties associated with readily available information about ocean environmental parameters. The bathymetry offset values were intended to mimic tidal fluctuations. The seabed values were developed from the mean and standard deviation of the tabulated bottom layer properties for clay, silt, sand, gravel, moraine, chalk, and limestone found in [Jensen *et al.* \(2011\)](#). The distributions of , , , and were truncated at . And, the distribution of was truncated by the properties of clay on the low end and limestone on the high end to ensure that the value of remained physically realistic. The sound speed increment multiplier values were based on appropriately incorporating tabulated variations in ocean sound speed. Note that for each environment, the situation where all of the uncertain parameters take on their most likely values are referred to as the baseline case.

The area statistics technique is based on the assumption that the uncertainty in the TL value at any range-depth (r, z) location in an uncertain ocean sound channel can be obtained by considering the variations in TL found near that location in the baseline TL calculation. The procedure for area statistics merely requires the baseline TL calculation at the frequency of the sound source, the (r, z) location of interest within the calculated TL field, and an algorithm or recipe for choosing and combining TL values near the location of interest to form an estimate of the PDF of TL. Given the simple assumption upon which the area statistics technique is based, the primary development effort involved empirically determining how to sample the TL field near the point of interest to achieve acceptable results for the five uncertain environmental parameters. Thus, some of the details of the algorithm described here would likely need revision if additional (or fewer) environmental parameters were uncertain.

For the area statistics technique, the baseline TL field calculation may come from any acoustic

propagation model. For this investigation, computed TL fields were obtained from the Range-dependent Acoustic Model (RAM)(Collins, 1994). In each case, TL field calculations were performed along an outward radial from a unity-strength harmonic monopole sound source with frequency $f_s = 100$ Hz, 200 Hz, or 300 Hz, and placed 91 m, 137 m, or 183 m, below the ocean surface. The source frequency and a nominal sound speed $c_s = 1500$ m/s were used to calculate the nominal wavelength, λ_s .

Using the baseline TL-field calculation, a simple algorithm or recipe with three steps was developed to produce area statistics results for any range-depth (r, z) location of interest. First, all the TL values within a range-depth rectangle centered on (r, z) were collected and weighted uniformly. Second, these TL values were sorted into a histogram. And third, this histogram was normalized to form an estimate of the PDF of TL. For this study, the sample rectangle's range and depth dimensions were $40\lambda_s$ and $13\lambda_s$, respectively, and a nominal histogram bin width of 1 dB was used. Here, the sample rectangle's dimensions were chosen to produce suitable results for the uncertainties defined in Table 1. Different sample rectangle dimensions, different TL sample weighting, and other adjustments to the area statistics algorithm are likely to be necessary for a different set of uncertainties.

Figure 3 illustrates this procedure at the range-depth location of (5720 km, 240 m) in environment 2 for a 200 Hz sound source. In Figure 3a), the TL sample area is indicated by the black box near the center of the TL field plot. The TL sample area is shown in an expanded view in Figure 3b) and is comprised of 720 individual TL samples. Two-dimensional linear interpolation was used to increase the number of range columns in the computational grid such that the final normalized histogram is comprised of 1715 TL samples. The area-statistics-estimated PDF of TL developed from the TL samples in Figure 3b) is shown in Figure 3c). For successful area statistics results, at least 400 TL samples are needed, and these can be obtained by two-dimensional linear interpolation if the baseline TL calculation was performed with coarse resolution and does not provide enough TL values within the sample rectangle. In addition, TL samples were not collected from any portion of the sample rectangle lying above the ocean surface or below the ocean floor.

When necessary, the bathymetry was linearly interpolated to calculate the water column depth at the range associated with each column of the computational grid.

To assess the accuracy of the estimated PDFs of TL, they were compared with Monte Carlo-generated PDFs of TL that were created from the computed TL values at the location of interest. Here, 1000 separate TL field calculations were completed used, each with values for the uncertain environmental parameters, drawn randomly from the probability distributions described in Table 1. These 1000 TL samples were sorted into a histogram with 1 dB nominal width bins, and the histogram was normalized to create a PDF of TL. Here the number of Monte-Carlo samples (1000) was high enough so that the Monte-Carlo generated PDFs of TL were comparably converged when compared to their counterpart area-statistics-estimated PDFs of TL (typically 400 to 3000 samples). A sensitivity analysis for a 200 Hz source in each of the four environments that involved increasing the number of Monte-Carlo samples to 2000 did not produce significant differences. Specifically, when compared to the 1000 sample results, the number of test points at which engineering accuracy was achieved changed by 1% or less.

Quantitative comparisons of the area-statistics estimated PDFs of TL (subscript 'AS') and the Monte-Carlo PDFs of TL (subscript 'MC') were made with the L_1 error-norm:

$$L_1 = \int_{-\infty}^{+\infty} |PDF_{MC}(TL) - PDF_{AS}(TL)|d(TL), \quad (6.1)$$

the integrated absolute value of the difference between the two PDFs, or, more intuitively, the non-overlapping area of the two PDFs. For PDF comparisons, is a convenient metric of accuracy because it is a single quantity that inherently accounts for differences in the mean, width, and shape of two PDFs. The error-norm is a dimensionless quantity that is bounded between 0 and 2, with corresponding to a perfect match between the two PDFs and corresponding to total mismatch (no overlap) of the two of the PDFs. In this study, 0.50 was chosen as the criterion for which an area-statistics-generated PDF was deemed engineering-level accurate. This criterion corresponds to a difference of 2 dB mean error (a measure of PDF location) and 2 dB standard deviation error

(a measure of PDF width) in 84% and 85% of test cases, respectively.

The L_1 error-norm is illustrated in Figure 4 for engineering-level-accurate (Figure 4a) and -inaccurate (Figure 4b) estimates for the PDF of TL. In both panels, the jagged marked area is the error. The result shown in Figure 4a) comes from the range-depth location (5720 m, 288 m) in environment 2, and the mean and standard deviation of the area statistics PDF (solid curve) are 1.23 dB and 1.02 dB smaller, respectively, than those of the Monte-Carlo PDF (dashed curve). The result shown in Figure 4b) comes from the range-depth location (1140 m, 384 m) in environment 2, and the mean and standard deviation of the area statistics PDF (solid curve) are 0.86 dB and 1.92 dB smaller, respectively, than those of the Monte-Carlo PDF (dashed curve).

6.4 Results and comparisons

For an overall accuracy assessment of the area statistics method, the error from (1) was computed on a coarse rectangular grid in each of the four uncertain ocean environments. The results are shown in Figure 5 as a grid of test locations overlaid on the baseline TL field for a 200 Hz source in each environment. The number and position of test locations were chosen based on the physical geometry and computational grid spacing in each environment without consideration for the results at the test locations. The number of test locations was increased in environment 4 due its larger physical size. Test points below the ocean floor were not considered. In each panel of Fig. 5, a white circle indicates a test location where the area-statistics estimated PDF of TL was found to be engineering-level accurate ($\zeta = 0.50$), while a black triangle indicates a test location where engineering-level accuracy of the area-statistics estimated PDF of TL was not achieved ($\zeta < 0.50$).

In the three shallower environments, area statistics produced PDFs of TL with errors less than or equal to 0.50 at 88, 95, and 85% or more of test locations for 91-m, 137-m, and 183-m deep sources at frequencies of 100, 200, and 300 Hz respectively. In the deepest environment where refraction of sound plays a larger role, area statistics was less successful. A quantitative summary of these results is provided in Table 2 which also includes additional results for environment 4

when the area-statistics algorithm described above is adjusted (marked with a).

To improve the area statistics results for deeper refractive environments, a closer look was taken at the TL fields and PDFs of TL calculated for environment 4. The most common failure in environment 4 typically occurred at test locations below the critical depth at which the sound speed equals the sound speed at the ocean surface (herein referred to as deep water test locations). For this failure, the shapes of the area-statistics and Monte-Carlo generated PDFs of TL were similar but the mean TL values were sufficiently different such that the errors were high. Furthermore, in these failures of area statistics, the baseline TL value at the center of the sample rectangle was noticeably different from the mean and median TL values of the sample area, indicating a highly non-uniform distribution of TL values around the sample rectangle center point. To partially correct the area statistics PDFs of TL for failures of this type, half the difference between the baseline and median TL values from the AS sample area was added to every TL value in the sample area to appropriately shift the area-statistics PDF of TL. This algorithm adjustment improved the percentage of engineering accurate tests locations in environment 4 from 64% to 73% for a 137m deep, 200 Hz source. And, this algorithm adjustment did not affect the success percentages of area statistics in environments 1, 2, or 3 at any of the frequencies considered here (100, 200, and 300 Hz).

The computational effort associated with area statistics was also compared to that associated with the Monte Carlo calculations using the MATLAB profiler. As might be expected, given its simple formulation, area statistics is significantly more efficient than Monte Carlo calculations. With the baseline TL calculation as a starting point for both approaches, area statistics does not require another TL field calculation while the Monte-Carlo approach as implemented here involves 1000 more. Thus, the difference in computational burden is substantial. For a single location, the Monte-Carlo calculations (using 10 Pad terms in RAM's PE solver) required 4.6 million times more computational effort than area statistics on average. For 100 field locations in a single range-depth plane of an uncertain ocean, the Monte-Carlo calculations required an average of 46 thousand times more computational effort than area statistics. Additionally, once the baseline TL calculation

is complete, area statistics can provide PDFs of TL in milliseconds of real time, making it practical for real-time applications of TL uncertainty.

6.5 Conclusions

This paper describes the area statistics technique for efficiently estimating transmission loss (TL) uncertainty in underwater acoustics. The technique is based on the idea that the TL variation found near the point interest in real space is similar to that found at the location of interest when environmental parameters are varied. The technique is simple and can be used to produce approximate PDFs of TL in uncertain ocean sound channels from a single (baseline) TL field calculation completed using the most probable value for each uncertain parameter. To implement the technique, TL values near a location of interest in the baseline TL field are collected and sorted into a histogram that is normalized to obtain an approximate PDF of TL at the location of interest. To determine the technique's accuracy, PDFs of TL created using area statistics were compared to PDFs generated using 1000-sample Monte Carlo calculations in four different ocean environments at three acoustic frequencies (100, 200, and 300 Hz) for three different source depths (91m, 137m, 183m). The area-statistics PDFs of TL achieved engineering-level accuracy (≤ 0.5) in 93% of test cases in the three shallower environments with consistent bottom reflection. In the environments where refraction was more important, area statistics was less successful; engineering level accuracy was only achieved in 56% of test cases, initially. However, this success percentage was improved to 65% by gently modifying the area statistics algorithm, and this modification did not affect the results in the shallower ocean environments.

The effort reported here supports the following four conclusions. (1) The area statistics technique is a viable alternative, or worthy complement, to Monte-Carlo calculations or other more computationally intensive techniques for estimating the uncertainty of TL field calculations in uncertain ocean environments with consistent downward-refraction and bottom reflection. In each of the three environments of this investigation meeting this bottom reflection criterion, the technique

produced engineering-level accuracy at 85% or more of the test locations. (2) The area statistics algorithm is simple enough that it can be modified to improve the technique's overall performance. One simple algorithm adjustment improved the engineering accuracy success rate of area statistics in the deepest environment considered in this study by approximately 10% at all three frequencies. (3) The area statistics technique is so inexpensive computationally that it should be implemented even when a more reliable but more computationally demanding approach is the primary means for TL uncertainty estimation. As part of this investigation, the area statistics approach was found to be millions of times faster than Monte-Carlo calculations. Thus, the computational penalty for implementing both, if the latter is preferred, is vanishingly small. Moreover, the technique is computationally inexpensive enough for use in real time applications. (4) The sample rectangle size, TL sample weighting, and other implementation details of the area statistics algorithm described here are likely to need adjustment if the ocean sound channel uncertainties of interest differ from those given in Table 1. The area statistics technique is ad-hoc and the implementation parameters in its current formulation were tuned to achieve a high percentage of engineering-accurate predictions for ocean sound channels with the uncertainties specified in Table 1. However, the uncertainties specified in Table 1 are generic and may serve as a useful starting point for many uncertain ocean sound channels. Thus, the area statistics formulation provided here may be broadly applicable.

Appendices

Appendix A

Random Pieces

Circulation Model

We now seek to develop a model to predict the circulation deposited during the interaction between a linear compression or expansion wave and the water-air interface. To develop the model we assume that the interface is approximately static during this interaction and maintains its initial sinusoidal shape. Based on

Hence we write,

$$\Gamma = \int_{0^+}^{\Delta t_a} \int_{-\infty}^{+\infty} \int_{1/2}^1 \frac{\nabla \rho \times \nabla p}{\rho^2} dx dy dt$$

A.1 Justifying Calculations

A.1.1 ka -calculations

Length Scales: $L_{alveolus} = 100\mu \text{ m}$

$$f_{us} = 1.5 \text{ MHz}$$

$$c_{water} = 1500 \text{ m/s}$$

$$\lambda_{acoustic} = \frac{c_{water}}{f_{us}} = 1 \text{ mm}$$

$$k = \frac{2\pi}{\lambda_{acoustic}} = 2000\pi \text{ m}^{-1}$$

$$a = L_{alveolus}$$

$$(ka)_{f=1.5\text{MHz}} = \frac{\pi}{5} \quad (ka)_{f=4.5\text{MHz}} = \frac{3\pi}{5}$$

Dimensional Numbers:

- Let $\lambda_{alveolus} = 100\mu \text{ m}$, $u_0 = c_{air} = 343 \text{ m}$, $v_0 = \langle a(t) \rangle \approx 0.65 \text{ m/s}$, $u_{intf}(t = 20) = 12.8 \text{ m/s}$, $G = 1 \text{ kPa}$
- $\lambda_{alveolus} = 100\mu \text{ m}$, $u_0 = c_{air} = 343 \text{ m}$, $v_0 = \langle a(t) \rangle \approx 0.65 \text{ m/s}$
- $t = 1 \rightarrow t_{dim} = 0.292\mu \text{ s}$
- $\sigma_{Alv} = 0.009 - 0.02 \text{ N/m}$ Schürch *et al.* (1976)

Model justifications: **Argument against viscosity - viscous length scales**

$$\nu_w = 0.7 \mu\text{m}^2/\text{s}, \quad \nu_a = 16.6\mu\text{m}^2/\text{s}, \quad f_c = \mathcal{O}(10^6)\text{Hz}$$

$$\sqrt{\nu_{air}/f_c} = 4\mu \text{ m} = \mathcal{O}(10^{-6}) \ll L_{alveolus} = \mathcal{O}(10^{-4})$$

$$\sqrt{\nu_{air,ND} t} \approx 0.5 < a(t) - a_0 \approx 4 \text{ at } t = 1000$$

Therefore the scale of the viscous effect is smaller than the scale of the problem we are looking at, but may be important at late times.

Argument against gravity:

- $Fr = \frac{u_0}{\sqrt{g_0 \lambda}} \approx 11000$

- $Fr = \frac{v_0}{\sqrt{g_0 \lambda}} \approx 21$

$$\nabla \times \mathbf{g} = 0$$

Argument against elasticity:

- $Ca = \frac{\rho u_{intf}^2}{G_{Alv}} = 163$

Argument against surface tension:

- $We = \frac{\rho_w u_{intf}^2}{\sigma_{Alv}} \approx 21 - 47 \times 10^3$

Numerical treatment of the initial interface

Theoretical vs simulated reflection coefficients

- Put contour plots of pressure here at $t = 1, 10, 20, 50, 100$ (or whatever)
- Put plots of pressure (p vs y center-line) after reflection from boundary here.
- Calculate theoretical and experimental pressure reflection coefficients
- Calculation $R = p_R/p_I = (-p_{reflected} + p_{atm})/(p_a - p_{atm}) = ((69.15 + 101325/p_{scale})/(71.42 - 0.714285714)) \approx 0.988$

To ensure that the numerical implementation of the interface is sufficiently sharp as to reflect the dynamics of a discontinuous interface, the simulated acoustic reflection coefficient T_S was calculated for the case of the 10 MPa trapezoidal wave for varying thickness parameter delta δ and compared to the theoretical acoustic reflection coefficient T , where

$$T = \frac{2(\rho c)_{air}}{(\rho c)_{air} + (\rho c)_{water}}$$

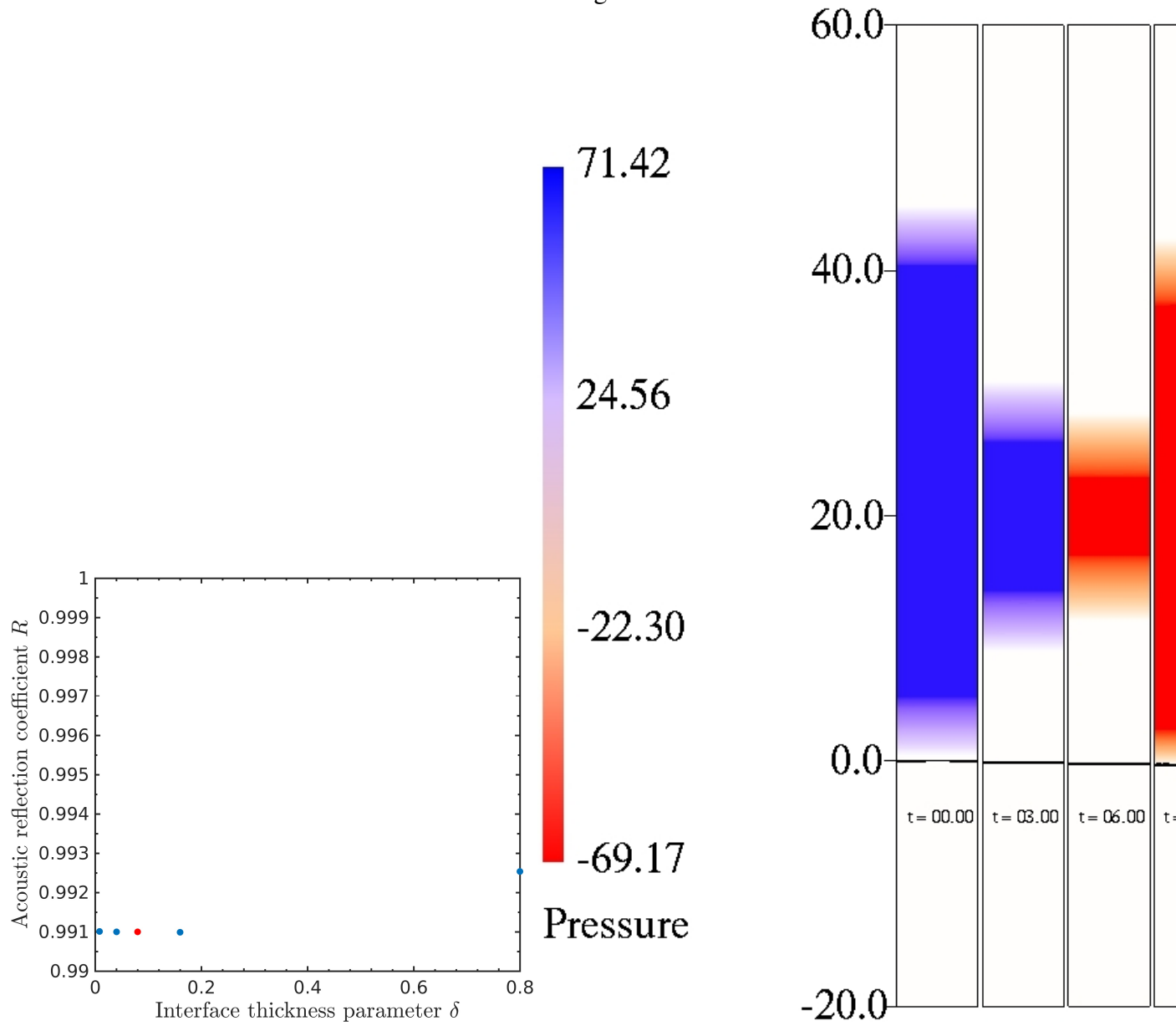
The prescribed interface thickness parameter (typically $\delta = 0.08\lambda$) was used to determine the initial volume fraction and density condition where the a distance parameter from the interface is defined as

$$d = \frac{\delta + y(x)_{interface} - y}{2\delta}.$$

and the initial Volume fraction is written as

$$y_0 = \begin{cases} 1, \\ \exp(\log(10^{-16}) |d|^8), \\ 0, \end{cases}$$

such that d is normalized within the mixed air-water region.



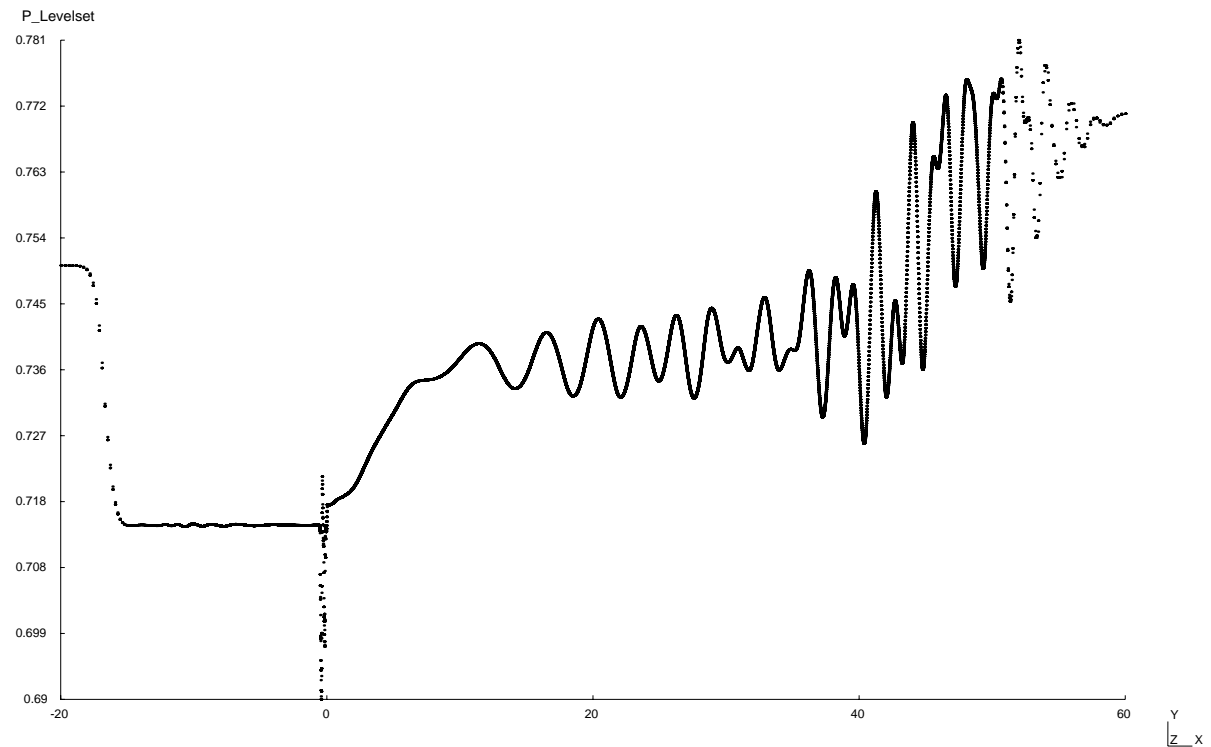


Figure A.1: Center-line pressure at $t=25$. At maximum, 0.1% of the wave is reflected back into the domain.

Mechanical Index

13;5u

$$MI = \frac{P_{PRPA}}{\sqrt{f_c}}$$

- The mechanical index is a metric designed to measure cavitation damage.
- It was designed for cavitation in water.
- FDA mandates that MI must stay below 1.9.

A.2 Convergence

- Put plots of vorticity and $a(t)$ for 50, 100, and 200 pts per lambda to demonstrate convergence

Previous studies of the Richtmyer-Meshkov Instability (RMI) have utilized theory, computation, and experiments to describe the behavior of the interface after the wave has passed. Richtmyer (1960) performed the linear stability perturbation analysis developed by Taylor (1950) for the case of an impulsive acceleration to create a model for the initial growth of the interface perturbation. Meshkov (1972) experimentally confirmed Richtmyer's qualitative predictions, hence the name of the instability. Meyer (1972) performed numerical simulations of the RMI and found good agreement with Richtmyer for the case of a shock impinging upon a light-heavy interface. Fraley (1986) used Laplace transforms in order to find the first analytical solution for the asymptotic growth rate for a shocked interface between perfect gases. To describe the late time, nonlinear growth of the perturbation, Zhang & Sohn (1997) used single mode perturbation, keeping many high order terms, to describe the velocity of the bubble and spike regions of the fluid. Sadot *et al.* (1998) combined the linear, impulsive solution with potential flow models of the asymptotic behavior of the bubble and spike to develop a model for the perturbation growth that is in good agreement with shock tube experiments for shocks with Mach numbers $\text{Ma}=1.3, 3.5$. Vortex theory has also been used to describe the behavior of the interface. Jacobs & Sheeley (1996) horizontally oscillated a container with two vertically stratified liquids to obtain standing waves and then bounced the container off of a coil spring to study the incompressible RMI. The late time evolution of the interface is modeled using a row of line vortices to obtain qualitatively similar results to those experimentally observed, however the late-time growth rate is underestimated. Samtaney & Zabusky (1994) used shock polar analysis to find the circulation deposited by a shock on planar and non-planar interfaces. Their results are validated using an Euler code and found to be within 10% of the computed value for $1.0 < \text{Ma} \leq 1.32$ for all $\rho_2/\rho_1 > 1$, and $5.8 \leq \rho_2/\rho_1 \leq 32.6$ for all Ma.

vorticity study objective

The objective of the present study is to provide a detailed explanation of the physics governing a perturbed water-air interface driven by a trapezoidal acoustic wave. This separate from previous research, which has largely looked at constantly-accelerated and shock-accelerated interfaces. Consequently, there are physically novel aspects of the present study. First, acoustic waves, which are typically thought of as small amplitude are shown to drive perturbation growth at the interface via baroclinic vorticity. Shock waves are, by definition, discontinuous and hence their propagation is a nonlinear process. In contrast, the propagation of acoustic waves in a homogeneous medium is a linear process. In the present study nonlinearity occurs as a result of the strong density discontinuity at the liquid-gas interface. Second, the acoustic wave has a finite duration. Hence the vorticity is deposited throughout a finite interaction time, unlike in the case of the RMI in which it is created by an instantaneous acceleration or the **RTI!** (**RTI!**) in which vorticity results from constant acceleration. Unlike shocks, which occur over a few molecular mean free paths and interact nearly instantaneously, acoustic waves occupy a finite space. Hence their interaction with interfaces occurs over a finite time. And third, interface deformation that occurs during the acoustic wave-interface interaction cannot be neglected. Transient interactions between deforming interfaces and multiple shocks are known to be capable of affecting the long term growth of the interface. [Henry de Frahan *et al.* \(2015a\)](#) demonstrated that interface growth could be controlled through transient wave-interface interactions by simulating shock passage through layered media, as a result of subsequent interactions between the interfaces and reflected and transmitted shocks and rarefactions. This work demonstrates that interface deformations that occur during the interaction with the acoustic wave can have a strong effect on the final growth of the interface.

A.2.0.1 Vorticity distribution

To better understand the distribution of vorticity generation within the gas-liquid mixture region of the interface we perform an order of magnitude analysis to compare the baroclinic vorticity from equation (3.8) in pure water vs air. As this can already be evaluated in water from what we have provided up to this point, we will focus on evaluation of the order of baroclinic vorticity generation in air.

Throughout this analysis we will denote the properties of the incoming wave and water with a subscript $-$, and the transmitted wave and air with a subscript $+$. For water, we will use the values for $\Delta\rho_I, \Delta L_I, \Delta\rho_a, \Delta L_a$ and θ previously defined in the section ??, based on our initial condition. Our treatment of the density gradient across the interface will remain unchanged for evaluation in air such that $\Delta\rho_I^- = \Delta\rho_I^+$ and $\Delta L_I^- = \Delta L_I^+$. To evaluate the remaining terms in air we will borrow techniques from linear acoustics. To find the pressure rise in the transmitted wave Δp_a^+ , we recognize that $a_0/\ell \ll 1$ and treat the incoming wave as a plane wave impinging normally on a flat material interface such that $\Delta p_a^+ = \mathbf{T} \Delta p_a^-$, where \mathbf{T} is the acoustic transmission coefficient, $\mathbf{T} = 2\rho^+ c^+ / (\rho^+ c^+ + \rho^- c^-)$ (Kinsler *et al.*, 1982). For our water-air interface $\mathbf{T} \approx 4.97 \times 10^{-4}$. Because of the strong impedance mismatch between fluids, the acoustic wave is almost entirely reflected, decreasing the pressure gradient in the air. Because of the drop in sound speed across the interface, the transmitted wave is compressed into a smaller physical area (i.e., the wavelength decreases) relative to the incoming wave, such that $\Delta L_a^+ = \Delta L_a^- (c^+ / c^-)$. This effect increases the pressure gradient in the air. To evaluate θ^+ , we utilize Snell's law which states that $c^- \sin \theta^- = c^+ \sin \theta^+$. Because $a_0/\ell \ll 1$ it is also true that $\theta^- \ll 1$, thus we use the small angle approximation of sin to find that $\theta^+ \approx \theta^- (c^+ / c^-)$. This refraction effect decreases the misalignment between the pressure and density gradients for the transmitted wave relative to the incoming wave. Quantitatively it also approximately cancels the increase in vorticity deposition that arises as a result of the increased pressure gradient created by the decrease in the length of the transmitted wave.

To get an idea of where within the mixed gas-liquid region at the interface the vorticity will be

generated, we consider equation (3.8) in air and water and write the ratio to find

$$\begin{aligned} \frac{\left\| \frac{\nabla \rho \times \nabla p}{\rho^2} \right\|_{air}}{\left\| \frac{\nabla \rho \times \nabla p}{\rho^2} \right\|_{water}} &= \mathcal{O} \left(\frac{\left[\frac{|\Delta \rho_I^+|}{|\Delta L_I^+|} \frac{|\Delta p_a^+|}{|\Delta L_a^+|} \frac{1}{|\rho^+|^2} |\theta^+| \right]}{\left[\frac{|\Delta \rho_I^+|}{|\Delta L_I^+|} \frac{(|\Delta p_a^+| / |\mathbf{T}|)}{|\Delta L_a^+| (|c^+| / |c^-|)} \frac{1}{|\rho^-|^2} (|c^+| / |c^-|) |\theta^+| \right]} \right), \\ &= \mathcal{O} \left(|\mathbf{T}| \left(\frac{|\rho^-|}{|\rho^+|} \right)^2 \right). \end{aligned} \quad (\text{A.1})$$

For our water-air interface, we evaluate equation (A.1) to find that the ratio of baroclinic vorticity generation in air to that in water would be of order $\mathcal{O}(10^2)$. While this analysis considers vorticity generation in pure air and water, as opposed to the mixed fluid region that is exactly relevant to this work, we make two observations based on this result. First, this result analysis is for an extreme case in which all of the vortical energy relevant to this problem, is able to be concentrated in pure air and water, and thus this result acts as an upper bound on the change in vorticity deposition we expect as the wave move from water across the interface into air. Additionally, this result suggests that for the mixed water-air region, where the strongest density gradient exists, vorticity generation is likely to occur in gas dominated fluid regions with a higher volume fraction of air than water.

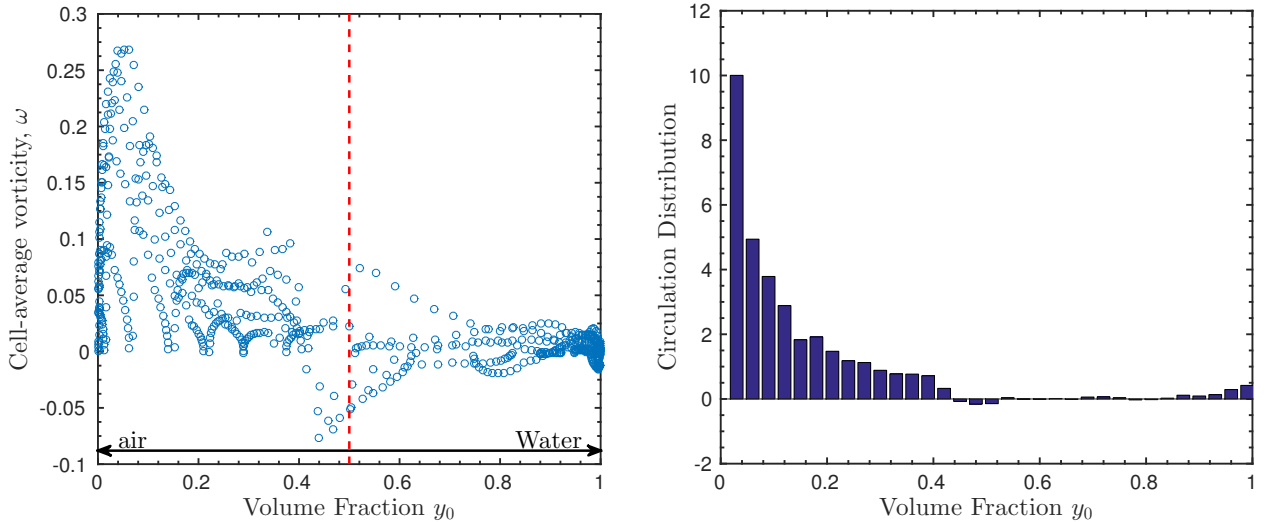


Figure A.2: For cells with non-negligible vorticity, a scatter plot of the mean vorticity in each cell is plotted as a function of volume fraction water (Left).

From the vorticity contours at $t = 1.0$ shown in ??, the vorticity is clearly concentrated in

the region with volume fraction of water $\alpha < 0.5$. To quantify this, numerically integrating the vorticity over the right-half domain we find that 97% of the circulation occurs in this region. To further illustrate the dependence of the vorticity deposition on the relative gas-liquid composition of the fluid within the interface region, Figure A.2 shows a scatter plot of the vorticity values in each cell vs the mean volume fraction of water in the cell $\langle \alpha \rangle$ (Left). The average circulation per-cell is separated into bins based on the relevant volume fraction to obtain a histogram and normalized to obtain the circulation distribution circulation as a function of α (Right). The observed circulation deposition in air-dominated fluid, $\alpha < 0.5$, and is within the predicted upper bound. This is qualitatively consistent with our analysis.

BIBLIOGRAPHY

Multibeam collection for EW9509: Multibeam data collected aboard Maurice Ewing from 1995-08-23 to 1995-09-24, departing from Chi-Lung, Taiwan and returning to Kao-hsiung, Taiwan.

Multibeam collection for KM0504: Multibeam data collected aboard Kilo Moana from 2005-02-17 to 2005-03-23, departing from Wellington, New Zealand and returning to Brisbane, Australia.

Abbot, Philip, & Dyer, Ira. 2002. Sonar Performance Predictions Incorporating Environmental Variability. Pages 611–618 of: Pace, Nicholas G., & Jensen, Finn B. (eds), *Impact of littoral environmental variability of acoustic predictions and sonar performance*. Dordrecht: Springer Netherlands.

Abbot, Philip, Dyer, Ira, Fellow, Life, & Emerson, Chris. 2006. Acoustic Propagation Uncertainty in the Shallow East China Sea. *Ieee journal of oceanic engineering*, **31**(2), 368–383.

Abgrall, Rémi. 1996. How to Prevent Pressure Oscillations in Multicomponent Flow Calculations: A Quasi Conservative Approach. *Journal of computational physics*, **125**(1), 150–160.

Alahyari Beig, Shahaboddin, & Johnsen, Eric. 2015. Maintaining interface equilibrium conditions in compressible multiphase flows using interface capturing. *Journal of computational physics*, **302**(dec), 548–566.

Allen, J S, & Roy, R a. 2000a. Dynamics of gas bubbles in viscoelastic fluids. II. Nonlinear viscoelasticity. *The journal of the acoustical society of america*, **108**(4), 1640–1650.

Allen, John S., & Roy, Ronald a. 2000b. *Dynamics of gas bubbles in viscoelastic fluids. I. Linear viscoelasticity*.

Anderson, John David. 1990. *Modern compressible flow: with historical perspective*.

Apfel, R E. 1982. Acoustic cavitation: a possible consequence of biomedical uses of ultrasound. *The british journal of cancer supplement*, **5**(mar), 140–6.

Apfel, R E, & Holland, C K. 1991. Gauging the likelihood of cavitation from short-pulse, low-duty cycle diagnostic ultrasound. *Ultrasound in medicine & biology*, **17**(2), 179–85.

Arda, Kemal, Ciledag, Nazan, Aktas, Elif, Aribas, Bilgin Kadri, & Köse, Kenan. 2011. Quantitative assessment of normal soft-tissue elasticity using shear-wave ultrasound elastography. *Ajr. american journal of roentgenology*, **197**(3), 532–6.

- Averkiou, Michalakis, Powers, Jeff, Skyba, Dan, Bruce, Matthew, & Jensen, Seth. 2003. Ultrasound Contrast Imaging Research. *Ultrasound quarterly*, **19**(1), 27–37.
- Baggs, R., Penney, D.P., Cox, C., Child, S.Z., Raeman, C.H., Dalecki, D., & Carstensen, E.L. 1996. Thresholds for ultrasonically induced lung hemorrhage in neonatal swine. *Ultrasound in medicine & biology*, **22**(1), 119–128.
- Barnett, S.B., Ter Haar, G.R., Ziskin, M.C., Nyborg, W.L., Maeda, K., & Bang, J. 1994. Current status of research on biophysical effects of ultrasound. *Ultrasound in medicine & biology*, **20**(3), 205–218.
- Bayliss, L. E., & Robertson, G. W. 1939. THE VISCO-ELASTIC PROPERTIES OF THE LUNGS. *Quarterly journal of experimental physiology and cognate medical sciences*, **29**(1), 27–47.
- Brennen, Christopher Earls. 2003. *CAVITATION AND BUBBLE DYNAMICS* by.
- Brouillette, Martin. 2002. The Richtmyer-Meshkov Instability. *Annual review of fluid mechanics*, **34**(1), 445–468.
- Brujan, EA Emil Alexandru. 2011. *Cavitation in non-newtonian fluids: With biomedical and bioengineering applications*. Berlin, Heidelberg: Springer Berlin Heidelberg.
- Calder, Brian. 2006. On the uncertainty of archive hydrographic data sets. *Ieee journal of oceanic engineering*, **31**(2), 249–265.
- Carstensen, Edwin L., Gracewski, Sheryl, & Dalecki, Diane. 2000. The search for cavitation in vivo. *Ultrasound in medicine and biology*, **26**(9), 1377–1385.
- Cavalcante, Francisco S. A. 2005. Mechanical interactions between collagen and proteoglycans: implications for the stability of lung tissue. *Journal of applied physiology*, **98**(2), 672–679.
- Child, S.Z., Hartman, C.L., Schery, L.A., & Carstensen, E.L. 1990. Lung damage from exposure to pulsed ultrasound. *Ultrasound in medicine & biology*, **16**(8), 817–825.
- Church, Charles C. 2002. Spontaneous homogeneous nucleation, inertial cavitation and the safety of diagnostic ultrasound. *Ultrasound in medicine & biology*, **28**(10), 1349–1364.
- Claudon, Michel, Dietrich, Christoph F C.F., Choi, B.I. Byung Ihn, Cosgrove, David O D.O., Kudo, Masatoshi, Nolsøe, Christian P, Piscaglia, Fabio, Wilson, S.R. Stephanie R, Barr, Richard G, Chammam, Maria C, Chaubal, Nitin G, Chen, Min-Hua M.H., Clevert, D.A. Dirk Andre, Correas, Jean Michel J.M., Ding, Hong, Forsberg, Flemming, Fowlkes, J Brian, Gibson, Robert N, Goldberg, B.B. Barry B, Lassau, Nathalie, Leen, Edward L S, Mattrey, Robert F, Moriyasu, Fuminori, Solbiati, Luigi, Weskott, Hans-Peter H.P., Xu, Hui-Xiong H.X., World Federation for Ultrasound in Medicine, R., European Federation of Societies for Ultrasound, H., Castaing, D., Waechter, F, Navarro, F, Abascal, A., Majno, P, Engerran, L., Albrecht, T., Blomley, M.J., Bolondi, L., Claudon, Michel, Correas, Jean Michel J.M., Cosgrove, David O D.O., Greiner, L., Jager, K., Jong, N.D., Leen, Edward L S, Lencioni, R., Lindsell, D., Martegani, A., Solbiati, Luigi, Thorelius, L., Tranquart, F., Weskott, Hans-Peter H.P., Whittingham, T., Arita,

J., Hasegawa, K., Takahashi, M., Hata, S., Shindoh, J., Sugawara, Y., Kokudo, N., Averkiou, M., Powers, J., Skyba, D.M., Bruce, M., Jensen, S., Barreiros, A.P., Piscaglia, Fabio, Dietrich, Christoph F C.F., Bernatik, T., Seitz, K., Blank, W., Schuler, A., Dietrich, Christoph F C.F., Strobel, D., Berstad, A.E., Brabrand, K., Foss, A., Bolondi, L., Gaiani, S., Celli, N., Golfieri, R., Grigioni, W.F., Leoni, S., Venturi, A.M., Piscaglia, Fabio, Boozari, B., Soudah, B., Rifai, K., Schneidewind, S., Vogel, A., Hecker, H., Hahn, A., Schlue, J., Dietrich, Christoph F C.F., Bahr, M.J., Kubicka, S., Manns, M.P., Gebel, M., Bos, L.J., Piek, J.J., Spaan, J.A., Bruix, J., Sherman, M., Bruix, J., Sherman, M., Bruix, J., Sherman, M., Llovet, J.M., Beaugrand, M., Lencioni, R., Burroughs, A.K., Christensen, E., Pagliaro, L., Colombo, M., Rodes, J., Cantisani, V., Ricci, P., Erturk, M., Pagliara, E., Drudi, F.M., Calliada, F., Mortele, K., D'Ambrosio, U., Marigliano, C., Catalano, C., Marin, D., Seri, M. Di, Longo, F., Passariello, R., Cao, B.S., Li, X.L., Li, N., Wang, Z.Y., Catalano, O., Sandomenico, F., Nunziata, A., Raso, M.M., Vallone, P., Siani, A., Catalano, O., Sandomenico, F., Raso, M.M., Siani, A., Cervone, A., Sardi, A., Conaway, G.L., Chami, L., Lassau, Nathalie, Malka, D., Ducreux, M., Bidault, S., Roche, A., Elias, D., Charnley, R.M., Morris, D.L., Dennison, A.R., Amar, S.S., Hardcastle, J.D., Chen, L.D., Xu, Hui-Xiong H.X., Xie, X.Y. X.H., Lu, M.Q. M.D., Xu, Z.F., Liu, G.J., Liang, J.Y., Lin, M.X., Chen, L.D., Xu, Hui-Xiong H.X., Xie, X.Y. X.H., Xie, X.Y. X.H., Xu, Z.F., Liu, G.J., Wang, Z.Y., Lin, M.X., Lu, M.Q. M.D., Chen, Min-Hua M.H., Dai, Y., Yan, K., Fan, Z.H., Yin, S.S., Yang, W., Wu, W., Wang, Y.B., Li, J.Y., Chen, Min-Hua M.H., Wei, Y., Yan, K., Gao, W., Dai, Y., Huo, L., Yin, S.S., Zhang, H., Poon, R.T., Chen, Min-Hua M.H., Yang, W., Yan, K., Dai, Y., Wu, W., Fan, Z.H., Callstrom, M.R., Charboneau, J.W., Chen, Min-Hua M.H., Yang, W., Yan, K., Zou, M.W., Solbiati, Luigi, Liu, J.B., Dai, Y., Choi, D., Lim, H.K., Lee, W.J., Kim, S.H., Kim, Y.H., Kim, S.H., Lim, J.H., Claudon, Michel, Cosgrove, David O D.O., Albrecht, T., Bolondi, L., Bosio, M., Calliada, F., Correas, Jean Michel J.M., Darge, K., Dietrich, Christoph F C.F., D'Onofrio, M., Evans, D.H., Filice, C., Greiner, L., Jager, K., Jong, N.D., Leen, Edward L S, Lencioni, R., Lindsell, D., Martegani, A., Meairs, S., Nolsoe, C., Piscaglia, Fabio, Ricci, P., Seidel, G., Skjoldbye, B., Solbiati, Luigi, Thorelius, L., Tranquart, F., Weskott, Hans-Peter H.P., Whittingham, T., Clevert, D.A. Dirk Andre, Stickel, M., Minaifar, N., Lohe, F., Graeb, C., Jauch, K.W., Reiser, M., Conlon, R., Jacobs, M., Dasgupta, D., Lodge, J.P., Cosgrove, David O D.O., Harvey, C., Cosgrove, David O D.O., Lassau, Nathalie, Crocetti, L., Lencioni, R., Debeni, S., See, T.C., Pina, C.D., Bartolozzi, C., Dawson, P., Cosgrove, David O D.O., Grainger, R., Giorgi, U. De, Aliberti, C., Benea, G., Conti, M., Marangolo, M., Dietrich, Christoph F C.F., Averkioui, M.A., Correas, Jean Michel J.M., Lassau, Nathalie, Leen, Edward L S, Piscaglia, Fabio, Dietrich, Christoph F C.F., Braden, B., Hocke, M., Ott, M., Ignee, A., Dietrich, Christoph F C.F., Ignee, A., Hocke, M., Schreiber-Dietrich, D., Greis, C., Dietrich, Christoph F C.F., Kratzer, W., Strobe, D., Danse, E., Fessl, R., Bunk, A., Vossas, U., Hauenstein, K., Koch, W., Blank, W., Oudkerk, M., Hahn, D., Greis, C., Dietrich, Christoph F C.F., Mertens, J.C., Braden, B., Schuessler, G., Ott, M., Ignee, A., Dietrich, Christoph F C.F., Schuessler, G., Trojan, J., Fellbaum, C., Ignee, A., Ding, Hong, Wang, W.P., Huang, B.J., Wei, R.X., He, N.A., Qi, Q., Li, C.L., Dodd, G.D., Memel, D.S., Zajko, A.B., Baron, R.L., Santaguida, L.A., , Biology), EFSUMB (European Federation of Societies for Ultrasound in Medicine, , Biology), EFSUMB (European Federation of Societies for Ultrasound in Medicine, Ellsmere, J., Kane, R., Grinbaum, R., Edwards, M., Schneider, B., Jones, D., Exuzides, A., Main, M.L., Colby, C., Grayburn, P.A., Feinstein, S.B., Goldman, J.H., Fan, Z.H., Chen, Min-Hua M.H., Dai, Y., Wang, Y.B., Yan, K., Wu, W., Yang, W., Yin, S.S., Ferrara, N., Kerbel, R.S., Finlay, I.G., Meek, D., Brunton, F., McArdle, C.S.,

Fioole, B., de Haas, R.J., Wicherts, D.A., Elias, S.G., Scheffers, J.M., van Hillegersberg, R., van Leeuwen, M.S., Rinkes, I.H. Borel, Flint, E.W., Sumkin, J.H., Zajko, A.B., Bowen, A., Fong, Y., Forner, A., Vilana, R., Ayuso, C., Bianchi, L., Sole, M., Ayuso, J.R., Boix, L., Sala, M., Varela, M., Llovet, J.M., Bru, C., Bruix, J., Forsberg, Flemming, Kuruvilla, B., Pascua, M.B., Chaudhari, M.H., Merton, D.A., Palazzo, J.P., Goldberg, B.B. Barry B, Foschi, F.G., Dall'Aglio, A.C., Marano, G., Lanzi, A., Savini, P., Piscaglia, Fabio, Serra, C., Cursaro, C., Bernardi, M., Andreone, P., Stefanini, G.F., Gillams, A.R., Lees, W.R., Guibal, A., Taillade, L., Mule, S., Comperat, E., Badachi, Y., Golmard, J.L., Guillou-Buffello, D. Le, Rixe, O., Bridal, S.L., Lucidarme, O., Hatanaka, K., Kudo, Masatoshi, Minami, Y., Maekawa, K., Hatanaka, K., Kudo, Masatoshi, Minami, Y., Ueda, T., Tatsumi, C., Kitai, S., Takahashi, S., Inoue, T., Hagiwara, S., Chung, H., Ueshima, K., Maekawa, K., Hirche, T.O., Ignee, A., Hirche, H., Schneider, A., Dietrich, Christoph F C.F., Huang, D., Chen, Y., Li, K., Zhang, Q., Iavarone, M., Sangiovanni, A., Forzenigo, L.V., Massironi, S., Fraquelli, M., Aghemo, A., Ronchi, G., Biondetti, P., Roncalli, M., Colombo, M., Ignee, A., Piscaglia, Fabio, Ott, M., Salvatore, V., Dietrich, Christoph F C.F., Inoue, T., Kudo, Masatoshi, Hatanaka, K., Takahashi, S., Kitai, S., Ueda, T., Ishikawa, E., Hagiwara, S., Minami, Y., Chung, H., Ueshima, K., Maekawa, K., Neoplasia, International Consensus Group for Hepatocellular, Jain, A., Reyes, J., Kashyap, R., Dodson, S.F., Demetris, A.J., Ruppert, K., Abu-Elmagd, K., Marsh, W., Madariaga, J., Mazariegos, G., Geller, D., Bonham, C.A., Gayowski, T., Cacciarelli, T., Fontes, P., Starzl, T.E., Fung, J.J., Jang, H.J., Kim, T.K., Burns, P.N., Wilson, S.R. Stephanie R, Jarnagin, W.R., Bach, A.M., Winston, C.B., Hann, L.E., Heffernan, N., Loumeau, T., DeMatteo, R.P., Fong, Y., Blumgart, L.H., Kessler, T., Bayer, M., Schwoppe, C., Liersch, R., Mesters, R.M., Berdel, W.E., Khawaja, O.A., Shaikh, K.A., Al-Mallah, M.H., Kisaka, Y., Hirooka, M., Kumagi, T., Uehara, T., Hiasa, Y., Kumano, S., Tanaka, H., Michitaka, K., Horiike, N., Mochizuki, T., Onji, M., Konopke, R., Bunk, A., Kersting, S., Konopke, R., Kersting, S., Bergert, H., Bloomenthal, A., Gastmeier, J., Saeger, H.D., Bunk, A., Korenaga, K., Korenaga, M., Furukawa, M., Yamasaki, T., Sakaida, I., Kudo, Masatoshi, Kudo, Masatoshi, Hatanaka, K., Kumada, T., Toyoda, H., Tada, T., Kudo, Masatoshi, Hatanaka, K., Maekawa, K., Kudo, Masatoshi, Izumi, N., Kokudo, N., Matsui, O., Sakamoto, M., Nakashima, O., Kojiro, M., Makuuchi, M., Kudo, Masatoshi, Okanoue, T., Kurt, M., Shaikh, K.A., Peterson, L., Kurrelmeyer, K.M., Shah, G., Nagueh, S.F., Fromm, R., Quinones, M.A., Zoghbi, W.A., Lamuraglia, M., Escudier, B.J., Chami, L., Schwartz, B., Leclere, J., Roche, A., Lassau, Nathalie, Langnas, A.N., Marujo, W., Stratta, R.J., Wood, R.P., Shaw, B.W., Larsen, L.P., Rosenkilde, M., Christensen, H., Bang, N., Bolvig, L., Christiansen, T., Laurberg, S., Lassau, Nathalie, Chami, L., Chebil, M., Benatsou, B., Bidault, S., Girard, E., Abboud, G., Roche, A., Lassau, Nathalie, Chami, L., Koscielny, S., Chebil, M., Massard, C., Benatsou, B., Bidault, S., Cioffi, A., Blay, J.Y., Cesne, A. Le, Lassau, Nathalie, Koscielny, S., Albiges, L., Chami, L., Benatsou, B., Chebil, M., Roche, A., Escudier, B.J., Lassau, Nathalie, Koscielny, S., Chami, L., Chebil, M., Benatsou, B., Roche, A., Ducreux, M., Malka, D., Boige, V., Lassau, Nathalie, Lamuraglia, M., Chami, L., Leclere, J., Bonvalot, S., Terrier, P., Roche, A., Cesne, A. Le, Leen, Edward L S, Ceccotti, P., Moug, S.J., Glen, P., MacQuarrie, J., Angerson, W.J., Albrecht, T., Hohmann, J., Oldenburg, A., Ritz, J.P., Horgan, P.G., Lencioni, R., Llovet, J.M., Leoni, S., Piscaglia, Fabio, Golfieri, R., Camaggi, V., Vidili, G., Pini, P., Bolondi, L., Li, N., Ding, Hong, Fan, P., Lin, X., Xu, C., Wang, W.P., Xu, Z.F., Wang, J., Lim, A.K., Taylor-Robinson, S.D., Patel, N., Eckersley, R.J., Goldin, R.D., Hamilton, G., Foster, G.R., Thomas, H.C., Cosgrove, David O D.O., Blomley, M.J., Liu, G.J., Lu, M.Q. M.D., Xie, X.Y. X.H., Xu, Hui-Xiong H.X.,

Xu, Z.F., Zheng, Y.L., Liang, J.Y., Wang, W.P., Liu, J.B., Wansaicheong, G., Merton, D.A., Chiou, S.Y., Sun, Y., Li, K., Forsberg, Flemming, Edmonds, P.R., Needleman, L., Halpern, E.J., Liu, Z., Lobo, S.M., Humphries, S., Horkan, C., Solazzo, S.A., Hines-Peralta, A.U., Lenkinski, R.E., Goldberg, S.N., Livraghi, T., Goldberg, S.N., Lazzaroni, S., Meloni, F., Ierace, T., Solbiati, Luigi, Gazelle, G.S., Lu, Q., Zhong, X.F., Huang, Z.X., Yu, B.Y., Ma, B.Y., Ling, W.W., Wu, H., Yang, J.Y., Luo, Y., Luo, Y., Fan, Y.T., Lu, Q., Li, B., Wen, T.F., Zhang, Z.W., Main, M.L., Goldman, J.H., Grayburn, P.A., Main, M.L., Ryan, A.C., Davis, T.E., Albano, M.P., Kusnetzky, L.L., Hibberd, M., Mandry, D., Bressenot, A., Galloy, M.A., Chastagner, P., Branchereau, S., Claudon, Michel, Maruyama, H., Takahashi, M., Ishibashi, H., Okugawa, H., Okabe, S., Yoshikawa, M., Yokosuka, O., Matsui, O., Mazzoni, G., Napoli, A., Mandetta, S., Miccini, M., Cassini, D., Gregori, M., Colace, L., Tocchi, A., Minami, Y., Kudo, Masatoshi, Chung, H., Kawasaki, T., Yagyu, Y., Shimono, T., Shiozaki, H., Moriyasu, Fuminori, Itoh, K., Mork, H., Ignee, A., Schuessler, G., Ott, M., Dietrich, Christoph F C.F., Nakano, H., Ishida, Y., Hatakeyama, T., Sakuraba, K., Hayashi, M., Sakurai, O., Hataya, K., Omata, M., Lesmana, L.A., Tateishi, R., Chen, P.J., Lin, S.M., Yoshida, H., Kudo, Masatoshi, Lee, J.M., Choi, B.I., Byung Ihn, Poon, R.T., Shiina, S., Cheng, A.L., Jia, J.D., Obi, S., Han, K.H., Jafri, W., Chow, P., Lim, S.G., Chawla, Y.K., Budihusodo, U., Gani, R.A., Lesmana, C.R., Putranto, T.A., Liaw, Y.F., Sarin, S.K., Peronneau, P., Lassau, Nathalie, Leguerney, I., Roche, A., Cosgrove, David O D.O., Piscaglia, Fabio, Bolondi, L., Piscaglia, Fabio, Corradi, F., Mancini, M., Giangregorio, F., Tamberi, S., Ugolini, G., Cola, B., Bazzocchi, A., Righini, R., Pini, P., Fornari, F., Bolondi, L., Piscaglia, Fabio, Gianstefani, A., Ravaioli, M., Golfieri, R., Cappelli, A., Giampalma, E., Sagrini, E., Imbriaco, G., Pinna, A.D., Bolondi, L., Piscaglia, Fabio, Nolsoe, C., Dietrich, Christoph F C.F., Cosgrove, David O D.O., Gilja, O.H., Nielsen, M., Bachmann, Albrecht, T., Barozzi, L., Bertolotto, M., Catalano, O., Claudon, Michel, Clevert, D.A., Dirk Andre, Correas, Jean Michel J.M., D'Onofrio, M., Drudi, F.M., Eyding, J., Giovannini, M., Hocke, M., Ignee, A., Jung, E.M., Klauser, A.S., Lassau, Nathalie, Leen, Edward L S, Mathis, G., Saftoiu, A., Seidel, G., Sidhu, P.S., ter Haar, G., Timmerman, D., Weskott, Hans-Peter H.P., Piskunowicz, M., Kosiak, W., Irga, N., Qiang, L., Yan, L., Chao-Xin, Y., Zeng, Y., Wu, H., Lei, Z., Zhong, Y., Fan, Y.T., Wang, H.H., Luo, Y., Quaia, E., D'Onofrio, M., Palumbo, A., Rossi, S., Bruni, S., Cova, M., Ridolfi, F., Abbattista, T., Marini, F., Vedovelli, A., Quagliarini, P., Busilacchi, P., Brunelli, E., Rossi, S., Rosa, L., Ravetta, V., Cascina, A., Quaretti, P., Azzaretti, A., Scagnelli, P., Tinelli, C., Dionigi, P., Calliada, F., Sangiovanni, A., Manini, M.A., Iavarone, M., Romeo, R., Forzenigo, L.V., Fraquelli, M., Massironi, S., Corte, C., Della, Ronchi, G., Rumi, M.G., Biondetti, P., Colombo, M., Sasaki, A., Kai, S., Iwashita, Y., Hirano, S., Ohta, M., Kitano, S., Scheele, J., Stang, R., Altendorf-Hofmann, A., Paul, M., Schlottmann, K., Klebl, F., Zorger, N., Feuerbach, S., Scholmerich, J., Schuessler, G., Fellbaum, C., Fauth, F., Jacobi, V., Schmidt-Mathiesen, A., Ignee, A., Dietrich, Christoph F C.F., Seitz, K., Bernatik, T., Strobel, D., Blank, W., Friedrich-Rust, M., Strunk, H., Greis, C., Kratzer, W., Schuler, A., Seitz, K., Greis, C., Schuler, A., Bernatik, T., Blank, W., Dietrich, Christoph F C.F., Strobel, D., Shaw, A.S., Ryan, S.M., Beese, R.C., Sidhu, P.S., Shiozawa, K., Watanabe, M., Takayama, R., Takahashi, M., Wakui, N., Iida, K., Sumino, Y., Sidhu, P.S., Shaw, A.S., Ellis, S.M., Karani, J.B., Ryan, S.M., Simpson, D.H., Chin, C.T., Burns, P.N., Skyba, D.M., Price, R.J., Linka, A.Z., Skalak, T.C., Kaul, S., Sorrentino, P., D'Angelo, S., Tarantino, L., Ferbo, U., Bracigliano, A., Vecchione, R., Strobel, D., Kleinecke, C., Hansler, J., Frieser, M., Handl, T., Hahn, E.G., Bernatik, T., Strobel, D., Seitz, K., Blank, W., Schuler, A., Dietrich, Christoph F C.F., von Herbay, A., Friedrich-Rust,

M., Kunze, G., Becker, D., Will, U., Kratzer, W., Albert, F.W., Pachmann, C., Dirks, K., Strunk, H., Greis, C., Bernatik, T., Su, H.L., Qian, Y.Q., Wei, Z.R., He, J.G., Li, G.Q., Zhang, J., Zhou, X.D., Jing, W., Therasse, P., Arbuck, S.G., Eisenhauer, E.A., Wanders, J., Kaplan, R.S., Rubinstein, L., Verweij, J., Glabbeke, M. Van, van Oosterom, A.T., Christian, M.C., Gwyther, S.G., Tiemann, K., Lohmeier, S., Kuntz, S., Köster, J., Pohl, C., Burns, P.N., Porter, T.R., Nanda, N.C., Lüderitz, B., Becher, H., Torzilli, G., Fabbro, D. Del, Palmisano, A., Donadon, M., Bianchi, P., Roncalli, M., Balzarini, L., Montorsi, M., Torzilli, G., Fabbro, D. Del, Palmisano, A., Donadon, M., Montorsi, M., Trillaud, H., Bruel, J.M., Valette, P.J., Vilgrain, V., Schmutz, G., Oyen, R., Jakubowski, W., Danes, J., Valek, V., Greis, C., Vilana, R., Forner, A., Bianchi, L., Garcia-Criado, A., Rimola, J., de Lope, C.R., Reig, M., Ayuso, C., Bru, C., Bruix, J., Wang, Z.Y., Xu, Hui-Xiong H.X., Xie, X.Y. X.H., Xie, X.Y. X.H., Kuang, M., Xu, Z.F., Liu, G.J., Chen, L.D., Lin, M.X., Lu, M.Q. M.D., Wei, K., Jayaweera, A.R., Firoozan, S., Linka, A.Z., Skyba, D.M., Kaul, S., Wilson, S.R. Stephanie R, Burns, P.N., Wilson, S.R. Stephanie R, Kim, T.K., Jang, H.J., Burns, P.N., Wu, W., Chen, Min-Hua M.H., Yin, S.S., Yan, K., Fan, Z.H., Yang, W., Dai, Y., Huo, L., Li, J.Y., Xu, Hui-Xiong H.X., Liu, G.J., Lu, M.Q. M.D., Xie, X.Y. X.H., Xu, Z.F., Zheng, Y.L., Liang, J.Y., Xu, Hui-Xiong H.X., Lu, M.Q. M.D., Liu, G.J., Xie, X.Y. X.H., Xu, Z.F., Zheng, Y.L., Liang, J.Y., Yanagisawa, K., Moriyasu, Fuminori, Miyahara, T., Yuki, M., Iijima, H., Zheng, R.Q., Mao, R., Ren, J., Xu, E.J., Liao, M., Wang, P., Lu, M.Q. M.D., Yang, Y., Cai, C.J., & Chen, G.H. 2013. Guidelines and good clinical practice recommendations for Contrast Enhanced Ultrasound (CEUS) in the liver - update 2012: A WFUMB-EFSUMB initiative in cooperation with representatives of AFSUMB, AIUM, ASUM, FLAUS and ICUS. *Ultrasound in medicine & biology*, **39**(2), 187–210.

Collins, Michael D. 1994. Generalization of the split-step Padé solution. *The journal of the acoustical society of america*, **96**(1), 382.

Dalecki, D, Keller, B B, Raeman, C H, & Carstensen, E L. 1993. Effects of pulsed ultrasound on the frog heart: I. Thresholds for changes in cardiac rhythm and aortic pressure. *Ultrasound in medicine & biology*, **19**(5), 385–90.

Dalecki, Diane, Child, Sally Z., Raeman, Carol H., Cox, Christopher, & Carstensen, Edwin L. 1997. Ultrasonically induced lung hemorrhage in young swine. *Ultrasound in medicine and biology*, **23**(5), 777–781.

Drake, Paul. 2006. *High-Energy-Density Physics*. Shock Wave and High Pressure Phenomena. Springer Berlin Heidelberg.

Dussik, K T. 1942. On the possibility of using ultrasound waves as a diagnostic aid. *Z neurol Psychiatr*, **174**, 153–168.

Edelman, Sidney. 2005. *Understanding ultrasound physics*. Woodlands, Texas: ESP.

Emerson, Chris, Lynch, James F., Abbot, Philip, Lin, Ying-Tsong, Duda, Timothy F., Gawarkiewicz, Glen G., & Chen, Chi-Fang. 2014. Acoustic Propagation Uncertainty and Probabilistic Prediction of Sonar System Performance in the Southern East China Sea Continental Shelf and Shelfbreak Environments. *Ieee journal of oceanic engineering*, 1–15.

- Faffe, Débora S., Rocco, Patricia R. M., Negri, Elnara M., & Zin, Walter A. 2002. Comparison of rat and mouse pulmonary tissue mechanical properties and histology. *Journal of applied physiology*, **92**(1), 230–234.
- Finette, Steven. 2005. Embedding uncertainty into ocean acoustic propagation models (L). *The journal of the acoustical society of america*, **117**(3), 997.
- Finette, Steven. 2006. A stochastic representation of environmental uncertainty and its coupling to acoustic wave propagation in ocean waveguides. *The journal of the acoustical society of america*, **120**(5), 2567.
- Finette, Steven. 2009. A stochastic response surface formulation of acoustic propagation through an uncertain ocean waveguide environment. *The journal of the acoustical society of america*, **126**(5), 2242–7.
- Flynn, H. G. 1975. Cavitation dynamics. I. A mathematical formulation. *The journal of the acoustical society of america*, **57**(6), 1379.
- Flynn, H. G. 1982. Generation of transient cavities in liquids by microsecond pulses of ultrasound. *The journal of the acoustical society of america*, **72**(6), 1926.
- Fraley, Gary. 1986. RayleighTaylor stability for a normal shock wave density discontinuity interaction. *Physics of fluids*, **29**(2), 376.
- Frizzell, Leon A. 1976. Shear properties of mammalian tissues at low megahertz frequencies. *The journal of the acoustical society of america*, **60**(6), 1409.
- Frizzell, Leon a., Chen, Ellen, & Lee, Chong. 1994. Effects of pulsed ultrasound on the mouse neonate: Hind limb paralysis and lung hemorrhage. *Ultrasound in medicine and biology*, **20**(1), 53–63.
- Frizzell, Leon A., Zachary, James F., O'Brien, William D., & O'Brien, William D. 2003. Effect of pulse polarity and energy on ultrasound-induced lung hemorrhage in adult rats. *The journal of the acoustical society of america*, **113**(5), 2912.
- Gerstoft, P., Huang, C.-F., & Hodgkiss, W.S. 2006. Estimation of Transmission Loss in the Presence of Geoacoustic Inversion Uncertainty. *Ieee journal of oceanic engineering*, **31**(2), 299–307.
- Harrison, G.H. H, Eddy, H.A. A, Wang, J.-P. P, & Liberman, F.Z. Z. 1995. Microscopic lung alterations and reduction of respiration rate in insonated anesthetized swine. *Ultrasound in medicine & biology*, **21**(7), 981–983.
- Heaney, K.D., & Cox, H. 2006. A Tactical Approach to Environmental Uncertainty and Sensitivity. *Ieee journal of oceanic engineering*, **31**(2), 356–367.
- Heifetz, E., & Mak, J. 2015. Stratified shear flow instabilities in the non-Boussinesq regime. *Physics of fluids*, **27**(8), 086601.

- Henry de Frahan, M. T., Movahed, P., & Johnsen, E. 2015a. Numerical simulations of a shock interacting with successive interfaces using the Discontinuous Galerkin method: the multilayered RichtmyerMeshkov and RayleighTaylor instabilities. *Shock waves*, **25**(4), 329–345.
- Henry de Frahan, Marc T., Varadan, Sreenivas, & Johnsen, Eric. 2015b. A new limiting procedure for discontinuous Galerkin methods applied to compressible multiphase flows with shocks and interfaces. *Journal of computational physics*, **280**(jan), 489–509.
- Holland, Christy K., Deng, Cheri X., Apfel, Robert E., Alderman, Jonathan L., Fernandez, Leonardo A., & Taylor, Kenneth J.W. 1996. Direct evidence of cavitation in vivo from diagnostic ultrasound. *Ultrasound in medicine & biology*, **22**(7), 917–925.
- Jacobs, J. W., & Sheeley, J. M. 1996. Experimental study of incompressible RichtmyerMeshkov instability. *Physics of fluids*, **8**(2), 405.
- James, Kevin R., & Dowling, David R. 2008. A method for approximating acoustic-field-amplitude uncertainty caused by environmental uncertainties. *The journal of the acoustical society of america*, **124**(3), 1465–1476.
- James, Kevin R., & Dowling, David R. 2011. Pekeris waveguide comparisons of methods for predicting acoustic field amplitude uncertainty caused by a spatially uniform environmental uncertainty (L). *The journal of the acoustical society of america*, **129**(2), 589–592.
- Jensen, Finn B., Kuperman, William A., Porter, Michael B., & Schmidt, Henrik. 2011. *Computational Ocean Acoustics*. Springer Science & Business Media.
- Johnsen, Eric, & Colonius, Tim. 2009. Numerical simulations of non-spherical bubble collapse. *Journal of fluid mechanics*, **629**(jun), 231.
- Johnsen, Eric, & Hua, Chengyun. 2012. Bubble Dynamics in a Standard Linear Solid (Viscoelastic) Medium. *Pages 103–107 of: Proceedings of the 8th international symposium on cavitation*. Singapore: Research Publishing Services.
- Keller, Joseph B. 1980. Bubble oscillations of large amplitude. *The journal of the acoustical society of america*, **68**(2), 628.
- Kinsler, Lawrence E., Frey, Austin R., Coppens, Alan B., & Sanders, James V. 1982. Fundamentals of Acoustics by Lawrence. *The journal of the acoustical society of america*, **72**(3), 1090.
- Knust, Juliane, Ochs, Matthias, Gundersen, Hans Jørgen G., & Nyengaard, Jens R. 2008. Stereological Estimates of Alveolar Number and Size and Capillary Length and Surface Area in Mice Lungs. *The anatomical record: Advances in integrative anatomy and evolutionary biology*, **292**(1), 113–122.
- Kramer, J. M., Waldrop, T. G., Frizzell, L. A., Zachary, J. F., & O'Brien, W D. 2001. Cardiopulmonary function in rats with lung hemorrhage induced by pulsed ultrasound exposure. *Journal of ultrasound in medicine : official journal of the american institute of ultrasound in medicine*, **20**(11), 1197–1206.

- Krouskop, T A, Wheeler, T M, Kallel, F, Garra, B S, & Hall, T. 1998. Elastic Moduli of Breast and Prostate Tissues under Compression. *Ultrasonic imaging*, **20**(4), 260–274.
- Latini, Marco, Schilling, Oleg, & Don, Wai Sun. 2007. Effects of WENO flux reconstruction order and spatial resolution on reshocked two-dimensional RichtmyerMeshkov instability. *Journal of computational physics*, **221**(2), 805–836.
- LEHMANN, J F, & HERRICK, J F. 1953. Biologic reactions to cavitation, a consideration for ultrasonic therapy. *Archives of physical medicine and rehabilitation*, **34**(2), 86–98.
- Leighton, T. G. 1997. *The Acoustic Bubble, Volume 10*. Academic Press.
- Lichtenstein, Daniel A. 2009. Ultrasound examination of the lungs in the intensive care unit. *Pediatric critical care medicine : a journal of the society of critical care medicine and the world federation of pediatric intensive and critical care societies*, **10**(6), 693–698.
- Linder, C.A., Gawarkiewicz, G.G., & Taylor, Maureen. 2006. Climatological Estimation of Environmental Uncertainty Over the Middle Atlantic Bight Shelf and Slope. *Ieee journal of oceanic engineering*, **31**(2), 308–324.
- Livingston, E.S. S., Goff, J.A. a., Finette, S., Abbot, P., Lynch, J.F. F., & Hodgkiss, W.S. S. 2006. Guest editorial: Capturing uncertainty in the tactical ocean environment. *Ieee journal of oceanic engineering*, **31**(2), 245–248.
- MacRobbie, Alan G., Raeman, Carol H., Child, Sally Z., & Dalecki, Diane. 1997. Thresholds for premature contractions in murine hearts exposed to pulsed ultrasound. *Ultrasound in medicine & biology*, **23**(5), 761–765.
- Madsen, E L, Sathoff, H J, & Zagzebski, J A. 1983. Ultrasonic shear wave properties of soft tissues and tissuelike materials. *The journal of the acoustical society of america*, **74**(5), 1346–1355.
- Marmottant, Philippe, van der Meer, Sander, Emmer, Marcia, Versluis, Michel, de Jong, Nico, Hilgenfeldt, Sascha, & Lohse, Detlef. 2005. A model for large amplitude oscillations of coated bubbles accounting for buckling and rupture. *The journal of the acoustical society of america*, **118**(6), 3499.
- Meltzer, Richard S., Adsumelli, Rishi, Risher, William H., Hicks, George L., Stern, David H., Shah, Pratima M., Wojtczak, Jacek A., Lustik, Stewart J., Gayeski, Thomas E., Shapiro, Janine R., & Carstensen, Edwin L. 1998. Lack of Lung Hemorrhage in Humans After Intraoperative Transesophageal Echocardiography with Ultrasound Exposure Conditions Similar to Those Causing Lung Hemorrhage in Laboratory Animals. *Journal of the american society of echocardiography*, **11**(1), 57–60.
- Meshkov, E. E. 1972. Instability of the interface of two gases accelerated by a shock wave. *Fluid dynamics*, **4**(5), 101–104.
- Meyer, K. A. 1972. Numerical Investigation of the Stability of a Shock-Accelerated Interface between Two Fluids. *Physics of fluids*, **15**(5), 753.

- Miller, DL. 2012. Induction of Pulmonary Hemorrhage in Rats During Diagnostic Ultrasound. *Ultrasound in medicine & biology*, **38**(8), 1476–1482.
- Miller, Douglas L. 2016. Mechanisms for Induction of Pulmonary Capillary Hemorrhage by Diagnostic Ultrasound: Review and Consideration of Acoustical Radiation Surface Pressure. *Ultrasound in medicine & biology*, **42**(12), 2743–2757.
- Miller, Douglas L., & Thomas, Ronald M. 1994. Heating as a mechanism for ultrasonically-induced petechial hemorrhages in mouse intestine. *Ultrasound in medicine & biology*, **20**(5), 493–503.
- Miller, Douglas L., Averkiou, Michalakis A, Brayman, Andrew A, Everbach, E Carr, Holland, Christy K, Wible, James H, & Wu, Junru. 2008a. Bioeffects considerations for diagnostic ultrasound contrast agents. *Journal of ultrasound in medicine : official journal of the american institute of ultrasound in medicine*, **27**(4), 611–632; quiz 633–636.
- Miller, Douglas L., Dou, Chunyan, & Wiggins, Roger C. 2008b. Frequency Dependence of Kidney Injury Induced by Contrast-Aided Diagnostic Ultrasound in Rats. *Ultrasound in medicine and biology*, **34**(10), 1678–1687.
- Miller, Douglas L., Dou, Chunyan, & Raghavendran, Krishnan. 2015. Dependence of Thresholds for Pulmonary Capillary Hemorrhage on Diagnostic Ultrasound Frequency. *Ultrasound in medicine & biology*, **41**(6), 1640–1650.
- Munk, Walter H. 1994. The Heard Island Feasibility Test. *The journal of the acoustical society of america*, **96**(4), 2330.
- Nyborg, Wesley L. 2001. Biological effects of ultrasound: Development of safety guidelines. Part II: General review. *Ultrasound in medicine & biology*, **27**(3), 301–333.
- O'Brien, W.D., Jr., Simpson, D.G., Frizzell, L.a., & Zachary, J.F. 2001a. Age-dependent threshold and superthreshold behavior of ultrasound-induced lung hemorrhage in pigs. *2001 ieee ultrasonics symposium. proceedings. an international symposium (cat. no.01ch37263)*, **2**(6).
- O'Brien, W D, Frizzell, Leon A., Weigel, Ronald M., Zachary, James F., O'Brien, William D., Frizzell, Leon A., Weigel, Ronald M., & Zachary, James F. 2000. Ultrasound-induced lung hemorrhage is not caused by inertial cavitation. *The journal of the acoustical society of america*, **108**(3), 1290–1297.
- O'Brien, W.D., Simpson, D.G., Frizzell, L.A., & Zachary, J.F. 2001b. Superthreshold behavior and threshold estimates of ultrasound-induced lung hemorrhage in adult rats: role of beamwidth. *Ieee transactions on ultrasonics, ferroelectrics and frequency control*, **48**(6), 1695–1705.
- O'Brien, W.D., Simpson, D.G. Douglas G, Moon-Ho Ho, Miller, R.J. Rita J, Frizzell, Leon A L.A., Zachary, James F J.F., Brien, William D O, Simpson, D.G. Douglas G, Ho, Moon-ho, Miller, R.J. Rita J, Frizzell, Leon A L.A., Member, Senior, & Zachary, James F J.F. 2003a. Superthreshold behavior and threshold estimation of ultrasound-induced lung hemorrhage in pigs: Role of age dependency. *Ieee transactions on ultrasonics, ferroelectrics and frequency control*, **50**(2), 153–169.

- O'Brien, William D, Frizzell, Leon A, Schaeffer, David J, & Zachary, James F. 2001c. Superthreshold behavior of ultrasound-induced lung hemorrhage in adult mice and rats: role of pulse repetition frequency and exposure duration. *Ultrasound in medicine & biology*, **27**(2), 267–277.
- O'Brien, William D., Kramer, Jeffrey M., Waldrop, Tony G., Frizzell, Leon A., Miller, Rita J., Blue, James P., & Zachary, James F. 2002. Ultrasound-induced lung hemorrhage: Role of acoustic boundary conditions at the pleural surface. *The journal of the acoustical society of america*, **111**(2), 1102.
- O'Brien, William D., Simpson, Douglas G., Frizzell, Leon a., & Zachary, James F. 2003b. Threshold estimates and superthreshold behavior of ultrasound-induced lung hemorrhage in adult rats: Role of pulse duration. *Ultrasound in medicine and biology*, **29**(11), 1625–1634.
- O'Brien, William D., Simpson, Douglas G., Frizzell, Leon A., & Zachary, James F. 2005. Superthreshold behavior of ultrasound-induced lung hemorrhage in adult rats: Role of pulse repetition frequency and exposure duration revisited. *Journal of ultrasound in medicine*, **24**(3), 339–348.
- O'Brien, William D. W.D., & Zachary, J.F. 1997. Lung damage assessment from exposure to pulsed-wave ultrasound in the rabbit, mouse, and pig. *Ieee transactions on ultrasonics, ferroelectrics and frequency control*, **44**(2), 473–485.
- O'Brien, William D., Jr, Simpson, Douglas G., Frizzell, Leon A., & Zachary, James F. 2006. Superthreshold Behavior of Ultrasound-Induced Lung Hemorrhage in Adult Rats: Role of Pulse Repetition Frequency and Pulse Duration. *J. ultrasound med.*, **25**(7), 873–882.
- Ochs, Matthias, Nyengaard, Jens R., Jung, Anja, Knudsen, Lars, Voigt, Marion, Wahlers, Thorsten, Richter, Joachim, & Gundersen, Hans Jørgen G. 2004. The Number of Alveoli in the Human Lung. *American journal of respiratory and critical care medicine*, **169**(1), 120–124.
- Pace, N. G., & Jensen, Finn. 2002. *Impact of Littoral Environmental Variability on Acoustic Predictions and Sonar Performance*. Springer Science & Business Media.
- Patterson, Brandon, Miller, Douglas, & Johnsen, Eric. 2012a. Theoretical microbubble dynamics in a homogeneous viscoelastic medium at capillary breaching thresholds. *The journal of the acoustical society of america*, **131**(4), 3385–3385.
- Patterson, Brandon, Miller, Douglas L, & Johnsen, Eric. 2012b. Theoretical microbubble dynamics in a viscoelastic medium at capillary breaching thresholds. *The journal of the acoustical society of america*, **132**(6), 3770.
- Penney, D.P., Schenk, E.A., Maltby, K., Hartman-Raeman, C., Child, S.Z., & Carstensen, E.L. 1993. Morphological effects of pulsed ultrasound in the lung. *Ultrasound in medicine & biology*, **19**(2), 127–135.
- Perlman, Carrie E., & Wu, You. 2014. In situ determination of alveolar septal strain, stress and effective Young's modulus: an experimental/computational approach. *American journal of physiology. lung cellular and molecular physiology*, **307**(4), L302–10.

- Porter, Tyrone M., Smith, Denise A. B., & Holland, Christy K. 2006. Acoustic Techniques for Assessing the Optison Destruction Threshold. *J. ultrasound med.*, **25**(12), 1519–1529.
- Raeman, Carol H., Child, Sally Z., & Carstensen, Edwin L. 1993. Timing of exposures in ultrasonic hemorrhage of murine lung. *Ultrasound in medicine & biology*, **19**(6), 507–512.
- Raeman, C.H., Child, S.Z., Dalecki, D., Cox, C., & Carstensen, E.L. 1996. Exposure-time dependence of the threshold for ultrasonically induced murine lung hemorrhage. *Ultrasound in medicine & biology*, **22**(1), 139–141.
- Raisinghani, Ajit, Rafter, Patrick, Phillips, Patrick, Vannan, Mani A., & DeMaria, Anthony N. 2004. Microbubble contrast agents for echocardiography: rationale, composition, ultrasound interactions, and safety. *Cardiology clinics*, **22**(2), 171–180.
- Richtmyer, R.D. 1960. Taylor Instability in Shock Acceleration of Compressible Fluids. *Communications on pure and applied mathematics*, **XIII**, 297–319.
- Roan, Esra, & Waters, Christopher M. 2011. What do we know about mechanical strain in lung alveoli? *American journal of physiology - lung cellular and molecular physiology*, **301**(5), L625–L635.
- Rognin, Nicolas G., Frinking, Peter, Costa, Maria, & Ardit, Marcel. 2008. In-vivo perfusion quantification by contrast ultrasound: Validation of the use of linearized video data vs. raw RF data. *Pages 1690–1693 of: 2008 ieee ultrasonics symposium*. IEEE.
- Sadot, O., Erez, L., Alon, U., Oron, D., Levin, L. A., Erez, G., Ben-Dor, G., & Shvarts, D. 1998. Study of Nonlinear Evolution of Single-Mode and Two-Bubble Interaction under Richtmyer-Meshkov Instability. *Physical review letters*, **80**(8), 1654–1657.
- Samtaney, Ravi, & Zabusky, Norman J. 1994. Circulation deposition on shock-accelerated planar and curved density-stratified interfaces: models and scaling laws. *Journal of fluid mechanics*, **269**(-1), 45.
- Sboros, V, MacDonald, C.A., Pye, S.D., Moran, C.M., Gomatam, J, & McDicken, W.N. 2002. The dependence of ultrasound contrast agents backscatter on acoustic pressure: theory versus experiment. *Ultrasonics*, **40**(1-8), 579–583.
- Schürch, S, Goerke, J, & Clements, J A. 1976. Direct determination of surface tension in the lung. *Proceedings of the national academy of sciences of the united states of america*, **73**(12), 4698–702.
- Sha, Liewei, & Nolte, Loren W. 2005. Effects of environmental uncertainties on sonar detection performance prediction. *The journal of the acoustical society of america*, **117**(4), 1942.
- Shyue, Keh-Ming. 2001. A Fluid-Mixture Type Algorithm for Compressible Multicomponent Flow with MieGrüneisen Equation of State. *Journal of computational physics*, **171**(2), 678–707.

- Simon, Julianna C, Sapozhnikov, Oleg A, Khokhlova, Vera A, Wang, Yak-Nam, Crum, Lawrence A, & Bailey, Michael R. 2012. Ultrasonic atomization of tissue and its role in tissue fractionation by high intensity focused ultrasound. *Physics in medicine and biology*, **57**(23), 8061–78.
- Singh, Siddharth, & Goyal, Abha. 2007. The origin of echocardiography: a tribute to Inge Edler. *Texas heart institute journal*, **34**(4), 431–8.
- Skyba, D M, Price, R J, Linka, A Z, Skalak, T C, & Kaul, S. 1998. Direct in vivo visualization of intravascular destruction of microbubbles by ultrasound and its local effects on tissue. *Circulation*, **98**(4), 290–3.
- Stone, Lawrence D., & Osborn, Bryan R. 2004. Effect of environmental prediction uncertainty on target detection and tracking. *Pages 58–69 of: Drummond, Oliver E. (ed), Defense and security*. International Society for Optics and Photonics.
- Tarantal, Alice F, & Canfield, Don R. 1994. Ultrasound-induced lung hemorrhage in the monkey. *Ultrasound in medicine & biology*, **20**(1), 65–72.
- Taylor, G. 1950. The Instability of Liquid Surfaces when Accelerated in a Direction Perpendicular to their Planes. I. *Proceedings of the royal society a: Mathematical, physical and engineering sciences*, **201**(1065), 192–196.
- Tjan, K. K., & Phillips, W. R. C. 2007 (mar). *On impulsively generated inviscid axisymmetric surface jets, waves and drops*.
- Tjan, K.K, & Phillips, W.R.C. 2008. On the impulsive generation of drops at the interface of two inviscid fluids. *Proceedings of the royal society a: Mathematical, physical and engineering sciences*, **464**(2093), 1125–1140.
- Urick, R. J. 1962. Generalized Form of the Sonar Equations. *The journal of the acoustical society of america*, **34**(5), 547.
- West, J B, Tsukimoto, K, Mathieu-Costello, O, & Prediletto, R. 1991. Stress failure in pulmonary capillaries. *Journal of applied physiology (bethesda, md. : 1985)*, **70**(4), 1731–1742.
- West, JOHN B. 2000. Pulmonary capillary stress failure. *Journal of applied physiology*, **89**(6), 2483 LP – 2489.
- Yang, Xinmai, & Church, Charles C. 2005. A model for the dynamics of gas bubbles in soft tissue. *The journal of the acoustical society of america*, **118**(6), 3595–3606.
- Zachary, J. F., & O'Brien, W. D. 1995. Lung Lesions Induced by Continuous- and Pulsed-Wave (Diagnostic) Ultrasound in Mice, Rabbits, and Pigs. *Veterinary pathology*, **32**(1), 43–54.
- Zachary, James F., Frizzell, Leon a., Norrell, Kandice S., Blue, James P., Miller, Rita J., O'Brien, William D, & O'Brien, William D. 2001a. Temporal and spatial evaluation of lesion reparative responses following superthreshold exposure of rat lung to pulsed ultrasound. *Ultrasound in medicine and biology*, **27**(6), 829–839.

- Zachary, James F., Blue, James P., Miller, Rita J., Ricconi, Brian J., Eden, J. Gary, & O'Brien, William D. 2006. Lesions of ultrasound-induced lung hemorrhage are not consistent with thermal injury. *Ultrasound in medicine and biology*, **32**(11), 1763–1770.
- Zachary, J.F., Semprott, J.M., Frizzell, L.A., Simpson, D.G., & O'Brien, W.D. 2001b. Superthreshold behavior and threshold estimation of ultrasound-induced lung hemorrhage in adult mice and rats. *Ieee transactions on ultrasonics, ferroelectrics and frequency control*, **48**(2), 581–592.
- Zeqiri, Bajram. 2003. Exposure criteria for medical diagnostic ultrasound: II. Criteria based on all known mechanisms. *Ultrasound in medicine & biology*, **29**(12), 1809.
- Zhang, Qiang, & Sohn, Sung-Ik. 1997. Nonlinear theory of unstable fluid mixing driven by shock wave. *Physics of fluids*, **9**(4), 1106.
- Zingarelli, R a. 2008. A mode-based technique for estimating uncertainty in range-averaged transmission loss results from underwater acoustic calculations. *The journal of the acoustical society of america*, **124**(4), EL218–L222.